UNIVERSITY OF SOUTHAMPTON

Faculty of Engineering and Physical Sciences
School of Physics and Astronomy

$B \to \pi \ell \nu$ and $B_s \to K \ell \nu$ decays in the Continuum Limit of Lattice QCD

by

Ryan Christopher Hill

A thesis for the degree of
Doctor of Philosophy

April 2022

University of Southampton

Abstract

Faculty of Engineering and Physical Sciences
School of Physics and Astronomy

Doctor of Philosophy

$B \to \pi\ell\nu$ and $B_s \to K\ell\nu$ decays in the Continuum Limit of Lattice QCD

by Ryan Christopher Hill

The Standard Model of particle physics is our current best model of the fundamental mechanics of nature. However, it cannot explain all observed phenomena, and clearly there must be new physics to uncover. At some level of precision, new physics effects must enter standard model predictions, and present themselves as discrepancies between observation and theory. Finding such clues at the precision frontier will provide valuable input on the advancement of our theoretical understanding of nature.

We see intriguing tensions between theoretical expectations and collider experiments for semileptonic heavy-light decays. The expected unitarity of the Cabbibo-Kobayashi-Maskawa (CKM) matrix is in tension with a combination of theoretical calculations and experimental evidence at a 3σ level for the first row of the matrix, and a similar $2-3\sigma$ discrepancy is present between determinations of the $|V_{ub}|$ matrix element from exclusive $B \to \pi\ell\nu$ decays and inclusive $B \to X_u\ell\nu$ decays. Investigating CKM matrix elements such as $|V_{ub}|$ requires the theoretical calculation of QCD form factors, which must be calculated non-perturbatively in the low energy regime of QCD, in combination with observations of decay rates from the B-factories and LHCb.

Here we present our work on determining the standard model QCD form factors for $B \to \pi\ell\nu$ and $B_s \to K\ell\nu$ using the non-perturbative lattice QCD technique. Our calculations of these quantities are more precise than a previous 2015 determination currently used in theoretical averages, and by updating these results we anticipate a corresponding increase in precision in these averages. In addition, we investigate a modification to standard lepton flavour universality ratios, which we demonstrate to provide more precise predictions. We suggest that these ratios may be used as an additional way to monitor lepton flavour universality.

Contents

List of Figures

List of Tables

List of Additional Material

Dataset DOI: 10.5258/SOTON/D2195

Declaration of Authorship

I declare that this thesis and the work presented in it is my own and has been generated by me as the result of my own original research.

I confirm that:

1. This work was done wholly or mainly while in candidature for a research degree at this University;
2. Where any part of this thesis has previously been submitted for a degree or any other qualification at this University or any other institution, this has been clearly stated;
3. Where I have consulted the published work of others, this is always clearly attributed;
4. Where I have quoted from the work of others, the source is always given. With the exception of such quotations, this thesis is entirely my own work;
5. I have acknowledged all main sources of help;
6. Where the thesis is based on work done by myself jointly with others, I have made clear exactly what was done by others and what I have contributed myself;
7. Parts of this work have been published as: [1], [2], and [3].

Signed:..... Date:.....

Acknowledgements

I would first like to thank my supervisors, Profs. Andreas Jüttner and Jonathan Flynn. Their patience, knowledge, and endless support have been essential to both my work and my personal growth as a researcher, and I would not be writing this thesis without them. Secondly, I would like to thank my direct collaborators, Tobi Tsang, Oliver Witzel, and Amarjit Soni, who have all broadened my knowledge immeasurably and given me support throughout my PhD. I must also extend gratitude to James Richings and Nils Asmussen, who were frequently subjected to my enthusiasm for programming and who built the sulat lattice analysis library alongside me.

I would also like to thank the members of the Southampton lattice group, and my friends in the school of physics and astronomy, for making my PhD experience memorable. I would also like to thank Michael Delve, who is a seemingly endless source of interesting mathematics, and who frequently renews my own enthusiasm for the subject.

I cannot conclude my acknowledgements without thanking my parents, who always go above and beyond any reasonable levels of support for me. Thank you both for indulging my weird academic interests throughout my life — and for all the cat photos. Finally, I would like to thank Nanami for always supporting me and putting up with my career aspirations. You make everything worth it.

Chapter 1

Introduction

The Standard Model (SM) of particle physics is a spectacularly successful theory of the fundamental mechanics of nature, with no confirmed discrepancies between experimental tests and theoretical calculation, in addition to a wealth of successfully predicted phenomena. The SM is still however an incomplete theory, notably unable to explain observed phenomena such as:

- The precise nature of neutrino masses and neutrino oscillations,
- The observed scale of the matter-antimatter asymmetry,
- The influence of dark matter and dark energy,
- Gravity.

There are numerous proposed extensions to the SM, with no successor yet clearly crowned by experiment. Precision tests of SM quantities provide bounds on the form that such extensions can take, by constraining the size of deviations from standard model predictions, and by identifying signals of new physics that must be explained by novel theoretical developments.

One such avenue of investigation is the unitarity of the Cabibbo-Kobayashi-Maskawa (CKM) matrix. The magnitudes of the individual CKM matrix elements parameterise the probability of one quark flavour decaying into another, and as a consequence of unitarity all rows and columns of the matrix should sum in quadrature to 1. Violations of CKM unitarity are strong indicators of unaccounted-for particles or decay paths linked to new physics. As of 2020, a meta-analysis of existing data by the Particle Data Group [4] finds a 3σ tension with unitarity in the first row of the CKM matrix, which hints at new physics and warrants further investigation.

The CKM matrix element $|V_{ub}|$ is relevant for decays involving a $b \to u$ transition. It enters the first row of the CKM matrix and, as of 2020, is the least precisely determined

matrix element [4]. It is also the element with the smallest magnitude in the first row of the CKM matrix, which led to it historically being considered negligible in some circumstances. This is, however, not the case — there exist prominent B-anomalies between experiment and theory; such as a long-standing 2–3 σ discrepancy between determinations of $|V_{ub}|$ from exclusive $B \to \pi \ell \nu$ and inclusive $B \to X_u \ell \nu$ decays, where X_u is any charmless final state [4]. These facts make further refinements of $|V_{ub}|$ and the resolution of such tensions an important direction of research.

Efforts to compute $|V_{ub}|$ from exclusive semileptonic decay modes require a union of theoretical and experimental effort. The SM decay rate equations for tree-level semileptonic $B_{(s)}$ decays currently feature two major sources of uncertainty - the decay rates themselves, and quantities termed "QCD form factors" that summarise QCD effects on the decay. The decay rates are experimentally measured at B-factories and LHCb, whereas the QCD form factors must be determined *via* non-trivial theoretical calculations.

The form factors must be calculated in the low-energy regime of QCD, where bound quarks reside and the coupling constant becomes $\mathcal{O}(1)$, rendering a perturbative expansion too difficult or simply impossible. In order to probe the momentum-dependence of the form factors in this range, non-perturbative approaches must be considered. A phenomenological method applicable for the more energetic region of the low-energy regime is known as QCD sum rules [5], for which global averages are provided by the Heavy Flavor Averaging Group [6]. For the very low energy regime, there also exists a well-established first-principles, systematically improvable method — a description of QCD termed "lattice QCD", which is the method employed in this work.

The central premise of Lattice QCD is to replace continuous space-time with a finite, discrete lattice of space-time points equipped with a Euclidean metric. Regularising QCD in this manner renders the path integral approach computationally tractable, and hence accessible to simulation techniques [7]. By carefully considering the renormalisation of the theory and phenomenology of the simulated processes, lattice results can be extrapolated to the continuum and used to make SM predictions.

Lattice QCD for b physics comes with additional challenges. Discretisation errors on fermions in Lattice QCD enter as several terms proceeding as powers of $(m_q a)$, with m_q the bare mass of a quark q and a the distance between lattice sites—the *lattice spacing*—which are problematic for heavy quarks, where this product can easily become $\mathcal{O}(\gtrsim 1)$. Typical lattice spacings today fall in the 2–4 GeV^{-1} range due to computational constraints, and the b quark mass in the $\overline{\text{MS}}$ scheme is determined to be $4.18^{+0.03}_{-0.02}$ GeV [4]; if a standard approach is employed, these parameters will lead to uncontrolled errors on the b quark. In order to simulate b physics on the lattice, alternative methods must be employed. Lattice QCD simulations of b-physics are

therefore carried out with some carefully formulated technique, such as extrapolating from simulations made with charm-like masses (as is done by the HPQCD collaboration using Highly Improved Staggered Quarks (HISQ) [8]), or by using a discretised effective action, such as Relativistic Heavy Quarks (RHQ) [9–11].

In this work, we present our calculations of the QCD form factors f_+ and f_0 for the processes $B \to \pi\ell\nu$ and $B_s \to K\ell\nu$ over the full allowed kinematic range. We simulate b quarks with the Columbia formulation of the RHQ action [11], and all other quarks with Shamir Domain-Wall fermions [12–16].

The sections of this thesis are organised as follows:

Chapter 2. First we give a brief introduction to Standard Model physics, highlighting the origins of the CKM matrix and particular effective theories relevant for Lattice QCD.

Chapter 3. Next we discuss how to discretise the continuum theory in order to make it suitable for computer simulation *via* the Lattice QCD formalism, and why this is both necessary and justified.

Chapter 4. In this section we discuss elements of Lattice QCD and continuum phenomenology pertinent to $B \to \pi\ell\nu$ and $B_s \to K\ell\nu$ decays.

Chapter 5. Next we return to the project to discuss the details of the simulation.

Chapter 6. The following section describes the analysis strategy, drawing on the background built up in sections 2–4, and presents the results of the project.

Chapter 7. We finish by drawing conclusions about the project results and discussing the future outlook.

My individual contributions to this project are as follows:

1. I performed the fits to extract Z_V^{bb} in section 6.1;
2. I performed all B meson mass fits, and demonstrated the requirement for point-point data to reliably fit the excited states in section 6.2;
3. I cross-checked the B_s, K, and π mass fits in section 6.2;
4. I performed all $B \to \pi$ form factor fits and cross-checked the $B_s \to K$ fits in section 6.3;
5. I performed the box analysis to obtain the systematic error due to the uncertainty in the RHQ parameters in section 6.5.5;

6. I constructed the total fit systematic and synthetic data points for $B \to \pi$, and cross-checked these for $B_s \to K$, in section 6.5;

7. I performed all z-fits for $B \to \pi$, and cross-checked $B_s \to K$, in section 6.6;

8. I calculated the lepton universality ratios for $B \to \pi$, and cross-checked $B_s \to K$, in section 6.7.

Chapter 2

The Standard Model

2.1 Introduction

The Standard Model is an $\mathrm{SU}(3) \times \mathrm{SU}(2) \times \mathrm{U}(1)$ gauge theory that describes the quantum field theories of the strong, weak, and electromagnetic forces. As noted in the introduction, the SM is remarkably successful. As an example, the value of the anomalous magnetic moment of the electron is famously one of the most precise measurements [4], predictions [17], and agreements—to around 10 significant figures, with a discrepancy of little more than 1σ—in modern physics. Today, the only known deviation from SM behaviour is the existence of neutrino masses. In the standard formulation of the SM, neutrinos are chosen to be explicitly massless, and will require the introduction of new physics to account for. The version of the SM presented here will ignore the existence of neutrino masses for brevity.

Many elements of the Standard Model were predicted by theoretical developments and later confirmed by experiment — what we would recognise today as a charm quark was proposed by several individuals, including Bjorken and Glashow [18], and was later a requirement of the Glashow–Iliopoulos–Maiani (GIM) mechanism as published in 1970 before its eventual detection in 1974 *via* the J/ψ particle [19, 20]; and a third generation of quarks was then predicted in 1973 by the development of the Cabibbo-Kobayashi-Maskawa matrix [21, 22], which was originally proposed to introduce CP-violation to the Standard Model and is now a cornerstone of electroweak theory. The existence of the bottom and top quarks themselves were experimentally confirmed in 1977 [23] and 1995 [24, 25], both at Fermilab. Electroweak theory—generally attributed to Glashow, Salam, and Weinberg—is built on several decades of theoretical development for the weak interaction and includes predictions for the $W^{\pm}$ and Z bosons [26] that were experimentally confirmed in 1983 at CERN [27, 28]. The most recent detections came in 2001, of the tau neutrino [29] and in 2012 of the Higgs boson [30, 31].

However, the Standard Model fails to provide an explanation for many other phenomena; such as gravity, and the observed matter-antimatter asymmetry in the universe due to an insufficient degree of CP-violation in the model. There are also a number of tensions within the Standard Model which may or may not become accepted violations of the SM as experimental measurements and theoretical calculations improve, such as the $\sim 3\sigma$ tension in CKM matrix unitarity [4]. A long-standing tension between theory and experiment for the anomalous magnetic moment of the muon $g-2$ has also historically been an exciting hint of new physics, and as of April 2021 results from the Fermilab $g-2$ experiment [32] place the tension at 4.2σ. However, a recent Lattice QCD calculation of $g-2$ from the Budapest-Marseille-Wuppertal (BMW) collaboration [33] instead puts the tension at 2.4σ, substantially decreasing the tension between theory and experiment. The exact status of this tension is currently unclear, but more experiments and calculations are planned by various groups for the future.

Of particular relevance to this project are the "B-anomalies" present in lepton flavour universality tests. Heavy-light (semi)leptonic decays are sensitive to the effects of unknown heavy particles, which may modify the coupling of the weak bosons to leptons. The effect of such particles would be indirectly observable as violating lepton flavour universality — the statement that leptons couple to the weak bosons uniformly under the SM. Presently, sizeable tensions exists for $B \to D^{(*)}\ell\nu$ and $B \to K^{(*)}\ell\nu$ processes; the Heavy Flavour Averaging Group [6] provides an average of experimental results [34–41] that is in tension with SM predictions [42–44] at a $\sim 3\sigma$ level for $B \to D^*\ell\nu$, and a 2.5σ discrepancy in the $B^+ \to K^+\ell^+\ell^-$ channel was reported by LHCb in 2019 [45]. A recent 2021 result from LHCb also finds a 3.6σ discrepancy in $B_s^0 \to \phi\mu^+\mu^-$ decays [46].

In this chapter, we begin with a general discussion of the language and features of quantum field theories in section 2.2. The underlying physics of the Standard Model is broken into sections on electroweak theory in section 2.3, in which we also discuss the origin of mass and the CKM matrix; and on QCD in section 2.4, in which we also discuss its approximate chiral symmetry—which is foundational to chiral perturbation theory, presented in section 2.5. We finish the chapter by giving a brief overview in section 2.6 of low-energy Standard Model physics with the heavy weak bosons integrated out, which is highly relevant for latttice QCD calculations of hadronic matrix elements for weak decays and flavour physics; and by introducing the theoretical background for the semileptonic decays of interest to this project in section 2.7. This section is largely based on the book by Peskin and Schroeder [47], which can be consulted for a more thorough introduction to the topics presented here.

2.2 Quantum Field Theories and Path Integral Quantisation

A modern understanding of quantum physics is primarily concerned with the description of mathematical fields. The fields utilised in quantum field theories (QFTs) are quantities that take some value over all space-time four-positions x. These fields are not particles; they are highly abstract quantities that give rise to particles as excitations of the fields. QFTs find their origin in the combination of quantum mechanics with special relativity, which naturally gives rise to a many-body theory of fields which accommodates particle creation and annihilation. The first phyiscal interaction to be quantised in this manner was electromagnetism, giving rise to quantum electrodynamics (QED). The subsequent development of theories describing the weak and strong interactions has been outlined in the introductory section to this chapter.

Traditionally, one begins by building a classical field theory, the fields of which are then quantised to generate a quantum field theory. There are two main approaches to quantising a field theory: "canonical quantisation", following Dirac [48], where the fields are interpreted as operators on a Fock space that satisfy specified equal-time commutation relations; and "path-integral quantisation" following Feynman [49], which integrates over all possible paths a particle can take, with each path weighted by the action (up to a factor of i). The path-integral formulation is foundational to lattice QCD, as will be discussed in chapter 3, and it will therefore be the formalism we utilise throughout this work.

The path integral is defined for some observable $\mathcal{O}$ as

$$\langle \widehat{\mathcal{O}} \rangle = \frac{1}{Z} \int \mathcal{D}[\psi_1(x)...\psi_n(x)] \mathcal{O} e^{iS[\psi_1(x)...\psi_n(x)]}, \tag{2.1}$$

where $\widehat{\mathcal{O}}$ is the operator for $\mathcal{O}$ operating on the Fock space of states, $\psi_1...\psi_n$ are the fields of the theory, Z is the partition function

$$Z = \int \mathcal{D}[\psi_1(x)...\psi_n(x)] e^{iS[\psi_1(x)...\psi_n(x)]}, \tag{2.2}$$

and $\mathcal{D}$ is the integral measure, defining each path to be summed over in the integral:

$$\mathcal{D}[\psi(x)] = \lim_{n\to\infty} \sum_i^n d\psi(x_i). \tag{2.3}$$

The action S is described in terms of a Lagrangian density (abbreviated to just "the Lagrangian"); which contains the dynamics of the theory:

$$S[\psi_1(x)...\psi_n(x)] = \int d^4x \mathcal{L}[\psi_1(x)...\psi_n(x)]. \tag{2.4}$$

We can thus define a field theory by specifying its Lagrangian.

The quantities $\langle\widehat{\mathcal{O}}\rangle$ coming out of the path integral are matrix elements of the operators $\widehat{\mathcal{O}}$ for the observable $\mathcal{O}$. These matrix elements are interchangeably called *Green's functions*, *n-point functions*, *correlation functions*, and *correlators*, and are defined as the vacuum expectation value of time-ordered products of operators

$$\langle\widehat{\mathcal{O}}\rangle = \left\langle 0 \,\middle|\, \mathrm{T}\left[\widehat{\psi}_1(x)...\widehat{\psi}_n(x)\right] \middle|\, 0\right\rangle, \tag{2.5}$$

where the 'n' in the name 'n-point function' refers to the number of operators in the product, and ψ is a generic label for a field, irrespective of whether it is scalar, vector, or fermionic. A particularly common function is the two-point function, also called the *propagator*, which describes the probability of propagation between two spacetime points:

$$\left\langle 0 \,\middle|\, \mathrm{T}\left[\widehat{\psi}(x)\widehat{\psi}(y)\right] \middle|\, 0\right\rangle. \tag{2.6}$$

Since it is relevant to the discussion of the necessity for non-perturbative methods in QCD, it is worth taking a moment to discuss perturbation theory in terms of the path integral. Here, perturbation theory manifests as splitting the action into a solvable "free" part and a non-solvable "interacting" part, parameterised by some expansion parameter g:

$$S = S_0 + gS_I. \tag{2.7}$$

Without going into the details, the "free" part can then be calculated whilst the "interacting" part can be expanded in terms of the parameter g. One finds that the expansion parameter corresponds to the coupling strength of interacting field theories, and since these coupling parameters are dependent on the energy scale of the interaction—as we will note in section 2.4.1—perturbation theory is inevitably only applicable over a certain range of energies. Unfortunately for QCD, this does not cover the full kinematic range accessible to the decays of bound states, and in this case we must look to non-perturbative approaches for answers instead.

2.3 Electroweak Theory

The electroweak interaction is described in the Standard Model by an $\mathrm{SU}(2)_\mathrm{W} \times \mathrm{U}(1)_\mathrm{Y}$ gauge theory, formalised in [26] as a renormalisable theory after several decades of theoretical development. The subgroups of electroweak theory are the "weak isospin" and "weak hypercharge" groups respectively, which are spontaneously broken to a $\mathrm{U}(1)_\mathrm{EM}$ electromagnetic symmetry *via* the Higgs mechanism at low energies to leave a massless photon and massive $W^\pm$ and Z vector bosons (which have "eaten" the three Goldstone bosons corresponding to the broken symmetry generators).

Since the theory carries an $\mathrm{SU}(2)_\mathrm{W} \times \mathrm{U}(1)_\mathrm{Y}$ gauge symmetry, the fields of the SM must take the following transformation laws for the $\mathrm{SU}(2)_\mathrm{W}$ and $\mathrm{U}(1)_\mathrm{Y}$ symmetries:

$$\psi(x) \to e^{\frac{i}{2} I_{3,\psi} T^a \theta^a(x)} \psi(x), \quad \psi(x) \to \begin{pmatrix} e^{\frac{i}{2} Y_\psi \beta(x)} & 0 \\ 0 & e^{\frac{i}{2} Y_\psi \beta(x)} \end{pmatrix} \psi(x), \tag{2.8}$$

where Y_ψ is the weak hypercharge of the field ψ, I_ψ is the weak isospin of ψ, and T^a are the three generators of $\mathrm{SU}(2)_\mathrm{W}$, which bear the relation

$$T^a = \frac{\sigma^a}{2} \tag{2.9}$$

where σ^a are the Pauli matrices. Naturally, for fields that do not interact with the electroweak force, these transformation rules are an identity transformation since $I_3 = 0, Y = 0$.

The minimally coupled electroweak covariant derivative therefore takes the form

$$D_\mu \psi(x) = \partial_\mu \psi(x) - i g_W I_{3,\psi} T^a W^a_\mu \psi(x) - \frac{i}{2} g_Y Y B_\mu \psi(x), \tag{2.10}$$

where ψ is some SM field, g_W is the $\mathrm{SU}(2)_\mathrm{W}$ weak isospin coupling, g_Y is the weak hypercharge coupling, I is the weak isospin of ψ , and Y is the weak hypercharge of ψ, W^a are the gauge fields of the three $\mathrm{SU}(2)_\mathrm{W}$ bosons, and B is the gauge field of the $\mathrm{U}(1)_\mathrm{Y}$ boson. The lack of direct interactions between the W^a and B fields is guaranteed by the fact that the generators of their gauge groups commute, *i.e.*

$$[T^a, Y] = 0. \tag{2.11}$$

The weak isospin of a field is given by the $\mathrm{SU}(2)_\mathrm{W}$ representation the field is part of, and the weak hypercharges of the fields are determined by choosing values such that gauge anomalies in the theory vanish. For brevity, we will skip the calculation of the hypercharges and refer to [47], which we shall directly quote the values from; although here we use a convention where the weak hypercharges are twice the value of those quoted in [47]. Table 2.1 summarises the values of weak isospin and weak hypercharge which we will use in the proceeding sections.

The electroweak Lagrangian can be arranged as

$$\mathcal{L}_\mathrm{EW} = \mathcal{L}_\mathrm{Gauge} + \mathcal{L}_\mathrm{Fermions} + \mathcal{L}_\mathrm{Higgs} + \mathcal{L}_\mathrm{Yukawa}, \tag{2.12}$$

with each of the four terms representing some thematic component of the theory. We shall now visit each of these terms in series, before discussing the Higgs mechanism and the effects it has on the fields of the Lagrangian.

Field	I_3	Y	Q
v_e, v_μ, v_τ	+1/2	-1	0
e_L, μ_L, τ_L	-1/2	-1	-1
e_R, μ_R, τ_R	0	-2	-1
u_L, c_L, t_L	+1/2	+1/3	+2/3
d_L, s_L, b_L	-1/2	+1/3	-1/3
u_R, c_R, t_R	0	+4/3	+2/3
d_R, s_R, b_R	0	+2/3	-1/3
$W^\pm$	± 1	0	± 1
Z	0	0	0
γ	0	0	0
h	-1/2	1	0

TABLE 2.1: The weak isospin eigenvalue (I_3), weak hypercharge (Y), and electromagnetic quantum number (Q) for the fields that enter the spontaneously-broken electroweak Lagrangian. The electromagnetic quantum number is related to weak isospin and weak hypercharge by $Q = I_3 + Y/2$.

2.3.1 Gauge Term

The Gauge component describes the propagators and interactions of four gauge bosons of the theory,

$$\mathcal{L}_{\text{Gauge}} = -\frac{1}{4} W^a_{\mu\nu} W^{a\mu\nu} - \frac{1}{4} B_{\mu\nu} B^{\mu\nu} \tag{2.13}$$

where $W^a_{\mu\nu}$ is the field strength tensor that corresponds to the $\text{SU}(2)_\text{W}$ symmetry, with a running over the three $\text{SU}(2)_\text{W}$ gauge bosons; and $B_{\mu\nu}$ is the field strength tensor corresponding to the $\text{U}(1)_\text{Y}$ symmetry.
$B_{\mu\nu}$ is defined by

$$B_{\mu\nu} = \partial_\mu B_\nu - \partial_\nu B_\mu \tag{2.14}$$

where B_μ is the gauge field of the B boson. This contains only propagator terms, and thus there are no self-interactions of the B boson, as expected from an Abelian gauge group.

The field strength tensor of the non-Abelian $\text{SU}(2)_\text{W}$ group, however, does include interactions terms between the three W fields:

$$W^a_{\mu\nu} = \partial_\mu W^a_\nu - \partial_\nu W_{a\mu} + i g_W \epsilon^{abc} \left[W^b, W^c \right]. \tag{2.15}$$

The W^1, W^2, and W^3 bosons live in the adjoint representation of $\text{SU}(2)_\text{W}$, and as such form an $\text{SU}(2)_\text{W}$-triplet and carry the weak isospins +1, 0, and -1 respectively. The four electroweak bosons all carry a 0 weak hypercharge.

2.3.2 Fermionic Term

The fermion fields and their couplings to the gauge bosons are described by the fermionic part of the electroweak Lagrangian. The Lagrangian reads:

$$\mathcal{L}_{\text{Fermions}} = \underbrace{i\bar{Q}^j \not{D} Q^j + i\bar{u}^j \not{D} u^j + i\bar{d}^j \not{D} d^j}_{\text{Quarks}} + \underbrace{i\bar{L}^j \not{D} L^j + i\bar{e}^j \not{D} e^j}_{\text{Leptons}} \tag{2.16}$$

The quark component of the Lagrangian is split into three components. The Q^j fields are left-handed $\text{SU}(2)_\text{W}$-doublets:

$$Q^i = \left(\begin{pmatrix} u_L \\ d_L \end{pmatrix}, \begin{pmatrix} c_L \\ s_L \end{pmatrix}, \begin{pmatrix} t_L \\ b_L \end{pmatrix} \right), \tag{2.17}$$

and the u^i and d^i are right-handed $\text{SU}(2)_\text{W}$-singlets:

$$u^i = (u, c, t); \;\; d^i = (d, s, b). \tag{2.18}$$

The L^i fields are left-handed $\text{SU}(2)_\text{W}$-doublets of electrons and neutrinos:

$$L^i = \left(\begin{pmatrix} \nu_e \\ e_L \end{pmatrix}, \begin{pmatrix} \nu_\mu \\ \mu_L \end{pmatrix}, \begin{pmatrix} \nu_\tau \\ \tau_L \end{pmatrix} \right), \tag{2.19}$$

and the e^i are right-handed $\text{SU}(2)_\text{W}$-singlets:

$$e^i = (e_R, \mu_R, \tau_R). \tag{2.20}$$

Notably, there are no right-handed neutrinos in the SM, although right-handed neutrinos are hypothesised as "Sterile Neutrinos" that do not interact *via* the fundamental interactions of the SM, as a possible source of neutrino masses.
Given that the right-handed components of the fermions are $\text{SU}(2)_\text{W}$-singlets and thus take $I = 0$; the covariant derivative for right-handed fields has a zero $\text{SU}(2)_\text{W}$ term, whereas the left-handed fields live in the fundamental representation of $\text{SU}(2)_\text{W}$ and carry the weak isospins +1/2 and -1/2:

$$D_\mu L = \partial_\mu L - \frac{i}{2} g_W T^a W_\mu^a L - \frac{i}{2} g_Y Y_L B_\mu L, \tag{2.21}$$

$$D_\mu R = \partial_\mu R - \frac{i}{2} g_Y Y_R B_\mu R, \tag{2.22}$$

where $D_\mu L$ is the action of the covariant derivative on left-handed $\text{SU}(2)_\text{W}$-doublets and $D_\mu R$ is that for right-handed $\text{SU}(2)_\text{W}$-singlets.

2.3.3 Higgs and Yukawa Terms

The Higgs part of the Lagrangian describes the Higgs propagator and the coupling of the Higgs and electroweak boson fields. It is given by

$$\mathcal{L}_{\text{Higgs}} = |D_\mu \phi|^2 - \mu^2 |\phi|^2 - \frac{\lambda}{2}(|\phi|^2)^2 \tag{2.23}$$

where μ^2 is the mass of the Higgs field, λ is the coefficient of the quartic potential term, and ϕ is a scalar $\mathrm{SU}(2)_\mathrm{W}$-doublet termed the Higgs field, and given by

$$\phi = \begin{pmatrix} \phi^+ \\ \phi^0 \end{pmatrix} = \frac{1}{\sqrt{2}} \begin{pmatrix} \phi_1 + i\phi_2 \\ \phi_3 + i\phi_4 \end{pmatrix}. \tag{2.24}$$

The Higgs field lives in the fundamental representation of $\mathrm{SU}(2)_\mathrm{W}$ and hence ϕ^+ and ϕ^0 have weak isospins of +1/2 and -1/2 respectively. The covariant derivative is again given by (2.10).

The Yukawa term couples the Higgs field to the fermions, and is given by

$$\mathcal{L}_{\text{Yukawa}} = Y_L^{ij} \bar{L}^i \phi e^j + Y_d^{ij} \bar{Q}^i \phi d^j + Y_u^{ij} \bar{Q}^i \phi^\dagger u^j + h.c., \tag{2.25}$$

where the Y_{ij} are Yukawa couplings for the generations i and j, which are complex matrices that are not necessarily symmetric or Hermitian [47].

Thus far, we have described a theory of long-ranged weak-isospin and weak-hypercharge interactions between massless fermions, mediated by four massless gauge bosons. This, however, is not what we observe in nature — we see a weak force that is a short-ranged interaction mediated by massive bosons, and an electromagnetic force that is long-ranged and mediated by a massless boson, all of which interact with massive fermion fields. The connection between these pictures is elucidated by considering the $\mu^2\phi^2$ mass term in the Higgs sector, which *via* a change-of-variables in the Higgs field termed *spontaneous symmetry breaking* introduces gauge-invariant mass terms to the theory, driven by the Higgs and Yukawa sectors [50–52]. We will outline this process, and its consequences, in section 2.3.4.

2.3.4 Electroweak Symmetry Breaking

Consider the Higgs potential [50–52],

$$V_{\text{Higgs}} = \mu^2 |\phi|^2 + \frac{\lambda}{2} |\phi|^4 \tag{2.26}$$

Taking the derivative with respect to $|\phi|^2$, we see that the potential has a minimum at

$$|\phi| = \left(\frac{-\mu^2}{\lambda}\right)^{1/2}, \tag{2.27}$$

and taking the second derivative gives us the requirement for this to be a minimum of the potential:

$$\lambda > 0. \tag{2.28}$$

The coefficient of the quartic term λ must necessarily be positive, else the potential has no minimum and is thus unphysical. We will label the value given by (2.27) with v and identify this as the *vacuum expectation value* of ϕ.

Armed with this information, let us now examine the μ^2 parameter of (2.27). For a positive μ^2, we get a parabolic potential since the quadratic and quartic computents of the potential sum to some value ≥ 0. In this regime, the Higgs field has a zero vacuum expectation value and the fields of the Standard Model remain massless. However, if we allow μ^2 to become negative, the now negative quadratic term begins to compete with the quartic term and we find that the potential falls to some minimum negative energy given by (2.27), before becoming dominated by the quartic term. The vacuum state of the Higgs field therefore acquires a non-zero expectation value, and becomes degenerate under the $\mathrm{SU}(2)_\mathrm{W}$ gauge symmetry. The Higgs field must, however, choose one of these states to exist in — and since they are all equivalent, the field can fall into any under some particular infinitesimal perturbation. Although the Lagrangian retains full $\mathrm{SU}(2)_\mathrm{W} \times \mathrm{U}(1)_\mathrm{Y}$ symmetry when this occurs, making this choice spontaneously breaks the $\mathrm{SU}(2)_\mathrm{W}$ gauge symmetry of the vacuum state.

This non-zero expectation value requires us to re-parameterise the Higgs field in such a way that we can expand the field around a null expectation value. In order to make this simple, we can pull out an $\mathrm{SU}(2)_\mathrm{W}$ rotation from the Higgs doublet defined in (2.24)

$$\phi(x) = e^{i\frac{\sigma^a}{2}\theta^a(x)} \frac{1}{\sqrt{2}} \begin{pmatrix} 0 \\ v + h(x) \end{pmatrix} \tag{2.29}$$

with $\langle h \rangle = 0$. Note that the Higgs field in (2.29) has been redefined as the product of some $\mathrm{SU}(2)_\mathrm{W}$ doublet and a gauge transform. We are perfectly free to fix this gauge, and we will make the choice $\theta^a = 0$, also known as the *unitary gauge*.

Note also that we have now aligned the vacuum expectation value of the Higgs field without loss of generality with the vector

$$\langle \phi \rangle = \frac{1}{\sqrt{2}} \begin{pmatrix} 0 \\ v \end{pmatrix} \tag{2.30}$$

thanks to $\mathrm{SU}(2)_\mathrm{W}$-invariance in the Lagrangian.

To see what effects the acquisition of a non-zero vacuum expectation value has on electroweak theory, we can insert the unitary gauge-fixed (2.29) into (2.23).

2.3.5 Gauge Boson Masses

We can first study what happens to the electroweak bosons by looking at the terms quadratic in these fields alone:

$$\text{Quad.} = \left| \left(\partial_\mu - \frac{i}{2} g_W T^a W_\mu^a - \frac{i}{2} Y_\phi B_\mu \right) \frac{1}{\sqrt{2}} \begin{pmatrix} 0 \\ v \end{pmatrix} \right|^2 \tag{2.31}$$

$$= -\frac{v^2}{8} \left| \begin{pmatrix} g_W W^3 + g_Y B & g_W (W^1 - iW^2) \\ g_W (W^1 + iW^2) & g_Y B - g_W W^3 \end{pmatrix}_\mu \begin{pmatrix} 0 \\ 1 \end{pmatrix} \right|^2 \tag{2.32}$$

$$= -\frac{v^2}{8} \left(g_W^2 \left((W_\mu^1)^2 + (W_\mu^2)^2 \right) + \left(g_W W_\mu^3 - g_Y B_\mu \right)^2 \right) \tag{2.33}$$

Noting the difference of two squares in the first term in (2.33), we can simplify this expression by making the substitutions

$$W_\mu^\pm = W_\mu^1 \mp i W_\mu^2 \tag{2.34}$$

$$Z_\mu = \frac{1}{\sqrt{g_W^2 + g_Y^2}} \left(g_W W_\mu^3 - g_Y B_\mu \right) \tag{2.35}$$

Which gives us the result

$$-\frac{v^2}{8} \left(g_W^2 W^{\mu +} W_\mu^- + (g_W^2 + g_Y^2) Z^\mu Z_\mu)^2 \right), \tag{2.36}$$

which looks like mass terms for these newly-defined W^+, W^-, and Z fields:

$$-\frac{m_W^2}{2} W^{\mu +} W_\mu^- - \frac{m_Z^2}{2} Z^\mu Z_\mu, \tag{2.37}$$

so we can identify the masses

$$m_W = \frac{v g_W}{2}, \quad m_Z = \frac{v \sqrt{g_W^2 + g_Y^2}}{2}. \tag{2.38}$$

We can see that the vacuum expectation value of the Higgs field leads to three massive degrees of freedom in the theory: W^+, W^-, and Z bosons, which makes the weak interaction they mediate short-ranged. We are still missing the fourth degree of freedom in this new basis; we can identify this by normalising the remaining field in

(2.32), which did not gain a mass term in (2.33):

$$A_\mu = \frac{1}{\sqrt{g_W^2 + g_Y^2}}(g_W W^3 + g_Y B) \tag{2.39}$$

We can use this new basis for the fields to re-write the covariant derivative in terms of our new fields,

$$D_\mu = \partial_\mu - i\frac{g}{\sqrt{2}}(T^+ W_\mu^+ + T^- W_\mu^-) - i\frac{1}{\sqrt{g_W^2 + g_Y^2}} Z_\mu (g_W^2 I_3 - g_Y^2 Y) - i\frac{g_W g_Y}{\sqrt{g_W^2 + g_Y^2}} A_\mu \left(I_3 + \frac{Y}{2}\right), \tag{2.40}$$

where $T^\pm = \frac{1}{2}(\sigma^1 \pm \sigma^2) = \sigma^\pm$, and I_3 is the eigenvalue of the third component of the weak isospin. The massless A_μ field is a product of the surviving U(1) symmetry of the vacuum state, which observes the new gauge symmetry of the vacuum $\mathrm{U}(1)_{\mathrm{EM}}$. As implied by the subscript, we identify this as the photon field, and can therefore read from the covariant derivative that

$$e = \frac{g_W g_Y}{\sqrt{g_W^2 + g_Y^2}}, \quad Q = I_3 + \frac{Y}{2}, \tag{2.41}$$

where e is the electric charge and Q is the electric charge quantum number; here we now see the origin of the relation between weak isospin and electic charge alluded to in table 2.1.

By introducing the Higgs mechanism, we have a functional theory of the weak and electromagnetic forces that reconciles the necessary symmetries with observed masses of the weak bosons. Next, we shall see that the Higgs mechanism also generates the masses of the fermion fields.

2.3.6 Fermion Masses and the CKM Matrix

After electroweak symmetry breaking, the Yukawa Lagrangian becomes [47]

$$\mathcal{L}_{\text{Yukawa}} = -vY_L^{ij}\bar{e}^i \left(1 + \frac{h(x)}{v}\right) e^j - vY_d^{ij}\bar{d}^i \left(1 + \frac{h(x)}{v}\right) d^j - vY_u^{ij}\bar{u}^i \left(1 + \frac{h(x)}{v}\right) u^j + h.c. \tag{2.42}$$

where we have used our definition of the Higgs field in the broken symmetry regime,

$$\phi = \begin{pmatrix} 0 \\ v + h(x) \end{pmatrix}; \quad \phi^\dagger = \begin{pmatrix} v + h(x) \\ 0 \end{pmatrix} \tag{2.43}$$

and taken the appropriate dot product between the left-handed $\mathrm{SU}(2)_{\mathrm{W}}$-doublets and the Higgs field. We have obtained some interaction terms with the Higgs, and also some terms that look suspiciously like mass terms, if not for the Yukawa coupling

matrices—as we noted previously, there is absolutely no requirement for the Yukawa couplings to be diagonal, although they are for the electron fields [47]. We therefore have some distinction to draw in this framework for the quark fields; the quark mass eigenstates that we are used to do not participate in the weak interaction in some simple way, and the physics is more mathematically amenable when these fields are packaged into a weak basis—alternatively called *weak eigenstates*—as in (2.42). We can diagonalise the Yukawa coupling matrices to find the mass eigenstates; the diagonalisation allows us to multiply out the matrix with the fermion fields into a sum of terms without mixing between the fermion flavours, each acting as a mass term.

There should be a unitary transform between the mass and weak eigenstates in order to maintain the normalisation of the theory, and it is a property of Hermitian matrices that they are diagonalisable with unitary matrices. We should therefore seek to diagonalise the products $Y_q Y_q^\dagger$ and $Y_q^\dagger Y_q$, which are necessarily Hermitian by construction:

$$Y_q Y_q^\dagger = U_q M_q^2 U_q^\dagger; \;\; Y_q^\dagger Y_q = W_q M_q^2 W_q^\dagger \tag{2.44}$$

where M is the diagonalised mass matrix, which we can relate to the Yukawa couplings as [47]

$$Y_q = U_q M_q W_q^\dagger, \tag{2.45}$$

where U_q and W_q are necessarily unitary, following the prior discussion. Replacing the Yukawa couplings with this parameterisation, we can therefore obtain the transformation rules between the mass and weak eigenstates

$$q_R^i = W_q^{ij} \tilde{q}_R^j, \;\; q_L^i = U_q^{ij} \tilde{q}_L^j, \tag{2.46}$$

where $\tilde{q}_{L/R}^i$ are the mass eigenstates. We therefore identify the quark masses as

$$m_q^i = \frac{1}{\sqrt{2}} M_q^{ii} v. \tag{2.47}$$

The discussion is not over at this point, however. We find that the mass matrices for up-type and down-type quarks are not simultaneously diagonalisable; *i.e.* $U_u \neq U_d$. This has serious implications for interaction terms involving both the up-type and down-type quarks—terms that also involve a $W^\pm$ boson. These interaction terms for the W^+ take the shape [47]

$$\frac{1}{2} \bar{u}_L^i \gamma^\mu d_L^i, \tag{2.48}$$

which in the mass eigenbasis looks like

$$\frac{1}{2} \bar{\tilde{u}}_L^i (U_u^\dagger U_d)^{ij} \gamma^\mu \tilde{d}_L^i. \tag{2.49}$$

Since U_q are individually unitary, the product $(U_u^\dagger U_d)^{ij}$ is also unitary; given that this product appears in terms involving flavour-changing interactions, the elements of this

matrix seem to act like the roots of transition probabilities between the flavours in u^i and d^i. We call this matrix the Cabibbo-Kobayashi-Maskawa (CKM) matrix, with the definition

$$V_{\text{CKM}} = U_u^\dagger U_d = \begin{pmatrix} V_{ud} & V_{us} & V_{ub} \\ V_{cd} & V_{cs} & V_{cb} \\ V_{td} & V_{ts} & V_{tb} \end{pmatrix}. \tag{2.50}$$

We see that whenever a W^+ boson enters an interaction, it brings with it a factor V_{CKM}. Conversely, the entry of a W^- boson brings a factor of V^*_{CKM}. Since every $W^\pm$ interaction brings this matrix with it, it is universal feature of flavour-changing charged currents; at least one matrix element should therefore enter every interaction that involves a change in quark flavour. Every decay should consistently feature the same values for the relevant entries of this matrix—this is a very strong constraint on the physics of the Standard Model and is a prime candidate for testing. The fact that this matrix is required to be unitary by definition constrains the possible values even further, and testing the unitarity of the CKM matrix is a principal direction of research today. The project presented in this thesis is one such contribution to this body of work.

In fact, we can form stronger constraints on the CKM matrix than those discussed already. The CKM matrix only has four independent parameters; we can absorb five into the quark fields (the sixth parameter that might be expected to also disappear must remain as an overall phase). There are many possible parameterisations; the "Standard" parameterisation is of three real mixing angles (θ_{12}, θ_{13}, θ_{23})and one *CP*-violating complex phase (δ_{13}). The CKM matrix in terms of these parameters reads

$$V_{\text{CKM}} = \begin{pmatrix} c_{12}c_{13} & s_{12}c_{13} & s_{13}e^{i\delta_{13}} \\ -s_{12}c_{23} - c_{12}s_{23}s_{13}e^{i\delta_{13}} & c_{12}c_{23} - s_{12}s_{23}s_{13}e^{i\delta_{13}} & s_{23}c_{13} \\ s_{12}s_{23} - c_{12}c_{23}s_{13}e^{i\delta_{13}} & -c_{12}s_{23} - s_{12}c_{23}s_{13}e^{i\delta_{13}} & c_{23}c_{13} \end{pmatrix}, \tag{2.51}$$

where $c_{ab} = \cos(\theta_{ab})$ and $s_{ab} = \sin(\theta_{ab})$. The complex phase δ_{13} is the only source of CP-violation in the Standard Model — CP-violation is theoretically also allowed in the quark-flavour sector but experimentally non-existent, which we will briefly outline when mentioning the Strong CP problem in section 2.4.2. It is important to note that there is no CP-violation in the case of a two-generation model of quarks, as is the case in the predecessor to the CKM matrix, the Cabibbo matrix [21]. Indeed, the motivation for extending the Cabibbo matrix by including a third generation of quarks in the Standard Model was expressly for the purpose of introducing a mechanism for CP-violation [22].

The sizes of the CKM matrix elements are strongly hierarchical, with the largest values along the principal diagonal of the CKM matrix, smaller entries on the first sub- and super-diagonals, and the remaining two elements being the smallest. This hierarchy is not immediately apparent in the "Standard" parameterisation, but an alternative

"Wolfenstein" parameterision [53]—useful for analytical approximations of the CKM matrix elements—makes this hierarchy explicit. The four Wolfenstein parameters are related to the "Standard" parameters by

$$\lambda = s_{12}, \quad A = s_{23}/s_{12}^2$$

$$\rho = \mathfrak{Re}\left(\frac{s_{13}e^{i\delta_{13}}}{s_{12}s_{13}}\right) \quad \eta = \mathfrak{Im}\left(\frac{s_{13}e^{i\delta_{13}}}{s_{12}s_{13}}\right)$$

where the quantities

$$s_{12} = \lambda \quad s_{23} = A\lambda^2 \quad s_{13}e^{i\delta_{13}} = A\lambda^3(\rho - i\eta)$$

are used to re-express the CKM matrix elements, to $\mathcal{O}(\lambda^4)$, as

$$V_{\text{CKM}} = \begin{pmatrix} 1-\lambda^2/2 & \lambda & A\lambda^3(\rho - i\eta) \\ -\lambda & 1-\lambda^2/2 & A\lambda^2 \\ A\lambda^3(1-\rho-i\eta) & -A\lambda^2 & 1 \end{pmatrix}. \tag{2.52}$$

The Wolfenstein parameters are all $\mathcal{O}(1)$ [4],

$$\lambda = 0.22653(48) \quad A = 0.799^{+0.027}_{-0.028} \quad \overline{\rho} = 0.141^{+0.016}_{-0.017} \quad \overline{\eta} = 0.357 \pm 0.011,$$

where $\bar{\rho} = \rho(1 - \lambda^2/2 + ...)$ and $\bar{\eta} = \eta(1 - \lambda^2/2 + ...)$, and the hierarchy of the CKM matrix elements manifests *via* the leading-order term in λ for each element.

To finish off, we will also note that the existence of neutrino masses requires additional terms in the Yukawa Lagrangian, which culminates in the introduction of an analogous matrix to the CKM matrix for neutrinos called the Pontecorvo–Maki–Nakagawa–Sakata (PMNS) matrix, needed to describe neutrino oscillations [54, 55].

2.4 QCD

In this section, we will describe QCD largely in isolation from electroweak theory in order to keep the discussion focused. We will make reference to electroweak theory where appropriate, however.

Quantum Chromodynamics (QCD) is the quantum theory of the strong force, which binds quarks together into composite particles (and provides the majority of the mass for these composite states). It is an SU(3) gauge theory of quark-gluon interactions. The QCD Lagrangian takes the form [47]

$$\mathcal{L}_{\text{QCD}} = -\frac{1}{4}G^{\mu\nu,a}G^a_{\mu\nu} + \bar{\psi}^i(i\not{D} - \frac{1}{2}m^2_{\psi})\psi^i, \tag{2.53}$$

where roman indices are "colour indices" spanning the SU(3) representation of the given object, the quark fields ψ are in the fundamental (triplet) representation of SU(3), forming "colour triplets"; and D_μ is the QCD covariant derivative

$$D_\mu \psi(x) = \partial_\mu \psi(x) + i g_S T^a A^a_\mu, \tag{2.54}$$

where g_S is the QCD coupling, T^a are the generators of SU(3) and A^a_μ are the gluon fields, which enter the field strength tensor

$$G^a_{\mu\nu} = \partial_\mu A^a_\nu - \partial_\nu A^a_\mu + i g_S f^{abc} A^b A^c, \tag{2.55}$$

where f^{abc} are the SU(3) structure constants. The gluon fields live in the adjoint (octet) representation of SU(3), and in the trivial (singlet) representation of the electroweak symmetries. As with $SU(2)_W$, the non-Abelian property of SU(3) introduces self-interaction terms between the gluons. By inspection, we can find three-gluon and four-gluon self-interaction terms in the Lagrangian, in addition to interaction terms involving two quarks and a gluon *via* the expansion of the covariant derivative. Although the fermion fields have a built-in mass term, there is no such term for the gluons, since it would not be SU(3)-invariant.

2.4.1 Confinement and Asymptotic Freedom

Roman indices in (2.53) indicate a "colour index", which takes 3 values for the quarks and 8 for the gluons. We call the three quark values "red", "green", and "blue", and anti-quarks carry "negatives" of these values we term "antired", "antigreen", and "antiblue". We can also define the gluon colour charges in terms of the quark charges *via* the construction of the adjoint representation, but there is not a unique way of doing this.

A curious property of colour-charged particles is that they exhibit a behaviour known as *colour confinement*, where at energies below the confinement scale $\lambda_{\text{Confinement}} \sim 300$ MeV [4] it is energetically favourable to form colour-neutral bound states. These bound states are termed *hadrons*. Colour-neutrality is achieved by grouping colour charges in red-green-blue triplets, or by pairing a colour with its anticolour. The colourless three-quark bound state is known as a *baryon*, and the colourless quark-antiquark pairs are known as *mesons*. These are not the only possible solutions; the first confirmed detection of a tetraquark state (composed of two quarks and two antiquarks) came in 2013 [56], and the first confirmed pentaquark state (comprising four quarks and an antiquark) was announced in 2015 [57], after an unreproducible 2003 result from LEPS. Colourless gluonic bound states, identified by various names such as *glueballs*, are also predicted by the Standard Model. In 2021, the discovery of a

three-gluon vector state was claimed by the TOTEM [58] and DØ [59, 60] experiments, following a joint analysis.

Colour confinement itself is a topic of great interest; it has no first-principles quantitative explanation and deep connections to other aspects of QCD. The fact that there is no first-principles explanation is rooted in the running of its coupling, g_S, with the energy scale. As described in detail in [61], the coupling strength of QCD decreases with an increasing energy scale. This means that at sufficiently low energies—or equivalently, sufficiently long distances—the theory becomes strongly coupled as $g_s \gtrsim 1$. This strong-coupling regime overlaps with the confinement scale, and renders a perturbative description of confinement inaccessible. Confinement is, at least, an emergent property of lattice QCD—a well-established non-perturbative description of QCD utilised by the project presented in this thesis—but this is insufficient for an analytic proof of confinement.

Confinement is also related to the mass gap problem in Yang-Mills theories. For QCD to exhibit a mass gap—*i.e.*, for there to exist no massless degrees of freedom orthogonal to the vacuum state—there can be no freely-propagating massless states. For 3 colour states, this implies that the gauge symmetry of QCD must be $\mathrm{SU}(3)$, rather than $\mathrm{U}(3)$, since $\mathrm{U}(3)$ Yang-Mills theory acts like $\mathrm{SU}(3)$ with an additional, non-interacting gluon. A singlet gluon state such as this would be freely-propagating, and result in no mass gap for QCD. The requirement of a mass gap for an interacting quantum Yang-Mills theory such as QCD has not been mathematically proven, and as such the role of confinement is highly relevant to the nature of the QCD gauge symmetry.

A second important feature of QCD is seen at high energies. As found in 1973 by Gross and Wilczek [62], and by Politzer [63], the coupling constant g_S decreases *logarithmically* with the energy scale — this is to say, the coupling constant asymptotically approaches 0 as $\mu \to \infty$. This behaviour is known as "asymptotic freedom" — the theory approaches the non-interacting limit as the energy scale increases. This avoids the existence of a pole at $\mu \to \infty$, and as such there are no obvious reasons why QCD should not be consistent at all energy scales μ. This is in contrast to QED, which does exhibit such a "Landau pole"; the resolution of the implied consistency problem is of great importance in quantum field theory.

2.4.2 Strong CP Problem

The QCD Lagrangian contains another term we have thus far omitted from (2.53) that removes unphysical dynamics resulting from a $\mathrm{U}(1)_\mathrm{A}$ axial symmetry of the

Lagrangian [64], which can be expressed in the form

$$\frac{3g_S^2\theta}{32\pi^2}G^{\mu\nu,a}G^a_{\mu\nu}, \tag{2.56}$$

where θ is a CP-violating "vacuum angle". This is a physically allowable second source of CP violation in the Standard Model, in addition to the CKM matrix discussed in section 2.3.6. However, experimental measurements of θ strongly constrain its value to zero [4]. There is no explanation for this in the Standard Model, and so this apparent coincidence is named the "Strong CP Problem". It is one more unresolved mystery in the Standard Model that is hoped to be explained by a successor theory. An SM extension known as Peccei-Quinn theory [65] is a popular proposed solution to the Strong CP Problem, which takes θ as an "axion field" rather than a "vacuum angle". Wilczek and Weinberg independently showed that the existence of this field introduces a new boson, the "axion" [66, 67], which also turns out to be a viable dark matter candidate [68]. Searches for the wide variety of axions proposed in the wake of Peccei-Quinn theory [68] are therefore highly important to the modern understanding of both QCD and cosmology.

Irrespective of the grand theoretical implications of this term, since experiment finds it to be negligible it is generally omitted from SM calculations; we similarly ignore this term in our Lattice QCD computations.

2.4.3 Quark Bilinears

As we have previously stated, the primary degrees of freedom in the confinement regime of QCD are quark bilinears. The symmetries of QCD require us to consider the existence of some transformation matrix Γ entering these bilinears, $\bar{\psi}\Gamma\psi$. There are 16 possible elements of this structure, which can be grouped into five bilinears shown in table 2.2 [47]. The structures transform differently under the Lorentz symmetry; the pseudo-scalars and pseudo-vectors transform similarly to the scalars and vectors respectively but pick up an additional minus sign. We can create or destroy particles with the desired quantum numbers by choosing the appropriate bilinear; for this project, we deal only the pseudo-scalar particles, but vector currents taking the form of a vector bilinear are also present in order to implement the weak interaction.

2.4.4 Approximate Chiral Symmetry

The Particle Data Group currently reports the $\overline{\text{MS}}$-scheme masses of the up, down, and strange quarks as $m_u = 2.16^{+0.49}_{-0.26}$ MeV, $m_d = 4.67^{+0.48}_{-0.17}$ MeV, and $m_s = 93^{+11}_{-5}$ MeV respectively [4]. These masses are well below the characteristic scale of quark confinement in the $\overline{\text{MS}}$ renormalisation scheme, $\Lambda_{\text{Confinement}} \sim 300$ MeV [4]. At this

Structure	Components	Transformation
1	1	Scalar
γ^μ	4	Vector
$\sigma^{\mu\nu} = \frac{1}{2}[\gamma^\mu, \gamma^\nu]$	6	Tensor
$\gamma^\mu\gamma^5$	4	Pseudo-vector
γ^5	1	Pseudo-scalar

TABLE 2.2: Quark bilinears of QCD.

energy scale, bound states of quarks become more useful degrees of freedom than the quarks themselves. Chiral perturbation theory is an effective theory of bound states of the pseudo-Nambu-Goldstone bosons of chiral symmetry breaking at low energies, which is discussed in section 2.5. Chiral perturbation theory is also foundational to *heavy meson* chiral pertubation theory, in which B and B_s mesons can be introduced as "matter fields" under the surviving $\mathrm{SU}(3)_V$ flavour symmetry, as we describe in section 4.2.1. We use this heavy meson extension to parameterise the physical limit of the $B_{(s)}$ decay simulations that constitute the main body of this thesis.

We can gain some insights into the behaviour of QCD by looking at the chiral limits $m_{u,d} \to 0$ and $m_{u,d,s} \to 0$. The light-quark Lagrangian (which describes the up and down quarks) takes the overall symmetry $\mathrm{SU(2)_L \times SU(2)_R \times U(1)_V \times U(1)_A}$. The axial $\mathrm{U(1)_A}$ symmetry is anomalous and is not a symmetry of QCD since it changes the measure in the path integral [47, 69], and the $\mathrm{U(1)_V}$ symmetry results in the conservation of baryon number. Interactions between the quarks and gluons of QCD lead the quark bilinears of (u, d) to acquire vacuum expectation values, which spontaneously breaks the chiral symmetry $\mathrm{SU(2)_L \times SU(2)_R}$ to the flavour symmetry $\mathrm{SU(2)_V}$, which we term *isospin*. Under this symmetry, the massless up and down quarks form a doublet:

$$Q = \begin{pmatrix} u \\ d \end{pmatrix}. \tag{2.57}$$

This also breaks the three generators of the doublet representation of $\mathrm{SU(2)_L \times SU(2)_R}$ to three massless Nambu-Goldstone bosons *via* Goldstone's Theorem [70]. Outside of the chiral limit, this symmetry is also *explicitly* broken by the non-zero quark masses; this instead generates three *massive* Nambu-Goldstone bosons, also termed *pseudo*-Nambu-Goldstone bosons. These three bosons are the $\pi^\pm$ and π^0 mesons. The differing electromagnetic charges of the up and down quarks provide an additional source of explicit chiral symmetry breaking and hence contribute to the mesonic masses, but at this energy scale the relative coupling strengths of the strong and electromagnetic forces implies that the amount of symmetry breaking due to electromagnetic effects is small compared to the strong force:

$$\mathcal{O}\left(\frac{\alpha_{\mathrm{EM}}}{\alpha_{\mathrm{S}}}\right) \sim \mathcal{O}(1/137) < 1\%. \tag{2.58}$$

This is generally below the statistical error of current lattice QCD simulations, including the ones presented in this document; and thus electromagnetic effects will not be discussed further. We note, however, that some lattice QCD calculations have now reached the level of precision at which both QED effects and isospin-breaking in the quark masses must be considered. We will instead accept this as a systematic error on the simulation results given that these effects are unresolvable for our purposes. For numerical reasons it is however useful to work in the isospin limit where the up and down quarks have the same, non-zero mass; this is discussed further in chapter 5.

The strange quark is also sufficiently light to be considered massless in the chiral limit to a good approximation; in this instance we take $(m_{u,d,s}) = 0$ which endows the Lagrangian for the up, down, and strange quarks with an $\mathrm{SU(3)_L} \times \mathrm{SU(3)_R} \times \mathrm{U(1)_V} \times \mathrm{U(1)_A}$ symmetry. The $\mathrm{U(1)_V}$ and $\mathrm{U(1)_A}$ are interpreted identically to the case with just the massless up and down quark, and we also have the $\mathrm{SU(3)_L} \times \mathrm{SU(3)_R}$ symmetry spontaneously break to an $\mathrm{SU(3)_V}$ flavour symmetry. Since we are now in the triplet representation of $\mathrm{SU(3)_V}$, there are eight generators that are broken, generating the $\pi^{\pm}, \pi^0, K^{\pm}, K^0, \bar{K}^0$, and η mesons. The explicit breaking of the chiral symmetry due to the mass and charge of the quarks is once again responsible for giving these mesons masses under the approximate chiral symmetry of QCD. The origin of these mesons as pseudo-Nambu-Goldstone bosons provides an explanation for the unusually small masses of these mesons compared to other hadrons.

2.5 Chiral Perturbation Theory

As noted in section 2.4.4, at energies below ~ 300 MeV the primary degrees of freedom of light quarks in QCD are bound states. We saw that the approximate chiral symmetry of the QCD Lagrangian for the three lightest quarks generates eight massive degrees of freedom, described by the meson octet $\pi^{\pm}, \pi^0, K^{\pm}, K^0, \bar{K}^0$, and η. Chiral perturbation theory [71, 72] gives us a language to describe these mesons in a perturbative manner, at the energy scale where individual quark fields are inaccessible to perturbation theory. As will be discussed in chapter 3, lattice QCD simulations are typically conducted at unphysical quark masses for computational efficiency; chiral perturbation theory tells us how chiral symmetry constrains the dependence of the masses and matrix elements of the of the eight pseudo-Nambu-Goldstone bosons on the quark (or pion) masses, providing us with fit functions for chiral extrapolations. It is worth noting that since the mass of the strange quark is significantly greater than the mass of the up and down quarks, an effective theory of just the up and down quarks should be more accurate than one that also approximates the strange as obeying a chiral symmetry. However, since such a theory only describes pion states,

the addition of the strange is necessary for the description of kaon states. If the kaon states can be ignored, then SU(2) chiral perturbation theory is a sufficient description.

Chiral perturbation theory describes the octet field

$$\Pi = \begin{pmatrix} \frac{\pi^0}{\sqrt{2}} + \frac{\eta}{\sqrt{6}} & \pi^+ & K^+ \\ \pi^- & -\frac{\pi^0}{\sqrt{2}} + \frac{\eta}{\sqrt{6}} & K^0 \\ K^- & \bar{K}^0 & -\frac{2\eta}{\sqrt{6}} \end{pmatrix}, \tag{2.59}$$

which obeys the chiral symmetry $SU(3)_V$. The effective Lagrangian is written in terms of the unitary field

$$\Sigma = \exp\left(\frac{2i\Pi}{f}\right), \tag{2.60}$$

where f is the pion decay constant.

2.6 Weak Decay Effective Hamiltonians

The characteristic scale of QCD for three light quark flavours is $\Lambda_{QCD} \sim \mathcal{O}(200\ \text{MeV})$, which describes the point at which perturbation theory begins to fail and non-perturbative techniques must be used. The mass of the $W^\pm$ bosons are ~ 80.3 GeV [4]; the distance traversed by the $W^\pm$ from the perspective of Λ_{QCD} is exceptionally small. Moreover, current Lattice QCD scales can typically resolve masses up to 2-4 GeV; the $W^\pm$ bosons are simply too heavy to simulate on the lattice. For these reasons, lattice QCD (and other low-energy descriptions) employs an effective Hamiltonian that "integrates out" the $W^\pm$, Z, and top quarks, treating flavour-changing charged interactions as point-like contact terms [73]. Such an approximation is also known as Fermi effective theory, given its relation to Fermi's theory of the weak interaction that preceded the notion of massive bosons and electroweak theory.

To first order, the effective Hamiltonian from the operator product expansion [74–76] is

$$\mathcal{H}_{\text{eff}} = \frac{G_F}{2} \sum_n V_{\text{CKM}}^{(n)} C^{(n)}(\mu) O^{(n)}(\mu), \tag{2.61}$$

where G_F is Fermi's constant, $V_{\text{CKM}}^{(n)}$ are elements of the CKM matrix, $C^{(n)}(\mu)$ are "Wilson Coefficients" that are a function of the renormalisation scale $\mu \gg \Lambda_{QCD}$ and describe the influence of factors above this scale, and $O^{(n)}(\mu)$ are local operators implementing the flavour-changing contact term. The Wilson coefficients are process-agnostic; they are also calculable in perturbation theory thanks to the requirement that the renormalisation scale is well above Λ_{QCD}.

2.7 Semileptonic Decays

2.7.1 Decay Equations

The processes studied in this project are $B \to \pi\ell\nu$ and $B_s \to K\ell\nu$ semileptonic decays, and so we should at this point discuss the phenomenology of semileptonic decays in the SM. The tree-level differential decay rate equations—neglecting electromagnetic effects—for both processes follow the same shape:

$$\frac{d\Gamma(B_{(s)} \to P\ell\nu)}{dq^2} = \frac{G_F^2|V_{ub}|^2}{24\pi^3}\frac{(q^2-m_\ell^2)^2\sqrt{E_P^2-M_P^2}}{q^4 M_{B_{(s)}}}\times \left[\left(1+\frac{m_\ell^2}{2q^2}\right)M_{B_{(s)}}^2(E_P^2-M_P^2)\left|f_+(q^2)\right|^2 + \frac{3m_\ell^2}{8q^2}\left(M_{B_{(s)}}^2-M_P^2\right)^2\left|f_0(q^2)\right|^2\right], \quad (2.62)$$

where $B_{(s)}$ is the B or B_s meson, P is either the K or π final state, q is the momentum transfer from the initial state to the $W^\pm$ boson, G_F is Fermi's constant, and f_+ & f_0 are semileptonic form factors for the particular decay mode.

Most quantities in (2.62) are known to a good precision, with averages provided by the Particle Data Group [4] and the Flavour Lattice Averaging Group [77]. Four quantities remain that require particular attention. These are the differential decay rate, which is measured at LHCb and b-factories; $|V_{ub}|$, the CKM matrix element which is a primary target of this study; and the two QCD form factors f_+ and f_0. The form factors are low-energy quantities that summarise the effect of QCD on the decay rate of one meson into another, and must be computed non-perturbatively. Lattice QCD can be applied to compute these form factors; determining the implied value of $|V_{ub}|$ is then possible by inserting these numbers into (2.62) along with the latest averages for the decay rate from experiment.

Since the CKM matrix should be unitary—as seen in section 2.3.6—the determination of $|V_{ub}|$ should, when added in quadrature with the remaining elements of the appropriate row or column of the CKM matrix, sum to 1. A deviation from this quantity is a strong indicator of new physics, and by decreasing the error on both the form factors and the differential decay rate we may see such a deviation emerge from the statistics. As mentioned in chapter 1, there are several tensions involving $|V_{ub}|$ — and at present, $|V_{ub}|$ is the least precisely determined matrix element.

The 2–3σ tension between $|V_{ub}|$ determinations from inclusive and exclusive semileptonic decay modes has, at the time of writing, stood for over a decade. The 2021 FLAG report gives an average for the exclusive determination at $|V_{ub}|^{\text{excl.}} = 3.74(17) \times 10^{-3}$ [77]—a change from $|V_{ub}|^{\text{excl.}} = 3.43(14) \times 10^{-3}$ in the 2019 report [78]—and the PDG gives value of $|V_{ub}|^{\text{incl.}} = 4.49(28) \times 10^{-3}$ for the inclusive

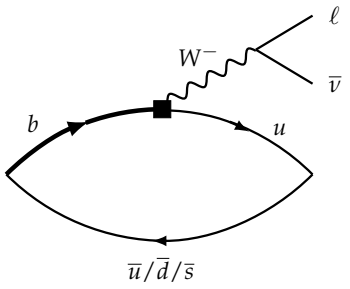

FIGURE 2.1: The tree-level Feynman diagram of $B_{(s)} \to P\ell\nu$ decays. The CKM matrix element $|V_{ub}|$ enters at the quark-W interaction vertex. The hadronic part of this diagram is a three-point function of three quark propagators, which can be decomposed in terms of QCD form factors.

mode [4]. Moreover, an alternative determination from leptonic decay modes sits at $|V_{ub}|^{\text{lep.}} = 4.03(37)(3) \times 10^{-3}$ [4]; close to halfway between the two semileptonic results and statistically compatible with both. Further muddying the picture is a recent analysis from the Belle collaboration, $|V_{ub}|^{\text{excl.}} = 4.10(09)(22)(15) \times 10^{-3}$ [79], a mere 1.3σ above the semileptonic result. Although more recent results appear to be converging, more work must be done to ensure that the tension is decreasing. As such, future developments on the horizon will provide more input on $|V_{ub}|$. Aside from the programme of steadily improving lattice QCD results, the Belle-II experiment continues to study B decays, and is expected to have a lifetime production of 50 ab of collision data [80].

2.7.2 Form factor definitions

The QCD form factors in (2.62) enter as a result of the hadronic interaction in the decay, which is depicted in figure 2.1. We can therefore assess the hadronic part of the decay in isolation in order to study the form factors. To do this, we can perform a standard parameterisation of the hadronic matrix element $\langle P|V^\mu|B_{(s)}\rangle$,

$$\langle P|V^\mu|B_{(s)}\rangle = f_+(q^2)\left(p^\mu_{B(s)} + p^\mu_P - \frac{M^2_{B_{(s)}} - M^2_P}{q^2}q^\mu\right) + f_0(q^2)\left(\frac{M^2_{B_{(s)}} - M^2_P}{q^2}q^\mu\right), \tag{2.63}$$

where V^μ is the $b \to u$ flavour-changing vector current, $p_{B_{(s)}}$ is the momentum of the $B_{(s)}$ meson, p_P is the momentum of the P meson, and q^μ is the momentum transfer to the $W^\pm$ boson. The momentum transfer is therefore defined by

$$q^2 = (p^\mu_{B_{(s)}} - p^\mu_P)^2. \tag{2.64}$$

The calculation of these hadronic matrix elements forms the core focus of our Lattice QCD computations, with the goal of extracting $f_+(q^2)$ and $f_0(q^2)$ in the continuum for all allowed q^2.

2.7.3 Experimental Status

The Particle Data Group (PDG) provides averages for $B \to \pi\ell\nu$ decay rates, using data from several experimental collaborations [4], and the Heavy Flavour Averaging Group (HFLAV) also provides averages for heavy-quark decay channels [6]. The current PDG average for the $B^0 \to \pi^-\ell^+\nu_\ell$ fractional decay rate is 1.50(06) $\times 10^{-4}$, using BaBar [81–83], Belle [84–86], and CLEO2 [87] data. The average for the $B^+ \to \pi^0\ell^+\nu_\ell$ fractional decay rate is 7.80(27) $\times 10^{-5}$, using BaBar [81–83], and Belle [84, 86] data. These stand at a 4% and 3.5% error respectively. Taking into account the isospin factor relating these decays, one would expect to find

$$\frac{\mathcal{B}(B^+)}{\mathcal{B}(B^0)} = \frac{\tau_{B^+}}{2\tau_{B^0}}, \tag{2.65}$$

where τ is the lifetime of the subscript particle. These ratios respectively evaluate to ~ 0.52 and ~ 0.54 using PDG averages [4], confirming this expectation.

The first experimental semileptonic $B_s \to K$ results, using the ratio of $B_s \to K$ to $B_s \to D_s$ decay rates, were published in early 2021 by the LHCb collaboration [88] and reported by HFLAV. LHCb gives a branching fraction of $1.06(05)(08) \times 10^{-4}$ for $B_s^0 \to K^-\mu^+\nu_\mu$; an error of $\sim 9\%$.

The Belle-II experiment is also actively collecting data and should provide new experimental input on these decay modes, among many others, in the upcoming years. The first measurement of $B_s^0 \to K^-\ell^+\nu_\ell$ is anticipated *via* the $\Upsilon(5S)$ resonance, with an estimated 5-10% error for 1 ab^{-1} of data collected at $E_{\text{CM}}(\Upsilon(5S))$.

The Belle collaboration also provides forecasts for the precision of $|V_{ub}|$ estimates from future lattice and Belle-II data. From the exclusive $B \to \pi\ell\nu$ channels, an uncertainty of 1.0-1.7% in 10 years is predicted, down from 3.6-6.2% today, depending on the method used and whether electromagnetic effects are included or not. The projection for a determination from $B_s \to K\ell\nu$ in 5 years—no 10-year-projection is given—is put at 4.5-4.7%, depending on whether electromagnetic effects are included. An estimate of 3.0-4.8% on the precision of $|V_{ub}|$ in 10 years from inclusive processes is also given, mostly driven by an estimated 2.5-4.5% uncertainty in theoretical inputs.

2.7.4 Lattice Status

Presently, the Flavour Lattice Averaging Group uses results from three independent computations of the $B_s \to K\ell\nu$ [89–91] and $B \to \pi\ell\nu$ [90, 92, 93] form factors, a detailed summary of which can be found in the 2019 FLAG report [78]. The form factors are expressed in terms of parameterised functions which are discussed in detail in section 4.2.2. The dominant parameter in the case of $B \to \pi\ell\nu$ has an error of 3.2%,

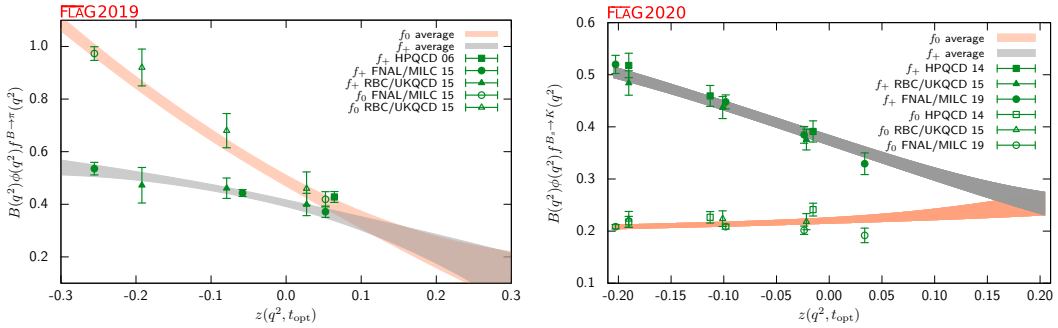

FIGURE 2.2: Flavour Lattice Averaging Group averages [78] for the $B_s \to K\ell\nu$ [89–91] and $B \to \pi\ell\nu$ [90, 92, 93] f_+ and f_0 form factors. The variable z is a function of q^2, used to parameterise the extrapolation of lattice results across all accessible q^2, as discussed in section 4.2.2.

which has decreased from 7.3% in the 2015 edition of the FLAG report [94]. There is a similar error of 3.8% for $B_s \to K\ell\nu$ [78].

The results of this project will update the RBC/UKQCD data points [90] in both of these averages. The FLAG average suggests that results with an error of $\sim 4\%$ on the dominant contributions to the form factor descriptions would constitute a valuable addition to the available body of work.

Chapter 3

Lattice QCD

3.1 Introduction

As we have discussed in the previous chapter, ground-state weak decays commonly occur on an energy scale at which QCD is inaccessible to perturbation theory. Effective theories such as chiral perturbation theory can approximate the behaviour of bound states at these energy scales; but these are not exact formulations of QCD expressed in terms of the fundamental fields that compose it. In this section, we will introduce lattice QCD — a first-principles, systematically improvable formulation of QCD that exhibits a well-defined reduction to continuum QCD in a suitable limit. Lattice QCD is expressed in terms of the path integral formulation of quantum field theories, where the definitions of n-point correlation functions are given by

$$\langle \mathcal{O}_1 ... \mathcal{O}_n \rangle = \frac{1}{Z} \int \mathcal{D}[A, \psi, \bar{\psi}] \mathcal{O}_1 ... \mathcal{O}_n e^{iS[A,\psi,\bar{\psi}]}, \tag{3.1}$$

where S is the action, and the partition function Z is

$$\int \mathcal{D}[A, \psi, \bar{\psi}] e^{iS[A,\psi,\bar{\psi}]}. \tag{3.2}$$

We will begin in section 3.2 with a brief overview of the formulation and observables of Lattice QCD. In section 3.3 we will address how to simulate the discretised path integral, and in 3.4 we consider the problem of inverting the very large Dirac matrices we encounter. In section 3.5 we will introduce the version of lattice QCD formulated by Wilson, before expanding this in section 3.6 to consider additional ways of discretising the QCD action that solve issues with the Wilson formulation. In section 3.7 we will discuss how to build correlation functions in lattice QCD from these actions, and we conclude in section 3.8 by describing the required renormalisation conditions. Much of this chapter is based on the textbook by Gattringer and Lang [95], which provides a more comprehensive introduction to these topics.

3.2 The Path Integral on the Lattice

3.2.1 Discretisation of Space-Time

When attempting to make calculations with the path integral in perturbation theory, one quickly runs into divergent terms in the resultant expressions. These take the form of ultraviolet (UV) divergences that are induced by unbounded momenta (such as those in loops), and infra-red (IR) divergences that appear for massless fields with vanishing momenta. In perturbation theory, these are dealt with using tricks such as introducing a momentum-cutoff, Pauli-Villars regularisation [96], and the dimensional regularisation procedure [97–99]. As Kenneth Wilson found in 1974, it is also possible to establish a non-perturbative gauge-invariant regularisation of the path integral by introducing minimum and maximum length scales in the form of a space-time lattice [7].

These lattices are usually square in the spatial dimensions and elongated in the temporal dimension such that there are $N^3 \times N_T$ lattice sites, where N is the number of lattice sites assigned to each spatial dimension, and N_T is the number of sites for the time dimension. In order to resolve dynamics around the energy scale of interest Λ, we require that

$$\frac{1}{aN} \ll \Lambda \ll \frac{1}{a}, \tag{3.3}$$

where a is the separation between lattice sites (or more succinctly, the "lattice spacing"). Since we typically use Lattice QCD to study hadronic bound states, the relevant energy scale is the confinement scale, Λ_{QCD}, or a characteristic mass scale around the nucleon mass of 1 GeV. Chiral perturbation theory power counting also suggests a scale of $4\pi f_\pi \sim 1$ GeV. The finite, discrete lattice of points introduces natural cut-offs for infra-red and ultraviolet divergences in the theory; the lattice cannot resolve states with energies greater than $1/a$, and states with energies lower than $1/aN$ do not fit in the finite volume, and so we must make sure these scales are sufficiently separated. Additional restrictions on these bounds may demanded be the physics of interest, and we will see in section 3.6.2 that simulating quarks with b-like masses places very expensive constraints on the lattice spacing if we do not use additional tricks. Lattice calculations commonly take $N_T = 2N$; however, this is not a strict rule.

Since space-time is discretised, the action of the theory is a sum of the Lagrangian over lattice sites rather than an integral over continuous space-time; *i.e.* we take

$$\int d^4x \to a^4 \sum_n , \tag{3.4}$$

where n is a lattice site labelled with 4 integers for the 4 space-time dimensions of the lattice.

3.2.2 Gauge Links

We should take care to ensure that the fermion fields transform correctly under their gauge symmetries on the lattice. The fermions are invariant under an SU(3) transform, so we should build a discrete covariant derivative that obeys this property, similar to the continuum case. To begin, we will replace the space-time derivative with a central difference:

$$\partial_\mu \psi(x) \to \Delta_\mu \psi(x) = \frac{\psi(x + a\hat{\mu}) - \psi(x - a\hat{\mu})}{2a}, \tag{3.5}$$

where $\hat{\mu}$ is a unit vector in the direction of μ. In order to preserve SU(3) invariance, we introduce the quantity $\mathrm{U}_\mu(x)$, which transforms as

$$U_\mu(x) \to \Omega(x) U_\mu(x) \Omega^\dagger(x + a\mu), \tag{3.6}$$

where $\Omega(x)$ is an SU(3) transform for a particular lattice site. We can then add this factor to (3.5) as

$$\Delta_\mu \psi = \frac{U_\mu(x)\psi(x + a\hat{\mu}) - U_{-\mu}\psi(x - a\hat{\mu})}{2a}, \tag{3.7}$$

where $U_{-\mu}(x) = U_\mu^\dagger(x - a\mu)$, to generate SU(3)-invariant terms in the Lagrangian.

This new quantity $U_\mu(x)$ is related to the gauge field as

$$U_\mu(x) = e^{i g_S a A_\mu(x)}. \tag{3.8}$$

Since $U_\mu(x)$ is an element of SU(3) and A_μ is an element of the Lie algebra of Equation (3.8) implies that the gauge fields do not live on the lattice sites like the fermion fields, but rather on the *links* between the sites. For this reason, $U_\mu(x)$ is generally termed the "link variable".

The transformation property is also similar for any consecutive series of gauge links:

$$U_\mu(x) U_\nu(x + a\hat{\mu}) \to \Omega(x) U_\mu(x) \Omega^\dagger(x + a\hat{\mu}) \Omega(x + a\hat{\mu}) U_\nu(x + a\hat{\mu}) \Omega^\dagger(x + a\hat{\mu} + a\hat{\nu}), \tag{3.9}$$

$$= \Omega(x) U_\mu(x) U_\nu(x + a\hat{\mu}) \Omega^\dagger(x + a\hat{\mu} + a\hat{\nu}), \tag{3.10}$$

By chaining a number of link variables in a closed loop, the Ω transforms at the left and right sides of this expression become $\Omega(x)$ and $\Omega^\dagger(x)$ respectively. Therefore, the trace of a closed path is gauge invariant, since these remaining transforms cancel under the cyclicity of the trace. Such an object is called a *Wilson loop* [7]; these are

essential to a successful description of the gauge sector in the action, as we will discuss in section 3.5.1.

3.2.3 Euclidean Space-Time

An integrand of the form e^{ix} is numerically unstable; it is an oscillatory function and therefore experiences a high degree of cancellation between contributions to the sum — a situation commonly termed "the Sign Problem". Fortunately, we can sidestep this issue by Wick rotating the integrand of (3.1) from Minkowski space-time to Euclidean space-time by making the replacement $t \to it_E$. Since the action is real-valued, the exponential factor also becomes real-valued, and now resembles a Boltzmann factor attached to the particular path it is evaluated for. We have therefore reduced QCD to an exercise in numerical integration; we compute the weight for each path we choose to evaluate and add it to the integral.

This also has the consequence that time can be treated like a fourth spatial dimension of the lattice. From this point onwards, equations and definitions involving the variable t in the context of lattice QCD computations refers to this Euclidean time. As an aside, we also note that the finite Euclidean time can also be mapped to a finite temperature.

3.2.4 Grassmann Variables and Wick's Theorem

Fermions obey Fermi statistics; that is to say, fermions obey an anti-commutation relation. Fermions are representable by anti-commuting Grassmann numbers — *i.e.* the fermion fields obey

$$\theta_1\theta_2 = -\theta_2\theta_1, \tag{3.11}$$

where θ_1 and θ_2 are Grassmann numbers. These variables behave in interesting ways under integration; one result crucial to the formulation of lattice QCD is the Matthews-Salam formula [100, 101], which proves that a Gaussian integral of Grassmann variables is a matrix determinant:

$$\int \left(\prod_k^N d\theta_k d\bar{\theta}_k \right) \exp\left\{ \sum_{i,j}^N \bar{\theta}_i M_{ij} \theta_j \right\} = -\det[M]. \tag{3.12}$$

By Wick rotating the QCD path integral to Euclidean space-time, we can find similar factors appearing in the lattice QCD path integral, with the matrix M as the Dirac operator. However, we typically deal with fermions of multiple flavours in the path integral, and we also have additional factors of the fermion fields appearing in the

integral from the observables we wish to compute the expectation values of:

$$\langle \overline{\theta}_{i_1} \theta_{j_1} ... \theta_{i_n} \overline{\theta}_{j_n} \rangle = \frac{1}{Z_F} \int \left(\prod_k^N d\theta_k d\overline{\theta}_k \right) \left(\overline{\theta}_{i_1} \theta_{j_1} ... \theta_{i_n} \overline{\theta}_{j_n} \right) \exp \left\{ \sum_{m,l}^N \overline{\theta}_m M_{ml} \theta_l \right\} \tag{3.13}$$

The applicability of the Matthews-Salam formula to the path integral can be extended *via* Wick's theorem [102]:

$$\frac{1}{Z_F} \int \left(\prod_k^N d\theta_k d\overline{\theta}_k \right) \left(\overline{\theta}_{i_1} \theta_{j_1} ... \theta_{i_n} \overline{\theta}_{j_n} \right) \exp \left\{ \sum_{m,l}^N \overline{\theta}_m M_{ml} \theta_l \right\} = (-1)^n \sum_{P(1,2,...,n)} \text{sign}(P) \prod_k^N \left(M^{-1} \right)_{i_k, j_{P_k}}, \tag{3.14}$$

where P is a permutation of the Grassmann fields. This expression is only non-zero for equal numbers of indices i and j, such that the Grassmann variables are required to come in pairs — *i.e.* quark bilinears. The number of pairs N defines the number of propagators in the correlation function.

This expression can also be depicted using an alternative notation which we will employ in later sections and introduce now. For a given expectation value of N fermion-antifermion pairs—let us use three for this illustration—we can systematically enumerate all terms of the sum as all possible permutations of *Wick contractions* of Fermion fields

$$\langle \theta_3 \overline{\theta}_3 \theta_2 \overline{\theta}_2 \theta_1 \overline{\theta}_1 \rangle = \langle \overbrace{\theta_3 \overline{\theta}_3} \overbrace{\theta_2 \overline{\theta}_2} \overbrace{\theta_1 \overline{\theta}_1} \rangle + \langle \overbrace{\theta_3 \overline{\theta}_3} \overbrace{\theta_2 \overline{\theta}_2 \theta_1 \overline{\theta}_1} \rangle + \langle \overbrace{\theta_3 \overline{\theta}_3 \theta_2 \overline{\theta}_2} \overbrace{\theta_1 \overline{\theta}_1} \rangle + \langle \overbrace{\theta_3 \overline{\theta}_3 \theta_2 \overline{\theta}_2 \theta_1 \overline{\theta}_1} \rangle + \langle \overbrace{\theta_3 \overline{\theta}_3 \theta_2 \overline{\theta}_2 \theta_1 \overline{\theta}_1} \rangle + \langle \overbrace{\theta_4 \overline{\theta}_3 \theta_2 \overline{\theta}_2 \theta_1 \overline{\theta}_1} \rangle, \tag{3.15}$$

where the pair

$$\overbrace{\theta_i \overline{\theta}_j} \tag{3.16}$$

is a *Wick Contraction* of the variables θ_i and $\overline{\theta}_j$. In order to enumerate all contributing terms, we simply have to form all possible Wick contractions of the fermion fields. The Wick contraction of fermion fields of different flavour is zero, and as such we can discard terms involving such contractions and only look for possible ways to "pair up" fermion fields of the same flavour.

The Wick contraction defines which fermion fields enter a particular inverse Dirac operator in the sum in (3.14); *i.e.* it is a pictoral representation of the spin indices of a Dirac matrix. To find the sign of a term due to its particular permutation of fermion fields, we simply anti-commute the fermion fields until all Wick contraction lines are

"disentangled" — when contracted fermion fields are neighbouring each other as $\theta_i\overline{\theta}_j$:

$$\langle \theta_3\overline{\theta}_3\theta_2\overline{\theta}_2\theta_1\overline{\theta}_1\rangle = -\langle \theta_3\overline{\theta}_1\theta_1\overline{\theta}_3\theta_2\overline{\theta}_2\rangle \tag{3.17}$$

$$= -\left\langle M_{31}^{-1}M_{13}^{-1}M_{22}^{-1}\right\rangle \tag{3.18}$$

$$= -\left\langle \mathrm{Tr}\left[M_{31}^{-1}M_{13}^{-1}\right]\mathrm{Tr}\left[M_{22}^{-1}\right]\right\rangle \tag{3.19}$$

where in the first line the minus sign comes from the odd number of permutations of fermion fields required order to re-arrange the fields, in the second line we express the fields in terms of the inverse Dirac operators, and in the third line we make explicit the fact that the indices of the inverse Dirac operators contract to make traces. Computing these Dirac operators are, therefore, critical to performing lattice QCD calculations.

3.2.5 The Lattice QCD Path Integral

The preceding definitions are sufficient for us to write down a "lattice" version of the QCD path integral for some observable $\mathcal{O}$, in which we can separate the "fermion" terms from the "gauge" terms to exploit the Grassmann nature of the fermion fields:

$$\langle\mathcal{O}\rangle = \frac{1}{Z}\int \mathcal{D}[\overline{\psi}\psi]\mathcal{D}[U]e^{-S_F[\overline{\psi}\psi U]}e^{-S_G[U]}\mathcal{O}[\overline{\psi}\psi U], \tag{3.20}$$

where the partition function Z is given by

$$Z = \int \mathcal{D}[\overline{\psi}\psi]\mathcal{D}[U]e^{-S_F[\overline{\psi}\psi U]}e^{-S_G[U]}, \tag{3.21}$$

and the fermion action S_F is

$$S_F = \sum_f \overline{\psi_f}D_f[U]\psi_f, \tag{3.22}$$

and D_f is the Dirac matrix for the quark flavour f.

We can factorise this integral into a fermionic and a gauge part also, with the Fermion path integral given by

$$\langle\mathcal{O}\rangle_F = \frac{1}{Z_F[U]}\int \mathcal{D}[\overline{\psi}\psi]e^{-S_F[\overline{\psi}\psi U]}\mathcal{O}[\overline{\psi}\psi U], \tag{3.23}$$

with the Fermion partition function

$$Z_F[U] = \int \mathcal{D}[\overline{\psi}\psi]e^{-S_F[\overline{\psi}\psi U]}. \tag{3.24}$$

The integration measure $\mathcal{D}[\overline{\psi}\psi]$ is a product of infinitesimal-Grassmann-variable pairs, the function $\mathcal{O}$ is of Grassmann variable pairs, and the Fermion action is a Gaussian exponent involving the Dirac operator. This allows us to use Wick's

Theorem (3.14) to integrate out the fermion fields, leaving us with the integral

$$\langle \mathcal{O} \rangle = \frac{\int \mathcal{D}[U] e^{-S_G[U]} \prod_f \det[D_f] \mathcal{O}[U, D_f^{-1}]}{\int \mathcal{D}[U] e^{-S_G[U]} \prod_f \det[D_f]}, \tag{3.25}$$

reducing the involvement of the fermions to the Dirac operator. The integration measure we are left with, $\mathcal{D}[U]$, is a *Haar measure*. The Lattice QCD Haar measure defines the path integral over the SU(3)-valued gauge links, allowing us to perform gauge-invariant integration over the SU(3) group. We will not discuss the details of these integrals, such as how they tell us how to integrate out common links between pairs of Wilson loops to "merge" them, but a good introduction can be found in *e.g.* [95].

3.3 Simulating the Path Integral

3.3.1 Monte-Carlo Integration

Monte-Carlo integration is a technique for integrating expressions by summing evaluations of the expression at random points in its domain. By doing so, we can evaluate the average value of the function. To recover the original integral, we need only multiply through by the volume of the domain. Mathematically, we can say

$$\int_a^b f(x)dx = V\langle f \rangle = \lim_{N\to\infty} \frac{V}{N} \sum_{n=0}^{N-1} f(x_n), \tag{3.26}$$

where we can also state the volume factor as the sum over the domain

$$V = \int_a^b dx. \tag{3.27}$$

We use Monte-Carlo integration because its error scales as $\mathcal{O}(N^{-1/2})$—that is to say, the error reduces by a factor of two when we include four times as many points in the integral. This may seem like very poor scaling behaviour, but when compared to other techniques Monte-Carlo is the clear winner for lattice QCD, purely because the error scaling has no dependence on the dimensionality of the problem. By comparison, quadrature methods commonly have error scalings of $\mathcal{O}(N^{-2/d})$, $\mathcal{O}(N^{-4/d})$, and so forth. For a very highly-dimensional integral such as the lattice QCD path integral—where the integration variables are paths of gauge links, not just spatial dimensions—these techniques are quickly overcome by the so-called "curse of dimensionality".

Returning to the path integral, we note that the main difference between the provided Monte-Carlo definitions and the path integral is the fact that we also have additional

terms multiplying the observable $f(x)$ in the integral, in the form of a Boltzmann factor e^{-S_G} and fermion determinants. These factors are variable, and provide a "weight" for every potential contributing point to the Monte-Carlo sum — some integration points are much more valuable than others, because they have a higher weight and are hence larger contributions to the average. If we can bias our random-number generator to preferentially select these more highly-weighted contributions, we will more quickly converge on an acceptable answer. Such a technique is known as "importance-sampling", and it operates by selecting samples from a non-uniform probability distribution.

For simplicity, let us first neglect the Fermion determinants when attempting to apply importance sampling to the path integral. First we can note that by introducing a weight in the sum, we must also introduce a corresponding weight in the volume factor in order for it to correctly reproduce the sampled region

$$\langle f \rangle = \frac{\int_a^b \rho(x) f(x)}{\int_a^b \rho(x) dx}. \tag{3.28}$$

We can re-parameterise the integral measure as a normalised probability density,

$$dP(x) = \frac{\rho(x)dx}{\int \rho(x)dx}, \tag{3.29}$$

and therefore express the expectation value of f as

$$\langle f \rangle = \int_a^b dP(x) f(x) = \lim_{N\to\infty} \frac{1}{N} \sum_{n=0}^{N-1} f(x_n), \tag{3.30}$$

where the x_n are generated by the probability density $dP(x)$.

Our path integral is already of the form in (3.28), and we can identity the integration measure as $\mathcal{D}[U]$, the observable as $\mathcal{O}[U, D^{-1}]$ and the weight (for now) as e^{-S_G}. The probability density used to select gauge ensembles is the *Gibbs measure*,

$$dP[U] = \frac{\mathcal{D}[U] e^{-S[U]}}{\int \mathcal{D}[U] e^{-S[U]}}. \tag{3.31}$$

We will address the inclusion of the fermion determinants in this distribution in sections 3.3.3 and 3.3.4.

We are left with the expression

$$\langle \mathcal{O} \rangle = \lim_{N\to\infty} \frac{1}{N} \sum_{n}^{N} \mathcal{O}[U_n, D^{-1}], \tag{3.32}$$

and the question now is how to generate our new integration variables U_n from the Gibbs measure.

3.3.2 Markov Chains

We can generate paths U_n by starting from an arbitrary path of gauge links, and moving towards one that follows the required distribution by using the Markov chain process to probabilistically perturb the links to a new path configuration. The distinguishing feature of a Markov chain is 'memoryless-ness" — the probability of choosing a particular next step in the Markov chain of configurations between our arbitrary path and the final result depends only on the current state and proposed next state of the path. By carefully considering how to construct the transition probability between update steps, we can formulate a Markov chain process that will guide our starting guess towards the region of configuration-space that carries the highest weight.

We can define the probability of selecting a particular next update step with the transition probability

$$P(U_n = U'|U_{n-1} = U) = T(U'|U). \tag{3.33}$$

Furthermore, we require that the equilibrium state does not preferentially select some direction, so the probability of reversing an update step must be equal to the probability of traversing it. This is expressed in the *balance equation*

$$\sum_U T(U'|U)P(U) = \sum_U T(U|U')P(U'), \tag{3.34}$$

and taking the right-hand sum shows that

$$\sum_U T(U'|U)P(U) = P(U'), \tag{3.35}$$

since

$$\sum_U T(U|U') = 1. \tag{3.36}$$

This shows that P(U) is a fixed point of the system, and will be gradually evolved towards as more update steps are applied to an arbitrary starting configuration.

However, we do not necessarily have access to all configurations required to satisfy (3.34) at a given point in time. We can instead formulate a Markov chain on the requirement that this holds term-wise with the *detailed balance condition*

$$T(U'|U)P(U) = T(U|U')P(U'). \tag{3.37}$$

Given this problem, a typical lattice calculation will employ a certain number of *thermalisation steps* to allow the algorithm to converge to equilibrium.

We now need some rule to generate the transition probabilities $T(U)$. The Metropolis algorithm is one method for deciding whether to accept a proposed configuration as the next step in the Markov chain. The transition probability between the current configuration U and proposed configuration U' for a probability distribution $\rho(U)$ can be expressed as

$$T_{i+1}(U'|U) = \min\left(1, \frac{T_i(U|U')\rho(U')}{T_i(U'|U)\rho(U)}\right), \tag{3.38}$$

where the min clamps the probability to $\leq 100\%$.

3.3.3 Revisiting the Fermion Determinant

Having discussed the generation of integration variables in the absence of fermion determinants, we now turn to the issue of including them. We should note that all we have discussed so far is equivalent to setting the Dirac matrices to unit matrices; this is known as the "quenched approximation", since the determinants can be expressed as

$$\det[D_f] = e^{\mathrm{Tr}[\ln(D_f)]} = e^{\mathrm{Tr}[D_f^{-1}]} = e^{-S_F^{\mathrm{eff}}}, \tag{3.39}$$

which represents a Dirac matrix with identical quantum numbers on its indices. In this case, the Dirac matrix is of a single quark that pops out the vacuum and returns to its source — a vacuum fluctuation. Setting these Dirac matrices to one removes these "sea-quark" effects from the simulation, "quenching" these excitations.

Modern simulations normally include the fermion determinants in the generation of gauge configurations, in what are called "Dynamical Fermion" calculations. With the inclusion of sea-quarks, we can capture contributions to observables resulting from sea-quark interactions. The determinant is generally folded into the probability distribution because treating it as an observable confounds the importance sampling, since the determinant can cover many orders of magnitude depending on the particular gauge configuration. However, including the determinant in the Gibbs measure is not a straightforward task. The determinant is of a very large matrix, which is a square matrix with dimension

$$N = M \text{ Lattice Sites} \times 4 \text{ Spin Indices} \times 3 \text{ Colour Indices}. \tag{3.40}$$

Typical decomposition methods for calculating matrix determinants run in $\mathcal{O}(n^3)$ time, which is problematic for a standard lattice of 10^6–10^8 sites. We can instead use a Monte-Carlo-based approximation for the determinant by introducing bosonic "pseudo-fermion" fields [103, 104]. We can define the determinant in terms of these

pseudo-fermions by first considering

$$\det A = \pi^{-N} \int \mathcal{D}[\phi_R]\mathcal{D}[\phi_I] e^{-\phi^\dagger A^{-1}\phi}, \tag{3.41}$$

where ϕ_R and ϕ_I are the respective real and imaginary parts of the pseudo-fermion field ϕ, and A is a matrix with eigenvalues λ that all have a positive real part $\mathfrak{Re}(\lambda) > 0$. We identify $A \equiv D_f D_f^\dagger$, and thus use this to determine the matrix determinant. The pseudo-fermions are noisy estimators; we can compute the integral by drawing the fields from a distribution and performing a Monte-Carlo integration.

3.3.4 Gauge Generation with Dynamical Fermions

If we consider again the Gibbs measure given in 3.31, we notice that it is highly local in the quenched approximation—we can adjust very few gauge links independently to construct a new Wilson loop. By contrast, adding the $S^{\text{eff.}}$ factor for dynamical fermions causes it to become non-local *via* the introduction of the Dirac operator, and so every gauge variable in the Wilson loop must enter the calculation of the update step. Without some specialised technique, this can lead to very large changes in the Wilson loop in a single update step, and hence a low acceptance rate, greatly diminishing the efficiency of the algorithm since we will spend most of the execution time computing update candidates that immediately get thrown away.

One common technique to address this problem, and the one used to generate the gauge configurations used in this work, is the Hybrid Monte Carlo (HMC) [105] algorithm (alternatively known as "Hamiltonian Monte Carlo" for its associations with Hamiltonian mechanics). The HMC is one instance of a class of solvers based on Molecular Dynamics techniques. Given our gauge configuration—a field of positions in configuration space—we can follow a Hamiltonian-mechanical approach by defining a "conjugate" field of momenta through configuration space, drawn from a Gaussian distribution. Labelling the field positions as Q and the conjugate momenta as P, this corresponds to a Hamiltonian

$$H[Q,P] = \frac{1}{2}P^2 + S[Q], \tag{3.42}$$

where S is the action. This Hamiltonian has the classical equations of motion, in Monte Carlo time τ,

$$\dot{P} = -\frac{\partial H}{\partial Q} = \frac{\partial S}{\partial Q}, \tag{3.43}$$

$$\dot{Q} = \frac{\partial H}{\partial P} = P, \tag{3.44}$$

which are the equations of a system of particles classically evolving in time. We can solve these equations numerically by evolving the system for a number of time steps $\epsilon = \Delta\tau$, where the total number of steps is determined such that $n\epsilon \approx 1$. This evolution is called a "trajectory", and it is deterministic. Since we have a finite step size, numerical errors are inevitable, which pull the HMC away from the correct trajectory. The HMC treats this by introducing a corrective Metropolis accept-reject step,

$$T(Q', P'|Q, P) = \min\left(1, \frac{\exp(-H[Q', P'])}{\exp(-H[Q, P])}\right), \tag{3.45}$$

which would equal 1 for an exact solution, and is closer to 1 (and hence makes the algorithm more efficient) for evolution strategies with smaller error terms.

So far, we have not seen how this algorithm is beneficial when we want to include the fermion determinant in the action. We begin by writing the action with the fermionic part in terms of the pseudo-fermion fields introduced in section 3.3.3,

$$S[U] = S_G[U] - \phi^\dagger \left(DD^\dagger\right)^{-1} \phi, \tag{3.46}$$

where we now must update the pseudo-fermion fields in addition to the gauge links. Similarly to the momentum generation for the gauge links, we can generate Gaussian-distributed complex vectors χ, and then and convert these to pseudo-fermions with $\phi = D\chi$. We need then only treat the ϕ as external fields that affect the trajectory of U, remembering to also update the ϕ vectors at each iterative step. Forcing Q to obey the SU(3)-symmetry of U allows us to formulate the HMC dynamics equations in terms of U and ϕ, and thus generate new gauge configurations.

3.3.5 Gauge Ensembles

We have now split the problem of computing the path integral into two broad parts — generating gauge configurations, and computing a path integral of some observable over those configurations. Since the configurations can be used to compute the path integral of many different observables, it makes sense to generate a set of configurations for re-use, in order to factorise out this cost of the simulation. Such a set of configurations is called a *gauge ensemble*. These configurations are computed for a particular lattice (and sea-quark action, if dynamical) and can then be used as integration variables for fermionic observables.

Despite building up this set of machinery for computing the path integrals, we have yet to define the gauge and fermion actions that enter the path integral. This proves to be a deep and detailed topic, and we will briefly outline the first formulation of these objects by Wilson in section 3.5, before moving onto more advanced and modern techniques.

3.4 Inverting the Dirac Operator

3.4.1 Quark Sources

3.4.1.1 Point Sources

The quark propagator—the inverse of the Dirac operator, D_f—is a large matrix connecting every (source site, spin, colour) combination to a (sink site, spin, colour) combination. For this discussion, following [95], we refer to a (site, spin, colour) combination as a 'point'. A propagator equal to the full inverse Dirac operator is referred to as an "all-to-all" propagator, since it connects every possible source point to every possible sink point. However, since the entries of this large matrix will be highly correlated due to translation invariance, we can be much more memory-efficient by storing only the entries that describe the propagation from a single source point to all sink points; such a restriction allows us to throw away largely redundant, memory-intensive information about the source position (since the matrix is highly correlated) whilst still maintaining all information necessary to make a choice of sink position at a later date. This is equivalent to keeping a single column of the propagator matrix [95],

$$D^{-1}(x,y_0)_{\substack{b,a_0\\b',a_0'}} = D^{-1}(x,y)_{\substack{b,a\\b',a'}}\delta(y-y_0)\delta_{a',a_0'}\delta_{a,a_0)}, \tag{3.47}$$

where the "point source" is defined by

$$S_0^{y_0,a_0,a_0'}(y)_{\substack{a\\a'}} = \delta(y-y_0)\delta_{a',a_0'}\delta_{a,a_0)}. \tag{3.48}$$

The computation of (3.47) requires the implied sum over the 3 colour indices and 4 spin indices to be evaluated, for a total of 12 source points contributing to each source-sink position pair. Since the Dirac operator is a gauge-dependent object, the Dirac operator for each gauge configuration must individually have the point source applied.

3.4.1.2 Gaussian Smeared Sources

Using point sources places the quark and anti-quark of the meson at the same lattice site, which has a small overlap with the physical wavefunction. To increase the overlap, we could use many point sources and insert functions to model the physical wavefunction, but the number of Dirac operator inversions required would be prohibitively expensive. We can instead increase this overlap and decrease the excited-state contamination of the ground state by placing the quarks at separate spatial lattice sites—but the same temporal site—by connecting them with some

"smearing function". A Jacobi smearing is a standard choice for the smearing, since it follows the Gaussian shape common to many simple wavefunctions [106]. The Jacobi smearing takes the form

$$M(x,y) = \left(1 + \frac{\sigma^2}{4N}\right) H(x,y) \tag{3.49}$$

where σ is the smearing width, N is the number of smearing steps, and $H(x,y)$ is given by

$$H(x,y) = \sum_{i=1}^{3} \left(U_i(x)\delta(x+\hat{i},y) + U_i(x-\hat{j})\delta(x-\hat{i},y) - 2\delta(x,y)\right)^N. \tag{3.50}$$

3.4.1.3 Sequential Sources

Our three-point functions require the contraction of three propagators, with the insertion of a vector current. Since we could in principle place the weak decay current anywhere in the lattice, the propagation of a quark travelling from source $\rightarrow$ current $\rightarrow$ sink should in principle require an expensive all-to-all propagator to compute.

We can escape this requirement by making use of the "sequential propagator":

$$D^{-1}_{seq.}(\vec{x},\vec{y})\gamma_5 = \sum_z D^{-1}(x,z)\Gamma D^{-1}(z,y)\gamma_5, \tag{3.51}$$

where Γ is the gamma structure required to create or annihilate the desired class of quark bilinear, which allows us to bundle two propagators into a single object by turning one propagator in a source term for the second, known as the "sequential source". Creating a sequential propagator will require an additional Dirac operator inversion, but we can now re-use this building block like any other propagator to form any correlation function in which the constituent pair of propagators may enter, and we can also treat the three-point function contraction like a two-point function contraction.

3.4.2 Inversion Algorithms

Many inversion algorithms converge in polynomial time, such as Gauss-Jordan elimination ($\mathcal{O}(n^3)$). As we already discussed for computing matrix determinants, the size of the matrices ($12N^2$, with the number of lattice sites N typically 10^6–10^8) makes such algorithms prohibitively expensive. We must instead turn to alternatives.

One class of alternatives is iterative solutions designed to solve linear systems. Many of these algorithms, such as conjugate gradient [107] instead converge as some power of the condition number κ of the matrix — for conjugate gradient, this is $\sim \sqrt{\kappa}$ for

large n. The conjugate gradient method, which we utilise in our simulations *via* the Chroma lattice QCD software package [108], will compute a point-source propagator by solving

$$Dx = S \tag{3.52}$$

for a Dirac operator D, point-source propagator vector x, and the source vector S.

It is important to note that the condition number of the Dirac matrix is dependent on the quark mass. Smaller quark masses inflate the condition number of the Dirac operator, making it more expensive to invert and more numerically unstable. For this reason, many lattice QCD studies utilise unphysically heavy up- and down-quarks, and extrapolate the masses of the resultant bound states to their physical values to generate final results. We use this strategy in our calculation; the model for the extrapolation procedure is given in section 4.2.1, and the details for the simulation are given in chapter 5. Theoretical and computational advances have however made it possible to produce viable calculations involving physical up- and down-quark masses within the last decade.

3.5 The Wilson Formulation and Beyond

3.5.1 Gauge Actions

There is no one unique way to discretise QCD — as long as our choice of action reduces to the continuum expression and is gauge invariant, we have significant freedom in how we define QCD on the lattice. To build gauge-invariant measures of the gauge fields, we can make use of the Wilson loop construction [7]—introduced in section 3.2.2—which is some closed path of gauge links. The "plaquette" is the smallest Wilson loop that can be formed, exploring four lattice sites in a square:

$$U_{\mu\nu}(x) = U_\mu(x)U_\nu(x + a\hat{\mu})U_{-\mu}(x + a\hat{\mu} + a\hat{\nu})U_{-\nu}(x + a\hat{\nu}). \tag{3.53}$$

The Wilson gauge action [7] constructs a discretised QCD gauge action from the plaquette:

$$S_G[U] = \frac{2}{g_S^2}\sum_x \sum_{\mu<\nu} \mathfrak{Re}\left[\mathrm{Tr}\left(\mathbb{1} - U_{\mu\nu}(x)\right)\right] \tag{3.54}$$

$$= \frac{a^4}{2g_S^2}\sum_x \mathrm{Tr}\left(G^{\mu\nu}(x)G_{\mu\nu}(x) + \mathcal{O}\left(a^2\right)\right) \tag{3.55}$$

where g_S is the QCD gauge coupling, and (3.55) has been obtained by Taylor-expanding the elements of the plaquette about a, using the definition of the link variable in (3.8). For a full explanation, see [95]. Since this is gauge invariant and

reduces to the continuum expression when $a \to 0$, this is a perfectly valid choice for the gauge action.

As indicated by (3.55), the Wilson gauge action reproduces the field strength tensor product up to a $\mathcal{O}\left(a^2\right)$ discretisation error. It is possible to obtain a better error scaling or more desirable simulation properties by making a different choice of gauge action. Two main methods for systematically improving errors are the Symanzik improvement program [109–111]—which we will touch upon in section 3.5.5—and renormalisation group transformations [112–114]. For this project, we utilise the Renormalisation-Improved Iwasaki gauge action [115, 116], which is formulated using the renormalisation group transform scheme and shares a general shape with the Doubly-Blocked Wilson action [117, 118]:

$$S = \frac{2}{g^2}\Big\{c_0 \sum \mathrm{Tr}(\text{simple plaquette loop}) + c_1 \sum \mathrm{Tr}(\text{rectangle loop}) \\ + c_2 \sum \mathrm{Tr}(\text{chair-type loop}) + c_3 \sum \mathrm{Tr}(\text{three-dimensional loop}) + \text{constant}\Big\}, \quad (3.56)$$

where the "simple plaquette loop" is the plaquette found in the Wilson gauge action, the "rectangle loop" is a 2×1 planar loop, the "chair-type loop" is a 2×1 non-planar loop with a 90-degree bend between the two 1×1 pieces, and the "three-dimensional loop" is a six-link path connecting two opposite vertices of a cube. The renormalisation constraint on the coefficients is $c_0 + 8c_1 + 16c_2 + 8c_3 = 1$ [116], and the Iwasaki action takes $c_0 = 3.648$, $c_1 = -0.331$, $c_2 = 0$, $c_3 = 0$. The Doubly-Blocked Wilson action is defined by $c_0 = 12.2552$, $c_1 = -1.4069$, $c_2 = 0$, $c_3 = 0$. We make use of the Iwasaki gauge action because it has an $\mathcal{O}(a^2)$-improved discretisation error, and because it allows for a small m_{res} parameter in the Domain-Wall fermion action [119] that we use for most of our fermions — see section 3.6.3 for a discussion of this action and the relevance of this parameter. As input to our simulations, we use the Iwasaki gauge ensembles calculated by the RBC-UKQCD collaboration [120–122].

3.5.2 Naïve Lattice Fermions

We can make a first attempt at discretising the fermion terms in the action by defining the fields at the lattice sites, and replacing derivatives with their discrete counterparts. Such an action is known as the *naïve fermion action*, which takes the form

$$S[\psi, \bar{\psi}] = a^4 \sum_x \bar{\psi}_\alpha(x) D_{\alpha\beta}(x) \psi_\beta(x), \quad (3.57)$$

where the Dirac operator is given by

$$D_{\alpha\beta}(x,y) = \sum_\mu (\gamma_\mu)_{\alpha\beta} \left(\frac{U_\mu(x)\delta_{x+a\hat{\mu},y} - U_{-\mu}(x)\delta_{x-a\hat{\mu},y}}{2a} + M\delta_{\alpha,\beta}\delta_{x,y} \right). \quad (3.58)$$

It may not be immediately apparent, but inverting this expression to obtain the propagator for the quark field leads to a complication in the theory. We can elucidate this by working in momentum space, so we can first Fourier transform the Dirac operator to

$$\widetilde{D}_p = m + \frac{i}{a}\sum_\mu \gamma_\mu \sin(p^\mu a), \tag{3.59}$$

which inverts to

$$\widetilde{D}^{-1}(p) = \frac{m - ia^{-1}\sum_\mu \gamma_\mu \sin(p^\mu a)}{m^2 + a^{-2}\sum_\mu \sin^2(p^\mu a)}, \tag{3.60}$$

which reduces to the expected continuum expression

$$\lim_{a\to 0} \widetilde{D}^{-1}(p) = \frac{m - i\gamma^\mu p_\mu}{m^2 + p^2}. \tag{3.61}$$

In the massless limit, we obtain a physical pole for the propagator at $p = (0,0,0,0)$. However, due to the sine, we also get a pole when any element of p is π/a. This generates a total of $2^4 = 16$ poles - two per dimension. These are called "doublers", and it is necessary to remove these spurious poles to recover the physical continuum behaviour. We will now take a look at a simple way to achieve this with the Wilson action.

3.5.3 Wilson Fermions

The Wilson action removes the unphysical doublers in the continuum limit by adding an additional term to the Dirac operator [7]:

$$\widetilde{D}_{\text{Wilson}}(p) = m + \frac{i}{a}\sum_\mu \gamma_\mu \sin(p^\mu a) + \frac{1}{a}\sum_\mu (1 - \cos(p^\mu a)). \tag{3.62}$$

This term vanishes for $p = (0,0,0,0)$ and reproduces the naïve lattice fermion result; for any momentum with at least one component of π/a, this term instead acts like an additional contribution to the mass:

$$m \to m + \frac{2l}{a}, \tag{3.63}$$

where l is the number of components equal to π/a. This mass term becomes divergent in the continuum limit, which causes the poles to decouple from the theory. The only pole that remains is the physical one, which did not obtain this additional mass term. The Wilson action does, however, come with a heavy cost: the Wilson term added to the action explicitly breaks chiral symmetry. In fact, the Nielson-Ninomiya theorem states that it is impossible to construct a local action that is both free of doublers and preserves chiral symmetry in an even number of dimensions [123].

This poses a particular problem: the spontaneous breaking of chiral symmetry is a core feature of QCD, explaining the low masses of the pseudo-Nambu-Goldstone boson octet and providing an effective field theory for the perturbative study of low-energy QCD in the form of chiral perturbation theory. Without deeper inspection, the Nielsen-Ninomiya theorem seems to place severe limitations on the applicability of lattice QCD. In section 3.5.4, we will discuss how this situation can be avoided *via* the Ginsparg-Wilson relation, and the consequences it has for the choices we make when simulating the $B_{(s)} \to P\ell\nu$ processes.

3.5.4 Chiral Symmetry on the Lattice

In the previous section, we stated that the Nielsen-Ninomiya theorem [123] tells us that no fermion action can be formulated that both preserves chiral symmetry and exists in an even number of dimensions. There is a trick that allows us to get around this theorem, however — the Ginsparg-Wilson relation [124] tells us how chiral symmetry is broken on the lattice *via* a specific value of the $\{\gamma_5, D\}$ anti-commutator:

$$\gamma^5 D + D\gamma^5 = aD\gamma^5 D, \tag{3.64}$$

which is a function of the lattice spacing a and hence matches the continuum definition for chiral symmetry in the continuum. The Wilson action does not obey this symmetry, nor do many other choices of action; we will return to the Ginsparg-Wilson relation when we discuss Domain-Wall fermions in section 3.6.3, which obey it in a strict limit.

Furthermore, with a description of how chiral symmetry is broken on the lattice, we can find one avenue to rescue chirally asymmetric fermions as shown by Lüscher [125]. Continuum fields may be expressed in a chiral basis in terms of left- and right-handed Majorana spinor components, which is not possible for lattice fields with broken chiral symmetry. However, when we match the lattice fields to the continuum fields *via* renormalisation, we can form conditions on the renormalisation such that QCD-like behaviour is recovered in the continuum by adding terms that reconstruct the chiral basis of QCD. The question of recovering continuum QCD can then be restated as a question of renormalising the lattice fields correctly; for chirally asymmetry fermions, this will typically take the form of additive renormalisation terms (see *e.g.* [126] for arguments). Lattice fields that obey the Ginsparg-Wilson relation therefore have considerably simpler renormalisation considerations, although the overlap operator (introduced in [127–130], modern formulation in [131]) is presently the only known exact solution to the Ginsparg-Wilson relation (and was shown to be a solution in [132]).

3.5.5 Symanzik Improvement Program

The Symaznik improvement program is a prodecure for systematically reducing discretisation errors on lattice fields by cancelling off error terms. To compare this to a simple example—in the spirit of Gattringer and Lang [95]—consider approximating the derivative of some function $f(x)$ *via* the central difference

$$\frac{f(x+a)-f(x-a)}{2a} = f'(x) + \frac{a^2}{6}f'''(x) + \frac{a^4}{120}f'''''(x) + ... \tag{3.65}$$

where the right-hand-side has been obtained by Taylor-expanding the function about $\pm a$,

$$f(x \pm a) = f(x) \pm af'(x) + \frac{a^2}{2}f''(x) \pm \frac{a^3}{6}f'''(x) + ... \tag{3.66}$$

The central difference has a leading $\mathcal{O}\left(a^2\right)$ discretisation error on the derivative, as seen in (3.65). By finding expressions for the error terms on the right-hand-side of (3.65), we can obtain an expression for the central difference to an arbitrary degree of precision $\mathcal{O}\left(a^{2n}\right)$ by adding increasingly complex cancellation terms to the left-hand side. For example, one of the ways we can express the third derivative is

$$f'''(x) = \frac{f(x+2a) - 2f(x+a) + 2f(x-a) - f(x-2a)}{2a^3} + \mathcal{O}(a^2), \tag{3.67}$$

and by adding this with a factor of $-a^2/6$ to (3.65), we can improve the overall discretisation error on $f'(x)$ to $\mathcal{O}\left(a^4\right)$ by cancelling off the $f'''(x)$ term. To improve the error to $\mathcal{O}\left(a^6\right)$, we would have to cancel off the $\mathcal{O}\left(a^4\right)$ terms introduced by both the central difference and $(a^2/6)f'''(x)$ approximations.

The Symanzik improvement program [109–111] follows the same spirit as this simple example: expressing lattice fields as a series expansion of continuum quantities, and using this to systematically improve discretisation errors on actions using these fields. Lattice field calculations are considerably more involved than the example presented so far, and the language used to compute the necessary cancellation terms is Symanzik effective theory. Although we will not dive into the details of Symanzik improvement, this sketch will serve as a useful reference for when we introduce the Sheikholeslami-Wohlert (Clover) action in section 3.6.1, as a stepping stone to the Relativistic Heavy Quark (RHQ) action we use to simulate b quarks in this work.

3.5.6 γ_5-hermiticity

Many lattice Dirac operators possess γ_5-hermiticity: a symmetry that states

$$(\gamma_5 D_\mu(x))^\dagger = \gamma_5 D \Rightarrow D_\mu(x)^\dagger = \gamma_5 D_\mu(x)\gamma_5. \tag{3.68}$$

Aside from being a useful trick to simplify expressions, this also implies that the fermion determinant is real. The realness of the fermion determinant allows us to fold it into the weighting factor of the Boltzmann distribution integrand and further simplify the integration procedure.

Moreover, γ_5-hermiticity is not restricted to the Dirac operator itself; the inverse also inherits this property, extending its usefulness to the manipulation of Wick-contracted fermion fields.

3.6 Fermion Actions

3.6.1 Clover Action

The Wilson action carries an $\mathcal{O}(a)$ discretisation error, which would make it the leading source of error in a typical calculation. We outlined the Symanzik improvement program in section 3.5.5, and are now in a position to ask a question: what happens when we apply Symanzik improvement to the Wilson action?

Sheikholeslami and Wohlert made such a calculation in their 1985 paper [133], in which they found $\mathcal{O}(a)$-improvement can be obtained by adding a single term to the Wilson action,

$$c_{\text{sw}} a^4 \sum_{x \in \Lambda} \bar{\psi}(x) \sum_{\mu < \nu} \frac{i}{4} \sigma_{\mu\nu} \widehat{G}_{\mu\nu} \psi(x), \tag{3.69}$$

where $\sigma_{\mu\nu}$ is the dimension-five operator

$$\sigma_{\mu\nu} = \frac{[\gamma_\mu, \gamma_\nu]}{2i}, \tag{3.70}$$

and $\widehat{G}_{\mu\nu}$ is the discretised field strength tensor, which can be expressed in terms of a sum of plaquettes originating at the lattice site at x,

$$\widehat{G}_{\mu\nu} = \frac{i}{8a^2} \left(Q_{\mu\nu}(x) - Q_{\nu\mu}(x) \right), \tag{3.71}$$

with $Q_{\mu\nu}$(x) the sum of plaquettes

$$Q_{\mu\nu}(x) = U_{\mu,\nu}(x) + U_{-\nu,\mu}(x) + U_{-\mu,-\nu}(x) + U_{\nu,-\mu}(x) \tag{3.72}$$

and c_{sw} is a coefficient that can be non-perturbatively turned to obtain an $\mathcal{O}(a)$-improved discretisation error on the fermions. A first attempt at applying Symanzik improvement suggests that five terms are necessary, but this can be reduced to (3.69) by considering symmetry arguments and parameter redefinitions [133].

This action is commonly known as the clover action, since in a 2D slice of the lattice the four contributing plaquettes to $Q_{\mu\nu}$ are reminiscent of a clover with four square leaves. For reasons that we will now discuss, we use an anisotropic version of the Clover action to simulate the b quark.

3.6.2 RHQ Action

Putting a b quark on a lattice is not as straightforward as it is for lighter quarks. Lattices in common use today typically have inverse lattice spacings of $\sim \mathcal{O}(2-4\text{GeV})$, and the calculations presented in this thesis are no exception. The b quark, however, has an $\overline{\text{MS}}$-scheme mass of $4.18^{+0.03}_{-0.02}$ GeV [4]. In order to properly resolve a field, we require

$$m_q \ll \frac{1}{a} \Rightarrow m_q a \ll 1, \tag{3.73}$$

since a acts as an ultraviolet cut-off. Discretisation errors related to the mass and momentum enter as $\mathcal{O}((m_b a)^n)$, $\mathcal{O}((pa^n))$, and $\mathcal{O}((pa)(m_b a)^n)$ [11], where n of arbitrary order; therefore, placing a b quark with a physical mass on a typical lattice will have very large or completely uncontrolled errors.

There are multiple ways to address this. One option is to use non-physical b quark masses and extrapolate to a physical mass, which typically still requires use of an effective action for reasonable masses to be taken, such as Highly Improved Staggered Quarks [8]. Domain-wall fermion simulations are also becoming a potential approach, with charm-like masses now feasible.

The approach taken by the Relativistic Heavy Quark (RHQ) action is to instead note that, near rest, the heavy quark will have a mass much larger than its spatial momentum. This allows us to expand the spatial components of the derivative D_i in powers of $(a\vec{p})$ *via* the Symanzik improvement programme (*c.f.* section 3.5.5), with the aim of cancelling all divergent error terms, although we cannot do this for the temporal direction and must maintain to all powers terms of the form $(m_0 a)$ and D_0 [9, 11]. This results in the Lagrangian of the effective action taking the form

$$\mathcal{L}_{\text{eff.}} = \mathcal{L}_{\text{eff.},-1} + \mathcal{L}_{\text{eff.},0} + \mathcal{L}_{\text{eff.},1} + ... \tag{3.74}$$

where we need only expand up to $\mathcal{L}_{\text{eff.},1}$ for $\mathcal{O}(a)$ improvement, and the three terms are given by

$$\mathcal{L}_{\text{eff.},-1} = \overline{\psi}\left(\frac{1}{2}B^{-1,1} + \gamma^0 D^0 C^{-1,1}\right)\psi, \tag{3.75}$$

$$\mathcal{L}_{\text{eff.},0} = \overline{\psi}\left(\left\{\vec{\gamma}\vec{D}, B^{0,1}\right\} + a\left\{\left[\vec{\gamma}\vec{D}, \gamma^0 D^0\right], C^{0,1}\right\}\right)\psi, \tag{3.76}$$

$$\begin{aligned}\mathcal{L}_{\text{eff.},1} = a\overline{\psi}\Big(&\vec{D}^2 B^{1,1} + a\left\{\vec{D}^2, \gamma^0 D0\right\} C^{1,1} \\ &+ \left[\gamma^i\gamma^j\right][D^i, D^j]B^{1,2} + a\left\{\left\{\gamma^i, \gamma^j\right\}\left[D^i, D^j\right], \gamma^0 D^0\right\} C^{1,2} \\ &+ \left[\gamma^i\gamma^0\right][D^i, D^0]B^{1,3} + a\left\{\left\{\gamma^i, \gamma^0\right\}\left[D^i, D^0\right], \gamma^0 D^0\right\} C^{1,3}\Big)\psi\end{aligned} \tag{3.77}$$

where $B^{n,m}$ and $C^{n,m}$ are polynomials in $m_0 a$ and D_0, and both m_0 and D_0 are taken to be $\mathcal{O}(a)$ to account for the situation where $m_0 \sim a$. One can then find redundancies in this expression and rotate the quark fields to show that, to $\mathcal{O}(a)$, the the $(m_0 a)$ and D_0 terms captured by the B and C polynomials can be entirely summarised by three parameters—$m_0 a$, c_{sw}, and ζ—which also cancel $\mathcal{O}(ap)$ discretisation errors [11]. Therefore, by inserting the correct values for these three parameters, the divergent error terms can be cancelled to all orders. It turns out that the $m_0 a$ parameter must be set to the physical mass for the quark it represents, whereas c_{sw} and ζ parameters have much more complicated definitions [11]. In a companion paper, the authors of the Columbia formulation also describe a tuning methodology to determine the correct values of the RHQ parameters [134]. The tuning procedure incurs an error on the three input parameters $m_0 a$, c_{sw}, ζ which must be taken into account in the final systematic error. A discussion of the RHQ tuning procedure is presented in section 5.3.3.

The RHQ action is based on the Fermilab action [9], and has been restated as both a Tsukuba formulation [10] and a Columbia formulation [11], each with different parameterisations of the input variables. In this work, we make use of the Columbia formulation of the RHQ action, which is

$$a^4 \sum_{x,y} \bar{\psi}(x)\left[\gamma_0 D_0 + \zeta\gamma_i \cdot D_i - \frac{a}{2}(D_0)^2 - \frac{a}{2}(D_i)^2 + c_{\text{sw}}\sum_{\mu>\nu}\frac{ia}{4}\sigma_{\mu\nu}\hat{F}_{\mu\nu}\right]\psi(y) \tag{3.78}$$

with the covariant derivatives

$$D_\mu\psi(x) = \frac{1}{2a}\left[U_\mu(x)\psi(x + a\hat{\mu}) - U_{-\mu}(x)\psi(x - a\hat{\mu})\right], \tag{3.79}$$

$$D_\mu^2\psi(x) = \frac{1}{a^2}\left[U_\mu(x)\psi(x + a\hat{\mu}) - U_{-\mu}(x)\psi(x - a\hat{\mu}) - \psi_(x))\right]. \tag{3.80}$$

RHQ fermions, despite breaking chiral symmetry, can be multiplicatively renormalised for on-shell Green's functions [11]. We will discuss the determination of the relevant renormalisation factors and relation to the heavy-light current bilinear in section 3.8.

3.6.3 Domain-Wall Fermion Action

The Domain-Wall Fermion (DWF) action [12–16] adds an unphysical discretised fifth dimension, which when taken to infinity satisfies the Ginsparg-Wilson relation and reproduces the overlap operator [131]. Since the infinite dimension cannot be simulated on a computer, we must make an approximation that approximately satisfies the Ginsparg-Wilson relation by instead introducing a dimension of length L_s. It is also necessary to introduce a new mass parameter M_5 that varies in this fifth dimension, which plays the role of removing doublers from the action. We use the Shamir variant of domain-wall fermions, with an action

$$S_{\mathrm{DWF}} = \sum_{x,y}\sum_{s,r} \overline{\Psi}(x,s) D_{\mathrm{DWF}}(x,s|y,r) \Psi(y,r), \tag{3.81}$$

where x and y are co-ordinates on the 4D boundary of the 5D bulk, and s and r are co-ordinates in the 5th dimension. The Dirac operator $D_{\mathrm{DWF}}(x,s|y,r)$ can be separated into a Wilson term and bulk term,

$$D_{\mathrm{DWF}}(x,s|y,r) = \delta_{s,r} D_{\mathrm{DWFWilson}}(x,y) + \delta_{x,y} D^{(5)}_{\mathrm{DWF}}(s,r), \tag{3.82}$$

where $D_{\mathrm{DWFWilson}}(x,y)$ is the Wilson Dirac operator stated in (3.58) with the mass replaced with M_5, and the the 5th dimension term

$$\begin{aligned} D^{(5)}_{\mathrm{DWF}}(s,r) = \delta_{s,r} - (1-\delta_{s,L_s-1})P^- \delta_{s+1,r} - (1-\delta_{s,0})P^+ \delta_{s-1,r} \\ + m(P^- \delta_{s,L_s-1}\delta_{0,r} + P^+ \delta_{s,0}\delta_{L_s-1,r}), \end{aligned} \tag{3.83}$$

where $P^{\pm} = (1 \pm \gamma^5)/2$, the right- and left-handed chiral projectors. The mass m of the fermion enters this term, rather than the Wilson action term.

The physical 4D fields can be extracted by making the projections

$$\psi(x) = P^- \Psi(x,0) + P^+ \Psi(x, L_s - 1), \tag{3.84}$$

$$\overline{\psi}(x) = \overline{\Psi}(x, L_s - 1) P^- + \overline{\Psi}(x,0) P^+. \tag{3.85}$$

From this definition, we can see that the left- and right-handed fields decouple as $L_s \to \infty$ and chiral symmetry is preserved. Since we will always have a finite L_s in a numerical simulation, there will be some residual chiral symmetry breaking that contributes to the quark mass. For Domain-Wall Fermions, this takes the form of a simple linear combination

$$m_q = m + m_{\mathrm{res}} \tag{3.86}$$

where m_{res} is the additional mass due to residual chiral symmetry breaking. Since the residual mass is typically small, we can approximate Domain-Wall fermions as satisfying the Ginsparg-Wilson relation, which greatly simplifies their

renormalisation. As with the RHQ renormalisation factor, we will discuss the DWF renormalisation in section 3.8.

For this work, we use Shamir Domain-Wall Fermions for all quark fields other than the bottom quark.

3.6.4 RHQ-DWF Bilinear

The vector current $V_\mu^l = \bar{x}\gamma^\mu b$ carries a discretisation error of $\mathcal{O}(a)$. We can construct a current with an $\mathcal{O}(a)$-improved error by adding single-derivative operators to the current, following the previous RBC-UKQCD $B_s \to K\ell\nu$, $B \to \pi\ell\nu$ paper [90]:

$$V_\mu^1 = \bar{l}(x) 2 \overrightarrow{D}_\mu b(x), \tag{3.87}$$
$$V_\mu^2 = \bar{l}(x) 2 \overleftarrow{D}_\mu b(x), \tag{3.88}$$
$$V_\mu^3 = \bar{l}(x) 2\gamma_\mu(\gamma_i \cdot \overrightarrow{D}_i) b(x), \tag{3.89}$$
$$V_\mu^4 = \bar{l}(x) 2\gamma_\mu(\gamma_i \cdot \overleftarrow{D}_i) b(x), \tag{3.90}$$

where the covariant derivatives are

$$\overrightarrow{D}_\mu b(x) = \frac{U_\mu(x) b(x + a\hat{\mu}) - U_{-\mu}(x) b(x - a\hat{\mu})}{2}, \tag{3.91}$$
$$\bar{l}(x) \overleftarrow{D}_\mu = \frac{\bar{l}(x + a\hat{\mu}) U_\mu^\dagger(x) - \bar{l}(x - a\hat{\mu}) U_{-\mu}^\dagger(x)}{2}. \tag{3.92}$$

Denoting the unimproved vector current as V_μ^0, these terms can then be added to the temporal and spatial parts of the vector current with a set of matching coefficients:

$$V_0(x) = V_0^0(x) + c_t^3 V_0^3(x) + c_t^4 V_0^4(x), \tag{3.93}$$
$$V_i(x) = V_i^0(x) + c_i^1 V_i^1(x) + c_i^2 V_i^2(x) + c_i^3 V_i^3(x) + c_i^4 V_i^4(x). \tag{3.94}$$

These coefficients have been calculated to one-loop order [135] using mean-field improved lattice perturbation theory [136], and we report these values when we introduce the details of our lattice simulation in chapter 5. As with the two actions we use, we will also discuss the current renormalisation in section 3.8.

3.7 Correlation Functions

3.7.1 Lattice Construction

As we discussed in 3.2.4, we can build correlation functions out of combinations of quark bilinears of flavours f_1 and f_2, which are the annihilation and creation operators

given respectively by:

$$\mathcal{O}_P = \overline{\psi}^{(f_1)}(x)\Gamma\psi^{(f_2)}(x); \quad \mathcal{O}_P^\dagger = \pm\overline{\psi}^{(f_2)}(x)\Gamma^\dagger\psi^{(f_1)}(x), \tag{3.95}$$

where Γ is the appropriate gamma structure for the bilinear, and the sign on the creation operator is dependent on the particular gamma structure. For pseudoscalars, the gamma structures are γ_5 matrices:

$$\mathcal{O}_P = \overline{\psi}^{(f_1)}(x)\gamma_5\psi^{(f_2)}(y); \quad \mathcal{O}_P^\dagger = -\overline{\psi}^{(f_2)}(y)\gamma_5\psi^{(f_1)}(x), \tag{3.96}$$

where we have used the fact that $(\gamma_5)^\dagger = \gamma_5$. The residual minus sign comes from the re-ordering of the γ_5 and γ_0 matrices after taking the Hermitian conjugate to find an expression in terms of $\overline{\psi}$ and ψ rather than $\psi^\dagger$ and ψ.

We will also simplify our notation of writing inverse Dirac matrices in the Wick contraction by directly assigning a symbol for the propagator:

$$G_f(x,y)_{\mathrm{ab}} = \psi(x)_{\mathrm{a}}^{(f)}\bar{\psi}(y)_{\mathrm{b}}^{(f)}, \tag{3.97}$$

which describes a particle propagating from y to x, where colour indices are suppressed and spin indices are indicated with roman letters.

One further property of great utility is γ_5-hermiticity, which we covered in 3.5.6. We we noted there, many propagators are γ_5-hermitian, and this is a property of both RHQ and DWF propagators. This property is defined by the relation

$$G_f(x,y)^\dagger_{ab} = (\gamma_5)_{\mathrm{ac}}G_f(y,x)_{\mathrm{cd}}(\gamma_5)_{\mathrm{db}}. \tag{3.98}$$

This allows us to re-use lattice propagators computed for the direction $y \to x$ if we need the same propagator for the direction $x \to y$. As a simple example, the computational cost of generating the quark propagators—generally the dominant expense—for a meson composed of a quark and anti-quark of the same flavour can be halved by re-using the quark propagator as the anti-quark propagator with this relation.

3.7.2 Two-Point Functions

We can begin with a discussion of the analytical form of the two-point function, which we can use to extract energies from the correlators. As we noted in section 2.7.2, this is required in order to extract the form factors from the three-point functions.

Pseudoscalar two-point functions are the product of a creation and annihilation operator for a pseudoscalar P,

$$C_{\text{2pt}}(t) = \langle \mathcal{O}_P(\vec{x}, t)\mathcal{O}_P^\dagger(\vec{0}, 0)\rangle, \tag{3.99}$$

which we can find an analytical expression for by making the individual expectation values explicit, and pulling out the time-dependence of the operators,

$$C_{\text{2pt}}(t) = \frac{1}{Z}\sum_{n,m}\frac{1}{4E_nE_m}\langle m|e^{-\hat{H}(T-t)}\mathcal{O}_P(\vec{x},0)e^{-\hat{H}t}|n\rangle\langle n|\mathcal{O}_P^\dagger(\vec{0},0)|m\rangle, \tag{3.100}$$

$$= \frac{1}{Z}\sum_{n,m}\frac{1}{4E_nE_m}\langle m|e^{-E_m(T-t)}\mathcal{O}_P(\vec{x},0)e^{E_nt}|n\rangle\langle n|\mathcal{O}_P^\dagger(\vec{0},0)|m\rangle, \tag{3.101}$$

where the Es are energies of the nth state, and T is the lattice time extent. The explicit form for the partition function is

$$Z = \sum_n \frac{\langle n|e^{-TH}|n\rangle}{2E_n} = \sum_n \frac{e^{-TE_n}}{2E_n}, \tag{3.102}$$

which gives us the total expression

$$C_{\text{2pt}}(t) = \frac{\sum_{n,m}\frac{1}{4E_nE_m}\langle m|e^{-E_m(T-t)}\mathcal{O}_P(\vec{x},0)e^{-E_nt}|n\rangle\langle n|\mathcal{O}_P^\dagger(\vec{0},0)|m\rangle}{\sum_l \frac{1}{2E_l}e^{-TE_l}}. \tag{3.103}$$

These operators must act on the ground states to create and annihilate the meson, so throwing away any states where both $n, m \neq 0$ leaves us with

$$C_{\text{2pt}}(t) = \sum_{n,m}\left(\frac{e^{-E_nt}e^{-(T-t)E_0}}{4E_nE_0}\frac{1}{\sum_l \frac{1}{2E_l}e^{-TE_l}}\langle 0|\mathcal{O}_P(\vec{x},0)|n\rangle\langle n|\mathcal{O}_P^\dagger(\vec{0},0)|0\rangle + \right.$$
$$\left.\frac{e^{-E_m(T-t)}e^{-E_0t}}{4E_0E_m}\frac{1}{\sum_l \frac{1}{2E_l}e^{-TE_l}}\langle m|\mathcal{O}_P(\vec{x},0)|0\rangle\langle 0|\mathcal{O}_P^\dagger(\vec{0},0)|m\rangle\right), \tag{3.104}$$

which is a sum of forwards-propagating and backwards-propagating states, normalised by a sum of finite-size effects. Since the n and m sums are now independent, we can write them using a single n index. We can also cancel off a factor of $(1/2E_0)e^{-TE_0}$ in the expression:

$$C_{\text{2pt}}(t) = \sum_n\left(\frac{e^{-\Delta E_nt}}{2E_n}\frac{1}{1+\frac{E_0}{E_1}e^{-T\Delta E_1}+\frac{E_0}{E_2}e^{-T\Delta E_2}+\ldots}\langle 0|\mathcal{O}_P(\vec{x},0)|n\rangle\langle n|\mathcal{O}_P^\dagger(\vec{0},0)|0\rangle + \right.$$
$$\left.\frac{e^{-\Delta E_n(T-t)}}{2E_n}\frac{1}{1+\frac{E_0}{E_1}e^{-T\Delta E_1}+\frac{E_0}{E_2}e^{-T\Delta E_2}+\ldots}\langle n|\mathcal{O}_P(\vec{x},0)|0\rangle\langle 0|\mathcal{O}_P^\dagger(\vec{0},0)|n\rangle\right), \tag{3.105}$$

If we can approximate the finite-size effects as negligible, we can say that

$$1 + \frac{E_0}{E_1} e^{-T\Delta E_1} + \frac{E_0}{E_2} e^{-T\Delta E_2} + ... \approx 1 \tag{3.106}$$

and write

$$C_{\text{2pt}}(t) = \sum_n \left(\frac{e^{-\Delta E_n t}}{2E_n} \langle 0|\mathcal{O}_P(\vec{x},0)|n\rangle\langle n|\mathcal{O}_P^\dagger(\vec{0},0)|0\rangle + \frac{e^{-\Delta E_n (T-t)}}{2E_n} \langle n|\mathcal{O}_P(\vec{x},0)|0\rangle\langle 0|\mathcal{O}_P^\dagger(\vec{0},0)|n\rangle \right), \tag{3.107}$$

Since the quantities ΔE_n—which are the difference between the vacuum and state energy—are what is actually measured, we will drop the delta from this expression as just write E_n. Pulling out the momentum-dependence of the operations using the Fourier transform and absorbing this into the energy definition, we can than identify the matrix elements in this sum as the same values, and simplify the expression as

$$= \sum_n \frac{Z_a Z_b}{2E_n} \left(e^{-E_n t} + e^{-E_n (T-t)} \right) \tag{3.108}$$

where matrix element for the transition between the vacuum and energy state $|n\rangle$ for the pseudoscalar P is

$$Z_a = |\langle 0|\mathcal{O}_P|n\rangle| = |\langle n|\mathcal{O}_P^\dagger|0\rangle|. \tag{3.109}$$

For the case where the annihilation and creation operators share the same type of source, we can state $Z_a = Z_b$. We can see that the value of the correlation function is exponential in the energy over time, and so for $0 \ll t \ll T$ the ground state will dominate, assuming a sufficiently large T. Such an expression behaves like a cosh function defined between the times $t = 0$ and $t = T$.

Under an appropriate ratio, and assuming ground-state dominance, we can also immediately isolate the ground-state energy. Since such a ratio will be contaminated by excited-states for $t \sim 0$, $t \sim T$, we call this the "effective mass". The ratio

$$m_{\text{eff}}(t + 1/2) = \ln\left(\frac{C(t)}{C(t+1)} \right) \tag{3.110}$$

gives the effective mass for the region $0 \ll t \ll T/2$, where the forwards-propagating state dominates. If we also wish to include the influence of the backwards-propagating state, we can instead define the effective mass as

$$m_{\text{eff}}(t) = \cosh^{-1}\left(\frac{C(t+1) + C(t-1)}{2C(t)} \right), \tag{3.111}$$

since, as we noticed above, the ground-state correlator behaves like a cosh function.

To compute the two-point functions under lattice QCD, we must calculate the contributions to $\langle \mathcal{O}_P(\vec{x},t)\mathcal{O}_P^\dagger(\vec{0},0)\rangle$. We can do this by making all possible Wick contractions between the quark fields composing the $\mathcal{O}_P$ operators.

We will label the flavours of the two quarks in the meson as f_1 and f_2. For mesons with $f_1 \neq f_2$, we generate only a connected two-point correlation function, given by

$$\langle \mathcal{O}_P(m)\mathcal{O}_P^\dagger(n)\rangle_{\text{conn.}} = -\Big\langle (\overbrace{\bar\psi(m)})_a^{(f_1)}(\gamma_5)_{ab}(\overbrace{\psi(m)})_b^{(f_2)}(\bar\psi(n))_c^{(f_2)}(\gamma_5)_{cd}(\overbrace{\psi(n)})_d^{(f_1)}\Big\rangle \tag{3.112}$$

$$= \Big\langle (\overbrace{\psi(n)})_d^{(f_1)}(\bar\psi(m))_a^{(f_1)}(\gamma_5)_{ab}(\overbrace{\psi(m)})_b^{(f_2)}(\bar\psi(n))_c^{(f_2)}(\gamma_5)_{cd}\Big\rangle \tag{3.113}$$

$$= \Big\langle \text{Tr}\left[(G_{f_1}(n,m))_{da}(\gamma_5)_{ab}(G_{f_2}(m,n))_{bc}(\gamma_5)_{cd}\right]\Big\rangle \tag{3.114}$$

$$= \Big\langle \text{Tr}\left[(G_{f_1}(n,m))_{da}(G_{f_2}(n,m))^\dagger_{ad}\right]\Big\rangle \tag{3.115}$$

where we have flipped the sign in (3.113) due to the anti-commutation of the Grassmann-valued quark fields and used γ_5-hermiticity in (3.115). In the above expressions, the spin indices are made explicit and the colour indices are suppressed.

For $f_1 = f_2$, there is also a disconnected contribution:

$$\langle \mathcal{O}_P(m)\mathcal{O}_P^\dagger(n)\rangle_{\text{disc.}} = -\Big\langle (\overbrace{\bar\psi(m)})_a^{(f_1)}(\gamma_5)_{ab}(\overbrace{\psi(m)})_b^{(f_1)}(\overbrace{\bar\psi(n)})_c^{(f_1)}(\gamma_5)_{cd}(\overbrace{\psi(n)})_d^{(f_1)}\Big\rangle \tag{3.116}$$

$$= -\Big\langle (\overbrace{\psi(m)})_b^{(f_1)}(\bar\psi(m))_a^{(f_1)}(\gamma_5)_{ab}(\overbrace{\psi(n)})_d^{(f_1)}(\bar\psi(n))_c^{(f_1)}(\gamma_5)_{cd}\Big\rangle \tag{3.117}$$

$$= -\Big\langle \text{Tr}\left[(G_{f_1}(m,m))_{ba}(\gamma_5)_{ab}\right]\text{Tr}\left[(G_{f_1}(n,n))_{dc}(\gamma_5)_{cd}\right]\Big\rangle. \tag{3.118}$$

3.7.3 Three-point Functions

The three-point functions that we study are flavour-changing charged currents. For this section, we will call the quark which does not change flavour the "spectator" quark and label it with $(sp.)$. We will call the quark which does change flavour the "valence" quark, and label the two flavours of this quark f_i and f_f for "initial flavour" and "final flavour". We therefore have the initial and final state annihilation operators

$$\mathcal{O}_i(x) = \bar\psi^{(f_i)}(x)\gamma_5\psi^{(s)}(x), \tag{3.119}$$

$$\mathcal{O}_f(x) = \bar\psi^{(f_f)}(x)\gamma_5\psi^{(s)}(x). \tag{3.120}$$

To implement the change in flavour, we utilise the flavour-changing vector current

$$V^\mu(x) = \bar\psi^{(f_i)}(x)\gamma^\mu\psi^{(f_f)}(x). \tag{3.121}$$

The three-point function itself is given by

$$C^{\text{3pt}}(t, t_{\text{snk}}, \vec{p}) = \sum_x e^{-i\vec{p}_x \cdot \vec{x}} \langle \mathcal{O}_f(\vec{x}, t) V^\mu(\vec{y}, t_{\text{snk}}) \mathcal{O}_i^\dagger(\vec{0}, 0) \rangle, \tag{3.122}$$

$$= \sum_{n,m} \frac{e^{-E_m^i t} e^{-E_n^f (t_{snk} - t)}}{4 E_m^i E_n^f} \langle 0 | \mathcal{O}_f | n \rangle \langle n | V^\mu | m \rangle \langle m | \mathcal{O}_i^\dagger | 0 \rangle, \tag{3.123}$$

where t_{snk} is the time at which the final state is annihilated.

The flavours f_i and f_f must necessarily be different for a change of flavour to occur, so we need only consider whether these fields can contract with the spectator quark to determine the diagrams that contribute to the final amplitude.

For $f_i \neq sp.$, $f_f \neq sp.$, we again obtain only a connected diagram:

$$\langle \mathcal{O}_f V^\mu \mathcal{O}_i^\dagger \rangle_{\text{conn.}} = - \left\langle (\bar{\psi}(z))_a^{(f_f)} (\gamma_5)_{ab} (\psi(z))_b^{(sp.)} (\bar{\psi}(y))_c^{(f_i)} (\gamma^\mu)_{cd} (\psi(y))_d^{(f_f)} (\bar{\psi}(x))_e^{(sp.)} (\gamma_5)_{ef} (\psi(x))_f^{(f_i)} \right\rangle \tag{3.124}$$

$$= \left\langle (\psi(y))_d^{(f_f)} (\bar{\psi}(z))_a^{(f_f)} (\gamma_5)_{ab} (\psi(z))_b^{(sp.)} (\bar{\psi}(x))_e^{(sp.)} (\gamma_5)_{ef} (\psi(x))_f^{(f_i)} (\bar{\psi}(y))_c^{(f_i)} (\gamma^\mu)_{cd} \right\rangle \tag{3.125}$$

$$= \left\langle \text{Tr} \left[\left(G_{(f_f)}(y, z) \right)_{da} (\gamma_5)_{ab} \left(G_{(s)}(z, x) \right)_{be} (\gamma_5)_{ef} \left(G_{(f_i)}(x, y) \right)_{fc} (\gamma^\mu)_{cd} \right] \right\rangle \tag{3.126}$$

For $f_f = sp.$, there is an additional disconnected diagram:

$$\langle \mathcal{O}_f V^\mu \mathcal{O}_i^\dagger \rangle_{\text{disc. } f_f} = - \left\langle (\bar{\psi}(z))_a^{(f_f)} (\gamma_5)_{ab} (\psi(z))_b^{(f_f)} (\bar{\psi}(y))_c^{(f_i)} \gamma_{cd}^\mu (\psi(y))_d^{(f_f)} (\bar{\psi}(x))_e^{(f_f)} (\gamma_5)_{ef} (\psi(x))_f^{(f_i)} \right\rangle \tag{3.127}$$

$$= - \left\langle (\psi(z))_b^{(f_f)} (\bar{\psi}(z))_a^{(f_f)} (\gamma_5)_{ab} \psi(x))_f^{(f_i)} (\bar{\psi}(y))_c^{(f_i)} \gamma_{cd}^\mu (\psi(y))_d^{(f_f)} (\bar{\psi}(x))_e^{(f_f)} (\gamma_5)_{ef} \right\rangle \tag{3.128}$$

$$= - \left\langle \text{Tr} \left[(G_{f_f}(z, z))_{ba} (\gamma_5)_{ab} \right] \text{Tr} \left[(G_{f_i}(x, y))_{fc} \gamma_{cd}^\mu (G_{f_f}(y, x))_{de} (\gamma_5)_{ef} \right] \right\rangle \tag{3.129}$$

$$= - \left\langle \text{Tr} \left[G_{f_f}(z, z) \gamma_5 \right] \text{Tr} \left[G_{f_i}(x, y) \gamma^\mu G_{f_f}(y, x) \gamma_5 \right] \right\rangle \tag{3.130}$$

and for $f_i = sp.$, we similarly have

$$\langle \mathcal{O}_f V^\mu \mathcal{O}_i^\dagger \rangle_{\text{disc. } f_i} = - \left\langle (\bar{\psi}(z))_a^{(f_f)} (\gamma_5)_{ab} (\psi(z))_b^{(f_i)} (\bar{\psi}(y))_c^{(f_i)} \gamma_{cd}^\mu (\psi(y))_d^{(f_f)} (\bar{\psi}(x))_e^{(f_i)} (\gamma_5)_{ef} (\psi(x))_f^{(f_i)} \right\rangle \tag{3.131}$$

$$= - \left\langle \text{Tr} \left[G_{f_f}(y, z) \gamma_5 G_{f_i}(z, y) \gamma^\mu \right] \text{Tr} \left[G_{f_i}(x, x) \gamma_5 \right] \right\rangle. \tag{3.132}$$

3.8 Continuum Renormalisation

As noted in previous sections, we must be careful when extrapolating lattice results to the continuum because the lattice spacing a must taken to 0, removing the UV-regulation. Renormalising the lattice results in order to make the extrapolation well-defined can be a complex topic; for this project the procedure is relatively simple. We introduced the renormalisation conditions for RHQ and DWF quarks in sections 3.6.2 and 3.6.3 respectively, and saw that—for our purposes—their bound states can be multiplicatively renormalised. We have yet to discuss the renormalisation of the RHQ-DWF bilinear, or the techniques by which we can obtain the renormalisation factors. We can begin with the RHQ-DWF bilinear.

As we noted in section 2.7.2, we can obtain the form factors of interest from the matrix elements $\langle P|V^\mu|B\rangle$ that enter three-point functions. Following [137, 138], we renormalise the current as

$$Z_V^{bl} = \rho\sqrt{Z_V^{bb} Z_V^{ll}}, \tag{3.133}$$

where Z_V^{bb} and Z_V^{ll} are renormalisation coefficients for the $b \to b$ and $l \to l$ vector currents, and ρ is a residual correction expected to be close to 1 due to most of the contributions cancelling [139].

Since DWF propagators can be assumed to negligibly break chiral symmetry, we can use the result that $Z_V = Z_A$ under chiral symmetry to identify these up to $\mathcal{O}(am_{\text{res}})$. We refer to [140] for the value of Z_A^{ll} calculated on the gauge ensembles utilised in our calculation.

The coefficient Z_V^{bb} can be computed from the vector current between two $B_{(s)}$ mesons as [141]

$$Z_V^{bb} = \frac{\langle B_{(s)} B_{(s)}^\dagger \rangle}{\langle B_{(s)} V_0 B_{(s)}^\dagger \rangle}, \tag{3.134}$$

by using the fact that

$$Z_V^{bb} \langle B_{(s)} V_0 B_{(s)}^\dagger \rangle = 2M_{B_{(s)}}, \tag{3.135}$$

where V^0 is the flavour-conserving current $\bar{b}\gamma^0 b$, and we can determine the renormalisation factor by fitting the ratio of the two-point to three-point function in the region where the ground state is dominant.

The residual renormalisation coefficient ρ was calculated alongside the current improvement coefficients [135] with mean-field improved lattice perturbation theory [136]. Putting these pieces together, we can calculate the renormalisation coefficient for the RHQ-DWF bilinear.

Chapter 4

Lattice QCD for Heavy-Light Semileptonic Decays

4.1 Calculation Background

4.1.1 Overview

In the previous chapters, we have introduced the background physics and calculation techniques for our processes of interest, $B \to \pi\ell\nu$ and $B_s \to K\ell\nu$. As a reminder, we ultimately seek to calculate the CKM matrix element $|V_{ub}|$ from the decay equation

$$\frac{d\Gamma(B_{(s)} \to P\ell\nu)}{dq^2} = \frac{G_F^2|V_{ub}|^2}{24\pi^3}\frac{(q^2-m_\ell^2)^2\sqrt{E_P^2-M_P^2}}{q^4 M_{B_{(s)}}}\times \left[\left(1+\frac{m_\ell^2}{2q^2}\right)M_{B_{(s)}}^2(E_P^2-M_P^2)\left|f_+(q^2)\right|^2+\frac{3m_\ell^2}{8q^2}\left(M_{B_{(s)}}^2-M_P^2\right)^2\left|f_0(q^2)\right|^2\right], \quad (4.1)$$

for the final state $P = \pi$ or $P = K$, where the form factors $f_+(q^2)$ and $f_0(q^2)$ must be calculated using non-perturbative techniques. Although we have outlined the procedure by which these form factors are calculable with lattice QCD, we have yet to introduce the methods we use to extract the form factors from the three-point functions and the techniques to extrapolate the lattice results to the continuum limit, and across the full q^2 range accessible to the decay and experiment. We shall rectify this situation in this chapter.

Experimental results typically probe the entire q^2 range for these decays, although they are more precise at low q^2. For $B \to \pi\ell\nu$ this is $0 \leq q^2 \leq 26.4\,\text{GeV}^2/c^2$, and it is $0 \leq q^2 \leq 23.7\,\text{GeV}^2/c^2$ for $B_s \to K\ell\nu$.

4.1.2 Form factors *via* $f_\perp$ and $f_\parallel$

As previously stated, the form factors f_+ and f_0 enter a standard parameterisation of the matrix element $\langle P|V^\mu|B_{(s)}\rangle$,

$$\langle P|V^\mu|B_{(s)}\rangle = f_+(q^2)\left(p^\mu_{B(s)} + p^\mu_P - \frac{M^2_{B_{(s)}} - M^2_P}{q^2}q^\mu\right) + f_0(q^2)\left(\frac{M^2_{B_{(s)}} - M^2_P}{q^2}q^\mu\right), \quad (4.2)$$

where $p_{B_{(s)}}$ is the momentum of the $B_{(s)}$ meson, p_P is the momentum of the P meson, and q^μ is the momentum transfer to the $W^\pm$ boson. The momentum transfer is therefore defined by

$$q^2 = (p^\mu_{B_{(s)}} - p^\mu_P)^2. \quad (4.3)$$

However, (2.63) is a non-trivial expression to extract f_+ and f_0 from. We can make a cleaner extraction of information from the matrix element by taking an alternative parameterisation in terms of the form factors $f_\parallel$ and $f_\perp$:

$$\langle P|V^\mu|B_{(s)}\rangle = \sqrt{2M_B}\left[v^\mu f_\parallel(E_P) + p^\mu_\perp f_\perp(E_P)\right] \quad (4.4)$$

where v^μ is the $B_{(s)}$ meson four-velocity, and $p^\mu_\perp = p^\mu_P - (p_P \cdot v)v^\mu$.

In the rest frame of the $B_{(s)}$ meson,

$$v^\mu \to (1, \vec{0}), \quad (4.5)$$

$$p^\mu_\perp \to (0, p^i_P), \quad (4.6)$$

which causes $f_\perp$ and $f_\parallel$ to each be dependent on either the spatial and temporal components only:

$$f_\parallel = \frac{\langle P|V^0|B_{(s)}\rangle}{\sqrt{2M_{B_{(s)}}}} \quad (4.7)$$

$$f_\perp = \frac{\langle P|V^i|B_{(s)}\rangle}{\sqrt{2M_{B_{(s)}}}}\frac{1}{p^i} \quad (4.8)$$

where no sum is implied over i; $f_\perp$ is equal for the three spatial dimensions. This decoupling of the components of the matrix elements in the form factor definitions greatly simplifies their extraction.

Ultimately, we are interested in f_0 and f_+. We can perform a simple linear combination of $f_\parallel$ and $f_\perp$ to recover these form factors,

$$f_0(q^2) = \frac{\sqrt{2M_B}}{M^2_{B_{(s)}} + E^2_P}\left[(M_{B_{(s)}} - E_P)f_\parallel(q^2) + (E^2_P - M^2_{B_{(s)}})f_\perp(q^2)\right], \quad (4.9)$$

$$f_+(q^2) = \frac{1}{\sqrt{2M_{B_{(s)}}}} \left[f_\parallel(q^2) + (M_{B_{(s)}} - E_P) f_\perp(q^2) \right]. \tag{4.10}$$

4.1.3 Extracting Form Factors from Three-Point Functions

We have yet to discuss the issue of extracting $\langle P|V^\mu|B_{(s)}\rangle$ from the three-point function, which contains several other factors. These factors could be removed *via* appropriate data analysis, but we can instead take use alternative method of cancelling off these additional factors by taking ratios of three-point and two-point functions. In practice, correlations between the two-point and three-point functions can yield improved statistics with this method.

Taking the definitions of two-point and three-point functions from (3.108) and (3.123), we can see that

$$\frac{C^\mu_{B\to\pi}(t)}{\sqrt{C_P(t) C_{B_{(s)}}(t_{\text{snk}} - t)}} = \frac{\sum_{n,m} \frac{e^{-E^i_m t} e^{-E^f_n (t_{snk} - t)}}{4E^i_m E^f_n} Z^{(n)}_P Z^{(m)}_{B_{(s)}} \langle P^{(n)}|V^\mu|B^{(m)}_{(s)}\rangle}{\sqrt{\left(\sum_n \frac{e^{-E_n t}}{2E_n}(Z^{(n)}_P)^2\right)\left(\sum_m \frac{e^{-E_m (t_{\text{snk}} - t)}}{2E_m}(Z^{(m)}_{B_{(s)}})^2\right)}}. \tag{4.11}$$

For $0 \ll t \ll t_{\text{snk}}$, it should be a good assumption that the ground-state is dominant. We can then take $m = 0$, $n = 0$ in (4.11) and re-arrange to find

$$R_{\text{gnd}}(t, t_{\text{snk}}) = \lim_{0 \ll t \ll t_{\text{snk}}} \frac{C^\mu_{B\to\pi}(t)}{\sqrt{C_P(t) C_{B_{(s)}}(t_{\text{snk}} - t)}} \sqrt{\frac{4E_P M_{B_{(s)}}}{e^{-tE_P} e^{-(t_{\text{snk}} - t) M_{B_{(s)}}}}} = \langle P|V^\mu|B_{(s)}\rangle. \tag{4.12}$$

We can also take a more relaxed time constraint by also including the first excited states for $B_{(s)}$ and P. It can be useful to instead take a ratio of the three-point function to "reduced" two-point functions,

$$C'_P(t) = \left(\sum_n \frac{e^{-E_n t}}{2E_n}(Z^{(n)}_P)^2\right) - \frac{e^{-E_1 t}}{2E_1}(Z^{(1)}_P)^2, \tag{4.13}$$

such that when we assume ground- and first-excited state dominance, $C'_P(t)$ is equal only to the ground-state. This simplifies the expansion of (4.11), which reduces to

three terms:

$$R_{\text{exc.}}(t, t_{\text{snk}}) = \lim_{0 \ll t \ll t_{\text{snk}}} \frac{C^{\mu}_{B\to\pi}(t)}{\sqrt{C'_P(t) C'_{B_{(s)}}(t_{\text{snk}} - t)}} \sqrt{\frac{4 E_P M_{B_{(s)}}}{e^{-t E_P} e^{-(t_{\text{snk}} - t) M_{B_{(s)}}}}} \tag{4.14}$$

$$\begin{aligned} &= \langle P | V^{\mu} | B_{(s)} \rangle + \\ &\quad \langle P^{(1)} | V^{\mu} | B^{(0)}_{(s)} \rangle \sqrt{\frac{Z^{(1)}_P}{Z^{(0)}_P}} \sqrt{\frac{E^{(0)}_P}{E^{(1)}_P}} \sqrt{e^{-t\left(E^{(1)}_P - E^{(0)}_P\right)}} + \\ &\quad \langle P^{(0)} | V^{\mu} | B^{(1)}_{(s)} \rangle \sqrt{\frac{Z^{(1)}_{B_{(s)}}}{Z^{(0)}_{B_{(s)}}}} \sqrt{\frac{E^{(0)}_{B_{(s)}}}{E^{(1)}_{B_{(s)}}}} \sqrt{e^{-(t_{\text{snk}} - t)\left(E^{(1)}_{B_{(s)}} - E^{(0)}_{B_{(s)}}\right)}}. \end{aligned} \tag{4.15}$$

In practice, replacing the two-point functions with "reduced" two-point functions has an insignificant effect on the results but increases numerical instability, so we use (4.15) as a model for a ratio utilising the unaltered two-point functions.

4.2 Continuum Phenomenology

4.2.1 SU(2) Heavy Meson Chiral Perturbation Theory

Chiral perturbation theory (ChiPT), as introduced in section 2.5, is insufficient to describe $B_{(s)} \to P\ell\nu$ processes in the continuum limit. These decays involve heavy-quark fields not present in the octet field Π that describes only the pseudo-Goldstone bosons living in the $\mathrm{SU}(3)_{\mathrm{V}}$-flavour symmetry of ChiPT. A synthesis of chiral perturbation theory and heavy quark effective theory (HQET), termed heavy-meson chiral perturbation theory (HMChiPT), was formulated to describe this situation [142–145]. A thorough review is available in Manohar and Wise [146], which much of this discussion is based upon.

The starting point is to introduce a heavy-light super-field from HQET [146]

$$H^a = \frac{1 + \not{v}}{2} \left[(P^*_{\mu})^a \gamma^{\mu} - P^a \gamma^5 \right], \tag{4.16}$$

where $(P^*_{\mu})^a$ and P^a annihilate vector and scalar heavy-light quark bilinears (such as B and B^*) respectively, and v is the four-velocity of the heavy quark. The super-field H_a transforms under a chiral symmetry $\mathrm{SU}(3)_{\mathrm{V}}$-flavour subgroup as an anti-triplet

$$H^a \to H^b V^{\dagger}_{ba}, \tag{4.17}$$

where $V^{\dagger}_{ba}$ is an $\mathrm{SU}(3)_{\mathrm{V}}$ transform, and H_a also transforms under an $\mathrm{SU}(2)$ heavy quark spin symmetry from HQET as a doublet

$$H_a \to D_Q(R) H_a, \tag{4.18}$$

where R is an element of the $\mathrm{SU}(3)_R$ symmetry group of the ChiPT Lagrangian, and D_Q is an element of the $\mathrm{SU}(2)$ heavy quark spin symmetry. This HQET field is not necessarily consistent with the ChiPT Lagrangian, since it does not transform under the full $\mathrm{SU}(3)_{\mathrm{L}} \times \mathrm{SU}(3)_{\mathrm{R}}$ symmetry without a particular choice of representation [146]. One such choice is

$$\hat{H}_a = \hat{H}_b L^{\dagger}_{ba}, \tag{4.19}$$

where L is an element of the $\mathrm{SU}(3)_{\mathrm{L}}$ symmetry. As a consequence of the implied parity transformation law, it is useful to couple the H field not to the unitary field Σ introduced in equation (2.60), but rather to the field

$$\xi = \sqrt{\Sigma}. \tag{4.20}$$

These fields are the basis of HMChiPT. To describe the continuum behaviour of our lattice simulations, we take full-QCD next-to-leading order expressions for the form factors for this effective theory from [147]. We also note, following [148], that for physical-mass strange quarks the full $\mathrm{SU}(3)_{\mathrm{L}} \times \mathrm{SU}(3)_{\mathrm{R}}$ chiral symmetry is an unnecessary complication since there is no need to extrapolate in the strange quark mass. We can therefore instead use the isospin-limit chiral symmetry $\mathrm{SU}(2)_{\mathrm{L}} \times \mathrm{SU}(2)_{\mathrm{R}}$ which describes only the up and down quarks as briefly described in section 2.5. To align conventions with [148], we will refer to this as $\mathrm{SU}(2)$ HMChiPT for brevity. Furthermore, the pion/kaon final states in nearly all of the simulation parameter-space have energies much larger than the rest masses. We can therefore describe the form factors in the hard-pion/kaon limit, following [149]. The ultimate product of these modifications is the two form factor descriptors

$$f_{\text{pole}}(M_P, E_P, a) = \frac{\Lambda}{E_P + \Delta}\left(c^{(0)}\left(1 + \frac{\delta f(M_\pi) - \delta f(M_\pi^{\text{phys}})}{(4\pi f)^2}\right) + c^{(1)}\frac{\Delta M_P^2}{\Lambda^2} + c^{(2)}\frac{E_P}{\Lambda} + c^{(3)}\frac{E_P^2}{\Lambda^2} + c^{(4)}a^2\Lambda^2\right), \tag{4.21}$$

$$f_{\text{no pole}}(M_P, E_P, a) = \left(c^{(0)}\left(1 + \frac{\delta f(M_\pi) - \delta f(M_\pi^{\text{phys}})}{(4\pi f)^2}\right) + c^{(1)}\frac{\Delta M_P^2}{\Lambda^2} + c^{(2)}\frac{E_P}{\Lambda} + c^{(3)}\frac{E_P^2}{\Lambda^2} + c^{(4)}a^2\Lambda^2\right), \tag{4.22}$$

where $c^{(n)}$ are fit parameters, Δ is the energy of a resonance typically below the production threshold of the decay, f_π is the pion decay constant, Λ is the chiral scale 1 GeV, $\Delta M_P^2 = M_P^2 - \left(M_P^{\text{phys}}\right)^2$, and $\delta f(M_\pi)$ is a "chiral log" introduced by the one-loop order terms. Its definition differs for the particular process we are interested in:

$$\delta f^{B\to\pi}(M_\pi) = -\frac{3}{4}(1+3g_b^2)M_\pi^2 \log\left(\frac{M_\pi^2}{\Lambda^2}\right), \tag{4.23}$$

$$\delta f^{B_s\to K}(M_\pi) = -\frac{3}{4}M_\pi^2 \log\left(\frac{M_\pi^2}{\Lambda^2}\right), \tag{4.24}$$

where g_b is the $B^*B\pi$ coupling constant. We additionally add a finite-volume term by modifying the chiral log as

$$M_\pi^2 \log\left(\frac{M_\pi^2}{\Lambda^2}\right) \to M_\pi^2 \log\left(\frac{M_\pi^2}{\Lambda^2}\right) + \frac{4M_\pi}{L}\sum_{\vec{r}\neq\vec{0}}^{L^3} \frac{K_1\left(|\vec{r}|M_\pi L\right)}{|\vec{r}|}, \tag{4.25}$$

where K_1 is a modified Bessel function of the second kind, and $\vec{r}$ is the spatial position vector of a lattice site in the L^3 volume.

4.2.2 z-expansions

Experiment results are generally binned into q^2 values throughout the accessible q^2 range; in order to make our lattice results available over the full q^2 range we must perform an extrapolation. The preferred way to do this is by using the z-expansion, which requires us to change variables from q^2 to z [150, 151]:

$$z(q^2,t_0) = \frac{\sqrt{1-q^2/t_+}-\sqrt{1-t_0/t_+}}{\sqrt{1-q^2/t_+}+\sqrt{1-t_0/t_+}}, \tag{4.26}$$

where $t_+ = M_{B_{(s)}} + M_P$ and t_0 is a free parameter. This parameterisation maps q^2 on to a unit circle, and allows us to expand the form factors as a convergent power series in z:

$$P_i(q^2)\phi_i(q^2,t_0)f_i(q^2) = \sum_{k=0}^{\infty} a_i^{(k)}(t_0)z(q^2,t_0)^k, \tag{4.27}$$

where i is 0 or $+$, referring to a fit for f_0 or f_+ respectively; P_i are "Blaschke factors" that must vanish for sub-threshold poles, and ϕ_i are "outer functions" that can be any analytic function of q^2. There is therefore a choice that can be made in the definition of the outer function; different outer functions correspond to different parameterisations in z. The free parameter t_0 can also be chosen to accelerate the convergence of the expansion.

There are two commonly-employed forms of this power series, known as the Boyd-Grinstein-Lebed (BGL) [150] and Bourrely-Caprini-Lellouch (BCL) [152]

parameterisations. In the BGL parameterisation, the outer functions are chosen such that the coefficients a have a simple unitarity constraint [153]

$$\sum_{k=0}^{N} (a_i^{(k)})^2 \lesssim 1, \tag{4.28}$$

which is true for any order N. The BCL parameterisation, on the other hand, chooses outer functions such that the functional form takes a simple shape, with a degree of freedom can be removed from the series expansion to obtain the following expressions for the form factors, for a pole at m_{pole}:

$$f_+(q^2) = \frac{1}{1 - q^2/m_{\text{pole}}^2} \sum_{k=0}^{N-1} a_+^{(k)} \left[z^k - (-1)^{k-K} \frac{k}{K} z^K \right] \tag{4.29}$$

$$f_0^{\text{no pole}}(q^2) = \sum_{k=0}^{N-1} a_0^{(k)} z^k \tag{4.30}$$

$$f_0^{\text{pole}}(q^2) = \frac{1}{1 - q^2/m_{\text{pole}}^2} \sum_{k=0}^{N-1} a_0^{(k)} z^k \tag{4.31}$$

The BCL parameterisation takes t_0 to be

$$t_0 = (M_i + M_f) \left(\sqrt{M_i} - \sqrt{M_f} \right)^2, \tag{4.32}$$

where M_i is the mass of the initial state, and M_f is the mass of the final state.

For any z-expansion, we can also remove an additional degree of freedom by enforcing the kinematic constraint that $f_0(0) = f_+(0)$.

4.2.3 Lepton Universality Ratios

As we saw in in section 2.3, leptons of different flavours in the Standard Model couple to the weak gauge bosons identically. This accidental flavour symmetry is known as *lepton universality*, and is a prediction of the Standard Model. We should, therefore, observe decay rates that depend only on their masses, and not on asymmetric flavour-dictated interactions. One way to test this is to form ratios of the decay rates for the individual flavours by integrating the differential decay rate over the kinematic ranges accessible to the relevant lepton masses. With knowledge of the form factors and the assumption of lepton universality, we can evaluate the ratio of decay rates under the standard model. A deviation between the standard model prediction and experimental results would then indicate lepton flavour universality violation, and a signal of new physics. These "R ratios" have the key advantage that the CKM matrix elements cancel in their construction, removing a large source of uncertainty.

The R ratio is defined as

$$R(P) = \frac{\int_{m_\tau^2}^{q^2_{\max}} dq^2 \frac{d\Gamma\left(B_{(s)}\to P\tau\overline{\nu}_\tau\right)}{dq^2}}{\int_{m_\ell^2}^{q^2_{\max}} dq^2 \frac{d\Gamma\left(B_{(s)}\to P\ell\overline{\nu}_\ell\right)}{dq^2}}, \tag{4.33}$$

where ℓ is either e or μ. This form of the ratio is chosen because the relatively large τ mass makes the ratio sensitive to f_0, whereas this term is negligible for e and μ masses. This means that non-perturbative calculations are a requirement for determining these ratios, as has been long known [154].

The traditional definition of the R-ratio given above does provide a test of lepton universality, but has the drawback that it is insensitive to the q^2 region $m_\ell^2 \leq q^2 \leq m_\tau^2$. We propose to use an alternative ratio to monitor lepton universality, following [155], which addresses this issue. We implement this with two key changes to the ratio definition:

- We change the lower integration limit of the denominator to m_τ^2 to match the numerator, as proposed in [155–157],
- We modify the weighting on the form factors in the denominator to depend on a common lepton mass, as in [155].

These changes make the largest part of the integrands—the F_V term—the same in the numerator and the denominator. We hope that this cancellation will lead to an increase in precision when evaluating the new ratio with our lattice form factors.

To implement this, we first re-write the differential decay rate as

$$\frac{d\Gamma\left(B_{(s)}\to P\ell\nu\right)}{dq^2} = \Phi(q^2)\omega_\ell(q^2)\left[F_V^2 + \left(F_S^\ell\right)^2\right], \tag{4.34}$$

where

$$\Phi(q^2) = \eta_{\rm EW}\frac{G_F^2|V_{\rm ub}|^2}{24\pi^3}|\vec{k}|, \tag{4.35}$$

$$\omega_\ell(q^2) = \left(1-\frac{m_\ell^2}{q^2}\right)^2\left(1+\frac{m_\ell^2}{2q^2}\right), \tag{4.36}$$

$$F_V^2 = \vec{k}^2\left|f_+(q^2)\right|^2, \tag{4.37}$$

$$\left(F_S^\ell\right)^2 = \frac{3}{4}\frac{m_\ell^2}{m_\ell^2+2q^2}\frac{\left(M_{B_{(s)}}-M_P^2\right)^2}{M_{B_{(s)}}^2}\left|f_0(q^2)\right|^2. \tag{4.38}$$

We now re-define the R-ratio as the "improved" R-ratio

$$R^{\text{impr}}(P) = \frac{\int_{m_\tau^2}^{q^2_{\text{max}}} dq^2 \frac{d\Gamma\left(B_{(s)} \to P\tau\overline{\nu}_\tau\right)}{dq^2}}{\int_{m_\tau^2}^{q^2_{\text{max}}} dq^2 \frac{\omega_\tau(q^2)}{\omega_\ell(q^2)} \frac{d\Gamma\left(B_{(s)} \to P\ell\overline{\nu}_\ell\right)}{dq^2}}. \tag{4.39}$$

Noting that the $\left(F_S^\ell\right)^2$ term is negligible for e and μ masses, we can drop this term from the denominator and simplify this expression to

$$R^{\text{impr}}(P) \approx 1 + \frac{\int_{m_\tau^2}^{q^2_{\text{max}}} dq^2 \Phi(q^2)\omega_\tau(q^2)\left(F_S^\tau\right)^2}{\int_{m_\tau^2}^{q^2_{\text{max}}} dq^2 \Phi(q^2)\omega_\tau(q^2)F_V^2}. \tag{4.40}$$

Chapter 5

Simulation Details and Data Analysis

5.1 Introduction

Having introduced the background for the semileptonic processes $B \to \pi\ell\nu$ and $B_s \to K\ell\nu$, and for the lattice formulation used to simulate these processes, we now turn to the specifics of setting up our calculation. We will begin in section 5.2 with a discussion of the ensembles that are used in this calculation, before moving on to the simulation parameters of the fermion actions we use in section 5.3. In section 5.4 we address the diagrams contributing to the quantities we need to compute, and any further simulation parameters we have yet to discuss. We introduce the statistical bootstrap in section 5.5, and describe how we can use it to propagate correlated errors through our analysis. Finally, we discuss our data fitting procedure in section 5.6.

5.2 Lattice Ensembles

As mentioned in section 3.5.1, we use the RBC-UKQCD 2+1 flavour DWF-Iwasaki gauge ensembles [120–122]. These ensembles make use of the renormalisation-improved Iwasaki gauge action (section 3.5.1) and domain-wall fermion sea quarks (section 3.6.3). These ensembles feature dynamical u, d, and s quarks in the isospin limit, such that the u and d quarks share a unitary light quark mass and become functionally degenerate flavours since electromagnetic effects are also neglected. Hereafter we will refer to a light l quark in place of the lattice u and d quarks. The existence of two degenerate flavours plus the independent strange quark mass is represented by the "2+1 flavour" terminology in the gauge ensemble definition. We note that $2 + 1 + 1$ flavour gauge ensembles—which also include a

Ensemble	$L^3 \times T$ / a^4	a^{-1} / GeV	am_l^{sea}	am_s^{sea}	M_π / MeV	# Configs	# Hits
C1	$24^3 \times 64$	1.785	0.005	0.040	338	1636	1
C2	$24^3 \times 64$	1.785	0.010	0.040	434	1419	1
M1	$32^3 \times 64$	2.383	0.004	0.030	301	628	2
M2	$32^3 \times 64$	2.383	0.006	0.030	362	889	2
M3	$32^3 \times 64$	2.383	0.008	0.030	411	544	2
F1S	$48^3 \times 96$	2.785	0.002144	0.02144	234	98	24

TABLE 5.1: The subset of RBC-UKQCD 2+1 flavour DWF-Iwasaki gauge ensembles [120–122] used in this calculation. From left-to-right, we list the ensemble name, site count per spatial (L) and temporal (T) dimension, inverse lattice spacing, light-quark mass, pion mass, number of calculated gauge configurations, and time sources per configuration. Both the lattice spacing and meson masses are determined from [162–164], and the sea quarks are simulated with the Shamir domain-wall fermion action [13, 14].

dynamical charm quark—are becoming more common in modern lattice calculations where charm sea-quark effects contribute to the correlation functions (see recent results by, *e.g.*, [33, 158–161]).

A summary of important properties of the ensembles used in this calculation are given in table 5.1. To improve statistics on our observables, we make multiple "hits" on ensembles with fewer configurations. These are calculations on the same configuration, but with a time and space translation of the source and sink positions—shifting by a sufficient number of timeslices to acceptably suppress correlations between measurements—that are averaged together to produce a combined result per configuration. As noted in section 3.3, the simulated configurations are separated sufficiently in Monte-Carlo time to suppress correlations between them.

The reason for choosing these ensembles is to map out the a- and M_π- dependence of the $f_\parallel$ and $f_\perp$ form factors for $B \to \pi\ell\nu$ and $B_s \to K\ell\nu$ (section 4.1.2), such that they can be extrapolated to their continuum, physical-mass values with heavy meson chiral perturbation theory (section 4.2.1). We highlight that the work presented in this project features the F1S ensemble, which provides an additional lattice spacing not present in the 2015 RBC-UKQCD calculation that this project seeks to update [90]. As we will see in sections 6.4 and 6.5, this additional ensemble provides a substantial improvement on the uncertainty in the continuum extrapolation.

Ensemble	$L^3 \times T$	a^{-1} / GeV	M_5	L_s	am_l^{sea}	am_s^{val}	am_s^{phys}
C1	$24^3 \times 64$	1.785	1.8	16	0.005	0.03224	0.03224(18)
C2	$24^3 \times 64$	1.785	1.8	16	0.010	0.03224	0.03224(18)
M1	$32^3 \times 64$	2.383	1.8	16	0.004	0.025	0.02477(18)
M2	$32^3 \times 64$	2.383	1.8	16	0.006	0.025	0.02477(18)
M3	$32^3 \times 64$	2.383	1.8	16	0.008	0.025	0.02477(18)
F1S	$48^3 \times 96$	2.785	1.8	12	0.002144	0.02144	0.02167(20)

TABLE 5.2: Properties of the DWF propagators used in this project. As with the gauge ensembles, the light and strange quarks are simulated with the Shamir domain-wall fermion action [13, 14]. The light valence quarks are simulated at the same masses as the light sea quarks, and the valence quarks use the values am_l^{val} which are within 10% of the physical quark masses.

5.3 Quark Propagators

5.3.1 DWF Propagators

Our l and s quark propagators are generated using the DWF action, using boundary conditions anti-periodic in time. We use unphysical light-quark masses equal to those of the sea quarks, and the strange quark masses are tuned to within 10% of their physical value. We take $M_5 = 1.8$, and $L_s = 16$ for the C and M ensembles, and $L_s = 12$ for the $F1S$ ensemble. All DWF propagators are generated with point sources. We summarise the simulation parameters of the DWF quarks in table 5.2. We induce momenta with norms that are integer multiples of lattice units in the DWF propagators by inserting an appropriate momentum exponential at the propagator source.

5.3.2 b Propagator

For b propagators, we utilise the RHQ action with boundary conditions anti-periodic in time. We generate both point- and smeared-source propagators, with the latter introduced to suppress excited-state contamination of the ground state. For the smeared propagators, we use the smearing parameters determined in [165] for the C and M ensembles, and for the F ensemble we scale these parameters to the $F1S$ lattice size. We will henceforth denote smeared operators with a tilde in any equations. The RHQ parameters are given in table 5.4, after a discussion of the tuning procedure. The smearing parameters are given in table 5.3.

	$L^3 \times T$	a^{-1} / GeV	σ_G	N_G
C	$24^3 \times 64$	1.785	7.86	100
M	$32^3 \times 64$	2.383	10.36	170
F	$48^3 \times 96$	2.785	12.14	230

TABLE 5.3: Smearing parameters on the three lattice spacings used in this analysis. Parameters on the C and M ensembles are repeated from [165], and the F ensemble parameters have been scaled in accordance with the lattice spacing. The smearing width for a Gaussian smearing function is given as σ_G, with the number of smearing steps N_G.

5.3.3 RHQ Action Tuning

The RHQ parameters am_0, c_{sw}, ζ are tuned in accordance with the procedure given in [165], based on the lattice spacing determined in [121, 162–164]. We use the B_s meson to tune the parameters. The parameters are tuned such that the spin-averaged mass

$$\overline{M}_{B_s} = \frac{M_{B_s} + 3M_{B_s^*}}{4} \tag{5.1}$$

and hyperfine splitting

$$\Delta M_{B_s} = M_{B_s^*} - M_{B_s} \tag{5.2}$$

reproduce their experimental values [4], and that the rest and kinematic masses of the B_s meson are equal

$$\frac{M_1^{B_s}}{M_s^{B_s}} = 1, \tag{5.3}$$

i.e. the B_s meson obeys the continuum dispersion relation

$$E_{B_s}^2 = M_{B_s}^2 + \vec{p}^2 \tag{5.4}$$

up to $\mathcal{O}(\vec{p}^4)$.

To carry out the tuning procedure, we match the physical observables to the RHQ parameters in the region where we can assume a linear relationship,

$$\begin{pmatrix} \overline{M}_{B_s} \\ \Delta M_{B_s} \\ \frac{M_1^{B_s}}{M_s^{B_s}} \end{pmatrix} = J \cdot \begin{pmatrix} m_0 a \\ c_{\text{sw}} \\ \zeta \end{pmatrix} + A, \tag{5.5}$$

where J is a 3×3 "gradient" matrix and A is an "intercept" vector. We construct J and A by measuring the spin-averaged mass, hyperfine splitting, and rest/kinematic mass

ratio as a set of vectors Y on seven parameter sets:

$$X_0 = \begin{pmatrix} m_0 a \\ c_{\rm sw} \\ \zeta \end{pmatrix}, \quad X_{m_0 a+} = \begin{pmatrix} m_0 a + \sigma_{m_0 a} \\ c_{\rm sw} \\ \zeta \end{pmatrix}, \quad X_{m_0 a-} = \begin{pmatrix} m_0 a - \sigma_{m_0 a} \\ c_{\rm sw} \\ \zeta \end{pmatrix},$$

$$X_{c_{\rm sw}+} = \begin{pmatrix} m_0 a \\ c_{\rm sw} + \sigma_{c_{\rm sw}} \\ \zeta \end{pmatrix}, \quad X_{c_{\rm sw}-} = \begin{pmatrix} m_0 a \\ c_{\rm sw} - \sigma_{c_{\rm sw}} \\ \zeta \end{pmatrix},$$

$$X_{\zeta+} = \begin{pmatrix} m_0 a \\ c_{\rm sw} \\ \zeta + \sigma_\zeta \end{pmatrix}, \quad X_{\zeta-} = \begin{pmatrix} m_0 a \\ c_{\rm sw} \\ \zeta - \sigma_\zeta \end{pmatrix},$$

and then construct J and A as

$$J = \left(\frac{Y_{m_0 a+} - Y_{m_0 a-}}{2\sigma_{m_0 a}}, \frac{Y_{c_{\rm sw}+} - Y_{c_{\rm sw}-}}{2\sigma_{c_{\rm sw}}}, \frac{Y_{\zeta+} - Y_{\zeta-}}{2\sigma_\zeta} \right), \quad A = Y_0 - J \cdot X_0. \tag{5.6}$$

We can then obtain the tuned RHQ parameters by inverting (5.5) to linearly interpolate within the parameter box as

$$\begin{pmatrix} m_0 a \\ c_{\rm sw} \\ \zeta \end{pmatrix}^{\rm RHQ} = J^{-1} \cdot \left(\begin{pmatrix} \overline{M}_{B_s} \\ \Delta M_{B_s} \\ \frac{M_1^{B_s}}{M_s^{B_s}} \end{pmatrix}^{\rm PDG} - A \right), \tag{5.7}$$

if the tuned parameters lie outside the initially chosen box—*i.e.* if the linear relationship does not hold—we repeat the analysis on a new set of parameters guided by the failed iteration step until we can successfully interpolate an RHQ parameter set corresponding to the required PDG values. The specific values we take for the spin-averaged mass and hyperfine splitting are, respectively,

$$\overline{M}_{B_s} = \frac{1}{4}\left(5366.82^{+0.22}_{-0.22} + 3 \times 5415.4^{+1.8}_{-1.4}\right)\ \text{MeV} = 5403.26^{+1.8}_{-1.4}\ \text{MeV}, \tag{5.8}$$

$$\Delta M_{B_s} = 48.6^{+1.8}_{-1.6} MeV, \tag{5.9}$$

which we refer to [4] for. We make a conservative choice for the error on the spin-averaged mass by setting it equal to the full error on $M_{B_s^*}$; the uncertainty in the tuning procedure is in any case dominated by the error on ΔM_{B_s}. We take the tuned parameters from [165] on the C and M as an initial guess for those ensembles, and use these results scaled by the F ensemble lattice size to obtain an initial guess for the F ensemble. We perform two iterations of the tuning procedure to obtain parameter sets for each ensemble, and do not find evidence of curvature within the parameter box. We cannot resolve a dependence of the RHQ parameters on the light sea-quark mass,

and so we average determinations on the C and M ensembles—there is only one F ensemble, so cannot also take an average for the fine lattice spacing—to obtain one set of averaged RHQ parameters per lattice spacing.

Calculating the mass of the B_s and B_s^* for a given set of RHQ parameters requires an analysis of two-point functions for these mesons calculated using lattice QCD. Since the technique will be described in section 6.2 during the presentation of the project results, we refer ahead to that section for the fitting procedure so that we do not dilute the discussion of the tuning procedure. To extract the masses, we use a ground state analysis following section 6.2.

We must also consider systematic error effects on the values of the RHQ parameters. The central values and errors of the RHQ parameters are reported in table 5.4, and we will now discuss the systematics that enter our determination.

- First, we consider heavy-quark discretisation errors in the RHQ action using a power-counting method, as discussed in [165], following the method outlined in [166]. We re-tune the RHQ parameters using a spin-averaged mass, hyperfine splitting, and rest/kinematic mass ratio adjusted by the uncertainties given in [165], and take the subsequent change in the parameter values as a systematic due to heavy-quark discretisation.
- We convert experimental data to lattice units using the lattice spacing during the tuning procedure, and therefore must account for effect of the error on the lattice spacing on the RHQ parameters. We re-tune on all ensembles with the lattice spacings adjusted by $\pm 1\sigma$ and take the largest deviation in the parameters for each of the three lattice spacings as the error on the appropriate ensembles.
- We must also account for the experimental uncertainty on the PDG values that enter the tuning procedure, in the form of the errors on the spin-averaged mass and hyperfine splitting. We again re-tune the parameters with $\pm 1\sigma$ on the experimental inputs and take the largest deviation for each lattice spacing as the error on the appropriate ensembles.
- We also account for the error due to a mis-tuning of the strange quark to its physical mass. On the C ensembles, where we have tuned to the physical mass, we re-measure the RHQ parameters using strange quarks of mass 0.030 and 0.040. We assume a linear dependence of the RHQ parameters on the strange mass between these bounds, and estimate the effect on the RHQ parameters by adjusting the strange mass by $\pm 1\sigma$ from its physical value and calculating the shift in the parameters from the slope. For the M ensembles, we have used a strange mass not tuned to the physical value, but instead a value 1σ above at 0.025. Here, we include a second strange quark mass of 0.0272 and extrapolate the RHQ parameters to the physical value to estimate the mis-tuning error. For

	a^{-1} / GeV	$m_0 a$	c_{sw}	ζ
C	1.785	7.471(51)(75)(82)(45)	4.92(13)(28)(07)(24)	2.929(63)(100)(15)(03)
M	2.383	3.485(25)(38)(45)(31)	3.06(07)(18)(05)(15)	1.760(30)(58)(07)(02)
F	2.785	2.423(62)(36)(31)(29)	2.68(13)(15)(04)(13)	1.523(79)(43)(05)(02)

TABLE 5.4: RHQ parameter central values and errors on the C, M, and F groups of ensembles. The quoted errors are, from left-to-right, the statistical error, heavy quark discretisation error, lattice spacing error, and experimental error.

the *F*1*S* ensemble, we save computational resources by re-using the slopes from the *M* ensembles—since the gradient of the slope decreases with increasing lattice spacing—and make a conservative estimate of the mis-tuning error by calculating the change in the RHQ parameters due to a $\pm 2\sigma$ shift in the used strange mass, which is within 1σ of the physical value. In all cases, we find a potential mis-tuning error of $\leq 0.3\%$. Compared to the other systematics this is small, and we neglect to include it in our final tally.

A plot of the dependence of the $B_s \to K\ell\nu$ form factors on the RHQ parameters for the C1 ensemble is given in figure 5.1. As shown in the plot, the form factors are linear in the parameter in the vicinity of the box.

5.4 Correlators

5.4.1 Diagrams

We need to enumerate all diagrams contributing to the two-point and three-point functions in our calculation. We refer back to section 3.7 for an enumeration of possible contributing diagrams to the involved classes.

For the $\pi^{\pm}$, we have two different quark flavours and thus only have a connected diagram. The π^0, however, has the quark content

$$\frac{u\bar{u} - d\bar{d}}{\sqrt{2}} \tag{5.10}$$

and in principle we should also have a disconnected contribution. However, since we work in the isospin limit, *i.e.* we use a unitary light quark mass where $m_u = m_d$, the disconnected contributions from π_0 final states cancel due to the masses being the same, and we need only consider the connected diagram. This also has the consequence that we need only a single connected diagram to describe all three π final states, and they are hence indistinguishable in our calculation.

The kaon, B, and B_s mesons also only have a connected contribution due to having two different quark flavours.

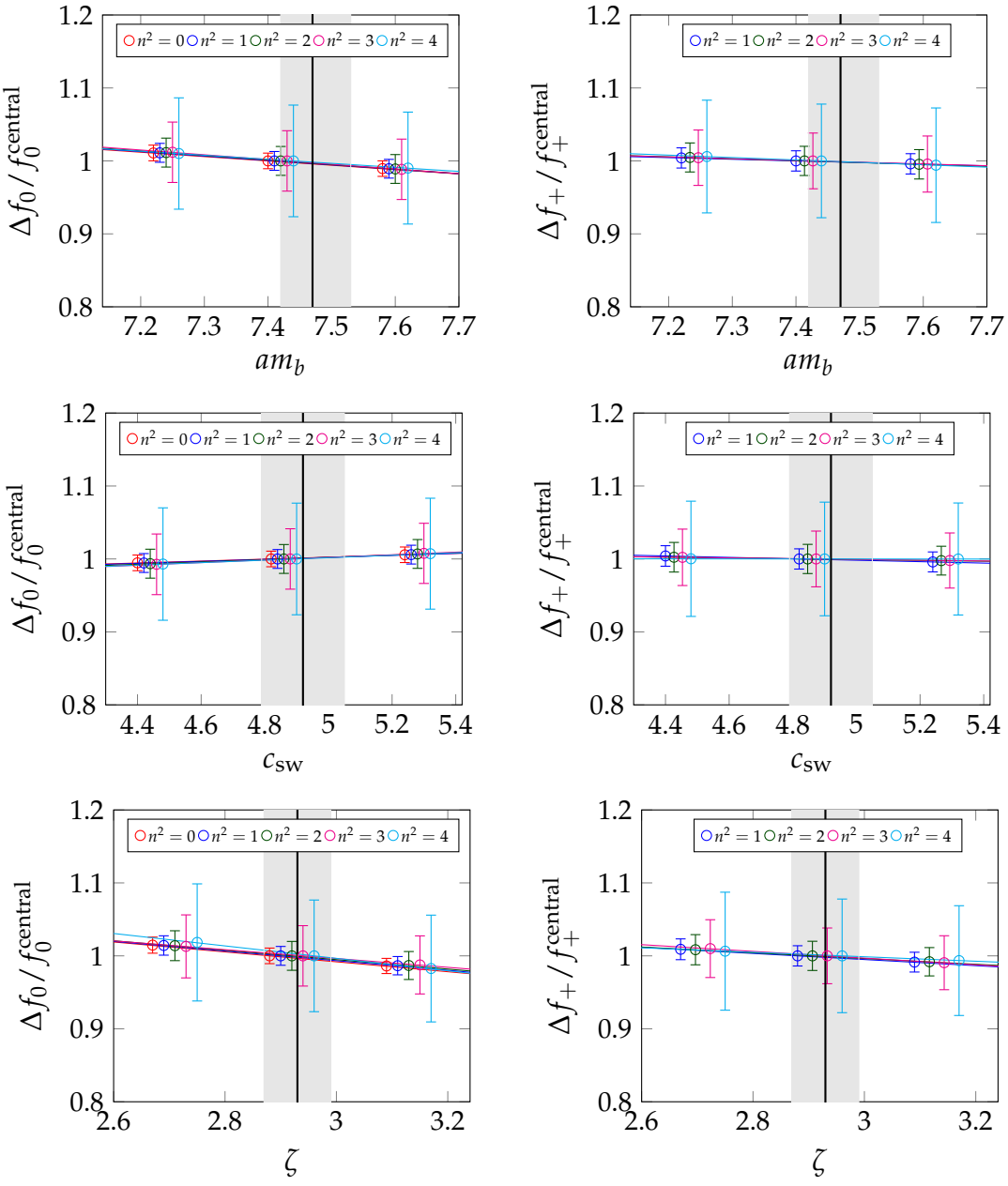

FIGURE 5.1: Dependence of the form factors f_0 and f_+ on the RHQ parameters for $B_s \to K\ell\nu$ on the C1 ensemble. For all momenta, no evidence of curvature in parameter dependence is observed. Our tuned values are indicated by a vertical black line, and the uncertainties by the grey bands. Points at different momenta for the same parameter values are offset for visual clarity; they take each the average RHQ parameter value for each of the three clusters of points shown per plot.

For the three-point functions, the $B_s \to K$ involves three distinct quark flavours and thus only has a connected contribution. For $B \to \pi$, the $B^0 \to \pi^{\pm}\ell^{\mp}\nu$ process involves three distinct quark flavours and also only has a connected contribution. Following an argument from isospin symmetry once more, the unitary light quark leads to a cancellation in the expected disconnected diagrams for the charged B decay. We therefore do not distinguish between these $B \to \pi\ell\nu$ decay paths in our results.

We therefore have only a single class of connected diagrams per correlation function that must be computed.

5.4.2 Source-Sink Separation

When choosing the source-sink separation, we have multiple factors to consider. A separation that is too small will not show a clear ground state signal, since excited-state contaminations originating at the source and sink timeslices will not have enough time to sufficiently decay. Conversely, increasing the source-sink separation also increases the statistical error. We must therefore attempt to find a balance that allows for a good ground state signal, whilst also giving us a good statistical error. The optimal source-sink separation for the C ensembles was studied in [90], and we re-use the separation for the C and M from here (20 and 26 timeslices respectively). For the $F1S$, we take a source-sink separation of 30 timeslices. The F separation has been chosen by scaling the C separation with the ratio of lattice spacings on these ensembles, such that the distance is approximately equal in physical units on all ensembles.

In [90], in order to determine the optimal source-sink separation, three-point functions for several separations were generated. These were generated for the C1 and M1 ensembles, the ensembles with the lightest sea-quark masses, and hence the most sensitive to excited-state effects on each lattice spacing. The separations that resulted in ratios with a good balance between a clear plateau and error size were then taken as the appropriate source-sink separations—20 and 26 on C1 and M1 respectively—which correspond to the same physical distance.

5.5 Statistical Techniques and Error Propagation

Correlators are defined as an average over path configurations, so in order to build correlators we must average over our simulation results. However, this alone would only give an average value of the correlator, so in order to estimate errors it is typical to use resampling methods. A resampling method utilises averages of subsets of a total sample to build a "resampled data set" that can be used to estimate statistical

observables; for lattice QCD, this amounts to computing the properties of a list of correlators built from various subsets of the total number of configurations available. This list of resampled correlators can then be treated as samples from the underlying distribution of the correlator, and we can perform operations on each of these resamples individually to obtain similar estimators for secondary observables derived from the correlators. In this way, we can propagate errors on to secondary observables that also account for correlations in the data *via* these estimators of probability distributions.

For this project we make use of bootstrap resampling [167]. For some random variable x, the bootstrap defines a mean and variance for an estimator $\tilde{x}$ by generating a resampled data set consisting of K "bootstrap samples" that can be used to compute statistical properties. The mean and variance for the bootstrap estimator $\tilde{x}$ are given respectively by

$$\langle \tilde{x} \rangle = \frac{1}{K} \sum_k b_k; \;\; \sigma^2_{\tilde{x}} = \frac{1}{K} \sum_k \left(b_k - \langle \tilde{x} \rangle \right)^2, \tag{5.11}$$

where b_k is the k^{th} bootstrap sample — the average of N randomly selected values from our data sample with replacement. We note that this particular implementation of the bootstrap assumes that the measurements of x are uncorrelated; since each x represents a configuration and we choose configurations sufficiently separated in Monte-Carlo time to be uncorrelated, this is a valid assumption for our data. Note that the definition of the bootstrap means that a single bootstrap average is virtually guaranteed to include repeats of data points from the original sample; it is relatively straightforward to demonstrate that each bootstrap sample is constructed from $\sim 63\%$ of the original sample for large N.

The number of bootstrap samples chosen is a free parameter; and the estimator $\tilde{x}$ converges to x in the limit $K \to \infty$. A significant advantage of being free to choose the number of bootstrap samples in each resampled data set is that it allows easy comparison between data sets of different sizes. Table 5.1 shows that each of the six ensembles used in this analysis have different sample sizes, so using a bootstrap resampling scheme provides a simple and statistically sound way for us to compute estimators for observables constructed from data over multiple ensembles, such as those in the continuum limit of our simulation.

Since the bootstrap is constructed from averages of randomly-selected data points, the bootstrap estimator carries with it an additional random-sampling error. As the number of bootstrap samples increases, the size of this error will decrease and the estimator error will converge to that of the original data set. For all quantities in this project, we use 500 bootstrap samples.

5.6 Data Fitting

5.6.1 General Procedure

Let us consider some vector of random variables y that we seek to describe with some function $f(\alpha, x)$, where α is a vector of input parameters to f and x is a vector of independent variables. We can use a tuning procedure in order to converge on the vector α that best describes y given the function f. We follow a generalised least-squares fitting procedure in order to optimise α. To do this, we seek to minimise the χ^2 value:

$$\chi^2 = \hat{r}_i W_{ij} \hat{r}_j \tag{5.12}$$

where the residual $\hat{r}$ is given by

$$\hat{r}_i = y_i - f(\alpha, x_i) \tag{5.13}$$

and the weight matrix W is the inverse of the covariance matrix C,

$$C_{ij} = \left\langle (y_i - \langle y \rangle)\,(y_j - \langle y \rangle) \right\rangle . \tag{5.14}$$

We should bear in mind that we are minimising resampled data. This means that we should not only minimise the χ^2 for the mean of the resampled data, but also do this minimisation for each individual bootstrap sample. In this way, we obtain a distribution of values for α and can thus estimate the error on the fit parameters. This means that each bootstrap sample should, in principle, have an individual weight matrix constructed from the covariance matrix for the particular bootstrap sample being fitted. However, in practice this can often prove numerically unstable. To obtain a stable fit, we can make a *frozen approximation* where we use the covariance matrix of the bootstrap mean to weight the fits to the individual bootstrap samples.

To minimise χ^2, we use the MINPACK implementation of the Levenberg-Marquardt algorithm library *via* the scipy package [168]. The Levenberg-Marquardt algorithm is iterative, and at every iteration step shifts the fit parameters $\alpha_i \to \alpha_i + \delta_i$, where δ_i is calculated from

$$\left(J_{ik} J_{kj} + \lambda \operatorname{diag}\left(J_{ik} J_{kj}\right)\right) \delta_j = J_{ij} \hat{r}_j, \tag{5.15}$$

where J_{ij} is the Jacobian matrix of f with respect to α_i, and λ is a damping parameter that can be tuned throughout the minimisation procedure. The algorithm has converged when the size of δ_i is within a supplied tolerance.

5.6.2 Goodness-of-fit

Having determined the optimal set of a parameters to match a particular function to some data, we can then quantify the quality of the fit. The chi-squared distribution—being the probability distribution for a quadrature sum of independent, normally distributed random variables—can be used to draw certain conclusions about our fit. The first statistic we can consider is the chi-squared per degree of freedom, or "reduced chi-squared". As the name implies, this is the ratio of the chi-squared statistic to the number of degrees of freedom in the fit. The optimal value of χ^2_ν is 1; this implies that the average deviation of the fit from the data is in agreement with the standard deviations of the data. The reduced chi-squared therefore gives us a goodness-of-fit statistic; a $\chi^2_\nu \gg 1$ implies that the fit model is not appropriate for the data, and a $\chi^2_\nu < 1$ is a product of overfitting, since we are claiming better knowledge of the data than the error on the data.

We can make a more precise statement about the goodness-of-fit by using the χ^2 to compute a p-value. The p-value is a probability of obtaining a result in at least as much tension with the null hypothesis as our observation, under the assumption that the null hypothesis is true. For these fits, the null hypothesis is "the fit model does not explain the data", which we have a quantitative measure for with the reduced chi-squared statistic. Our least-squares minimisation attempts to find the set of parameters that makes the best case for the alternative hypothesis. Obtaining a bad p-value—we will define the meaning of "bad" once we introduce a quantitative descriptor of the p-value—suggests that either the null hypothesis is incorrect, or we have obtained a very unlikely result. In order to decide whether to reject the null hypothesis, we must decide what counts as an unacceptable level of probability.

The definition of the p-value means that we can calculate it from the cumulative distribution function of our test statistic. The cumulative distribution function of the χ^2-distribution is given by

$$\chi^2_{\text{CDF}}\left(\nu, \chi^2\right) = P\left(\frac{\nu}{2}, \frac{\chi^2}{2}\right), \tag{5.16}$$

where P is the regularised lower incomplete gamma function. We can at this point define two tests:

> **One-Tailed Test**: Define the p-value as one minus the sum of probabilities between $\chi^2 = 0$ and $\chi^2 = \chi^2_{\text{fit}}$:
>
> $$p = 1 - P\left(\frac{\nu}{2}, \frac{\chi^2}{2}\right). \tag{5.17}$$

The p-value peaks with a value of 100% at $\chi^2_{\text{fit}} = 0$, approaches 50% at $\chi^2_{\text{fit}}/\nu = 1$ as $\nu \to \infty$, and tends towards 0 as $\chi^2_{\text{fit}} \to \infty$.

Two-Tailed Test: Define the p-value as twice the minimum value of a one-tailed test and reversed one-tailed test:

$$p = 2\min\left((P\left(\frac{\nu}{2}, \frac{\chi^2}{2}\right), 1 - P\left(\frac{\nu}{2}, \frac{\chi^2}{2}\right)\right). \tag{5.18}$$

The p-value has a peak of 100% at a value of χ^2_{fit}/ν that approaches 1 as $\nu \to \infty$, and tends towards 0 as $\chi^2_{\text{fit}} \to 0$ and $\chi^2_{\text{fit}} \to \infty$.

The one-tailed test only produces a low p-value for fits that do not describe the data well, whereas the two-tailed test also punishes fits that exhibit over-fitting behaviour. Functionally, the choice between these definitions boils down to what we consider a "good" p-value. For the one-tailed test, values a little under 50% correspond to $\chi^2/\nu \approx 1$, and both very large and very low p-values are bad. For the two-tailed test, values a little under 100% correspond to $\chi^2/\nu \approx 1$, and anything far below this is bad. The results presented in section 6 utilise the one-tailed p-value, for which the null hypothesis is rejected if $5\% < p < 95\%$.

It is extremely important to note that the rejection of the null hypothesis does *not* imply that we should accept the alternative hypothesis as true; to do so is a false dichotomy, since in our definition of the p-value we have already stated that statistical outliers will also produce poor p-values. Moreover, without evidence external to the fit, we cannot assume our chosen fit is the only fit with explanatory power — a sufficiently long Taylor series could produce a good p-value, even if such a fit would not tell us much. Ultimately, the p-value does not allow us to accept an alternative hypothesis. Its role is only to tell us whether to reject our proposed fit.
Only if our alternative hypothesis is well-motivated with sufficient supporting evidence or reasoning can we argue that the alternative hypothesis should be accepted. In this project, all fit models considered are motivated by quantum field theory — whether they are well-known calculations of correlation function behaviour or relations motivated by effective field theory. Since the data we collect should also be described by the specific quantum field theories our models are valid for, we can be confident that a fit in sufficient tension with the null hypothesis allows us to take our fit models as having explanatory power of the results — if we satisfy the assumptions of said models.

5.6.3 Simultaneous Fits over Multiple Data Sets

It is often advantageous or necessary to simultaneously fit multiple data sets that each share at least one descriptive parameter with at least one the fit models for another

data set. This can be implemented by putting all relevant data into the data vector y and assigning the appropriate fit model to different elements of y. The most convenient way of doing this is to construct d such that all elements from a particular data set are contiguous; and then we may define the fit function for the ith element of y, $f_i(\alpha, x_i)$, as

$$f_i(\alpha, x_i) = \begin{cases} 0 \leq i < n_0 & : g_0(\beta_0, x_i), \\ n_0 \leq i < n_1 + n_0 & : g_1(\beta_1, x_i), \\ & \dots \\ \sum_{j=0}^{m-1} n_j \leq i < \sum_{j=0}^{m} n_j & : g_m(\beta_m, x_i) \end{cases} \tag{5.19}$$

where n_m is the number of elements in the mth data set entering the fit, g_m is the function applied to the mth data set, and β_m is the subset of fit parameters α used by the fit function g_m. We need then only redefine the residual given in (5.13) by giving f an index as

$$\hat{r}_i = y_i - f_i(\alpha, x_i). \tag{5.20}$$

We can make adjustments to the covariance matrix of y to reflect assumptions about the correlations between the multiple data sets in the fit. A common situation is where the individual data sets should be correlated to themselves but not to each other; in this case, we can set all covariances between variables from different data sets to 0. If y is constructed such that it is the serial concatenation of the constituent data sets, we can think about the covariance matrix as a block matrix, where the diagonal blocks are covariance matrices of the input data sets and off-diagonal blocks are covariances between data sets. To assume zero correlation between data sets, we set all off-diagonal blocks to 0. We make use of such block-diagonal covariance matrices in our continuum fits and q^2 extrapolations, as presented in sections 6.4 and 6.6.

Chapter 6

Results

6.1 Heavy Current Renormalisation

In order to non-perturbatively determine the heavy current renormalisation factor Z_V^{bb}, we make fits to the ratio

$$\frac{C_2(t_{\text{snk}})}{C_3(t, t_{\text{snk}}) - C_3(t-1, t_{\text{snk}})} = Z_V^{bb}, \tag{6.1}$$

where $C_3(t, t_{\text{snk}})$ (see section 3.7 for general definitions of the correlation functions) is a three-point $B_s \to B_s$ function involving the $b \to b$ current $\bar{b}\gamma_0 b$, and C_2 is a B_s two-point function. The results of these fits are given in table 6.1, alongside Z_A^{ll} taken from [121]. Plots of the fits are given in figure 6.1. We obtain good p-values for all fits, with errors ranging from 0.28% on the C1 ensemble to 0.07% on the F1S ensemble, largely consistent on each lattice spacing.

	Z_A^{ll}	Z_V^{bb}	Fit Range	p
C1	0.7172	9.095(25)	[5, 16]	15%
C2	0.7178	9.136(21)	[2, 17]	76%
M1	0.7449	4.777(11)	[7, 19]	33%
M2	0.7452	4.772(06)	[2, 24]	55%
M3	0.7453	4.769(07)	[2, 24]	91%
F1S	0.7624	3.6240(24)	[2, 28]	34%

TABLE 6.1: Renormalisation coefficients for the light- and heavy-quark currents. The given fit ranges are inclusive, and both they and the p value are for the fits producing the Z_V^{bb} values. The corresponding Z_A^{ll} values are taken from [121].

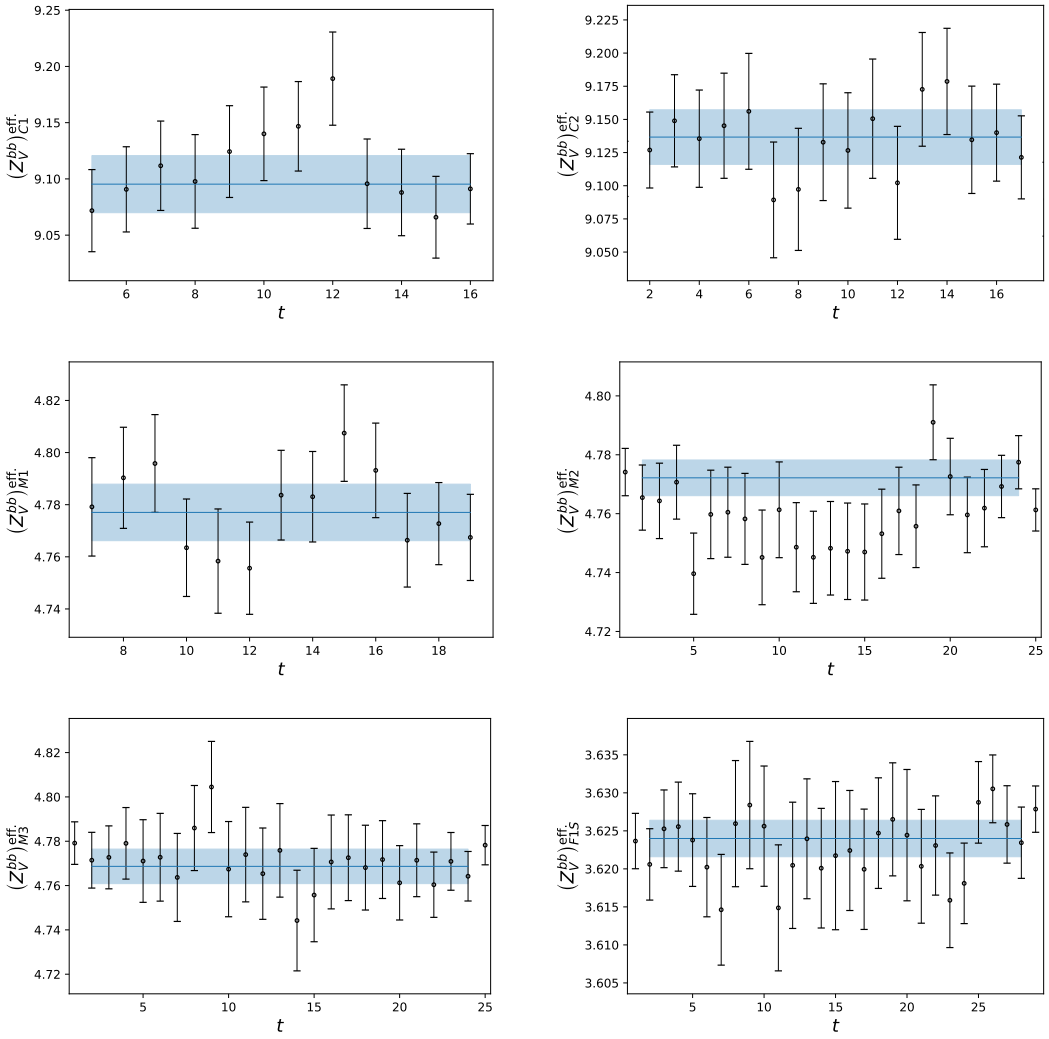

FIGURE 6.1: Fits to the ratio in 6.1 to extract the heavy current renormalisation factor Z_V^{bb}. From left-to-right, then top-to-bottom, are fits for the six ensembles C1, C2, M1, M2, M3, and F1S.

6.2 Two-Point Function Energy Fits

If we refer back to our definitions of the ratios we use to extract form factors from three-point and two-point functions in (4.12) and (4.15), we see that energies of the initial and excited states enter these expressions. As we found in (3.108), the energy also parameterises the analytic behaviour of the two-point functions of these states. Taking into account the backwards-propagating state from periodic boundary conditions, we can describe a lattice two-point function dominated by the ground and first excited states as

$$C(t) = \sum_{n=0}^{n=1} \frac{Z_n^{(a)} Z_n^{(b)}}{2E_n} \left(e^{-tE_n} + e^{-(T-t)E_n} \right), \tag{6.2}$$

where n denontes the nth energy state.

Since we only compute point-point data for the π and K mesons, we perform single-correlator fits to extract energies. For the B_s and B mesons, we need the smear-smear correlator for the three-point function ratios, but also compute point-smear correlators for an improved mass-extraction signal. For the B_s meson, we perform excited-state fits on the point-smear and smear-smear correlators simultaneously to extract the ground and first excited state energies.

However, for the B meson, we find that both the smear-smear and point-smear correlators suppress excited states so successfully that it is difficult to reliably extract the first excited state on all ensembles, in particular the F1S. To remedy this situation, we additionally computed point-point correlators for the B meson. Our fit strategy in this instance is to perform ground state fits on the smear-point and smear-smear correlators alongside an excited state fit on the point-point correlator simultaneously, which stabilises the fits and reduces the error on the fit results. We note that including the point-point correlator on the C2 ensemble for the B meson leads to an unacceptable p-value, however, and for this ensemble we follow the B_s fit strategy of extracting the excited state from the smear-smear and smear-point, since we can obtain a sufficient signal here.

Three fits are performed to generate a single set of fit parameters. First, an uncorrelated fit that excludes any excited states is performed on the input correlators. The results of this fit are used as an initial guess for an uncorrelated fit including excited states, the results of which are then in turn used as an initial guess for a final correlated fit including excited states, from which we quote results. A summary of mass fits on the four mesons is given in table 6.2, and full fit details are given in appendix A. Plots of the mass fits are given in figures 6.2, 6.3, 6.4, and 6.5.

For final state mesons with momenta $n^2 > 0$, we use the lattice dispersion relation to calculate the higher-momentum masses from the rest mass,

$$E_P^{\mathrm{ldr}} = 2\,\mathrm{arcsin}^{-1}\left(\sqrt{\sinh^2\left(\frac{M_P}{2}\right) + \sum_i \sin^2\left(\frac{\pi n_i}{L}\right)}\right), \tag{6.3}$$

where n_i is the ith component of the lattice momentum vector $\vec{n}$ and L is the number of sites per spatial dimension of the lattice.

6.3 Form Factor Extraction

As described in section 4.1.3, we extract the form factors $f_\parallel$ and $f_\perp$ by taking a ratio of the three-point and two-point functions given by equation (4.12) and performing a fit to the resultant plateau. Similar to the strategy for the two-point functions, we begin by making an uncorrelated ground state fit to find a reliable estimate for the form

M [MeV]	C1	C2	M1	M2	M3	F1S
M_{B_s}	5.365(15)	5.368(15)	5.367(21)	5.371(20)	5.376(21)	5.365(21)
M_B	5.302(15)	5.318(15)	5.307(20)	5.314(20)	5.318(20)	5.291(21)
M_K	0.5472(18)	0.5827(18)	0.5371(22)	0.5583(23)	0.5753(25)	0.5314(27)
M_π	0.3398(13)	0.4330(14)	0.3019(16)	0.3625(16)	0.4115(19)	0.2674(16)

TABLE 6.2: Ground-state masses for the four mesons involved in this calculation. Results are for correlated-in-time fits including the ground and first excited states of the mesons. K and π fits are to a single correlator, B_s fits are to smear-point and smear-smear correlators, and the B fits are to point-point, smear-point, and smear-smear correlators. Full fit information is given in Appendix A.

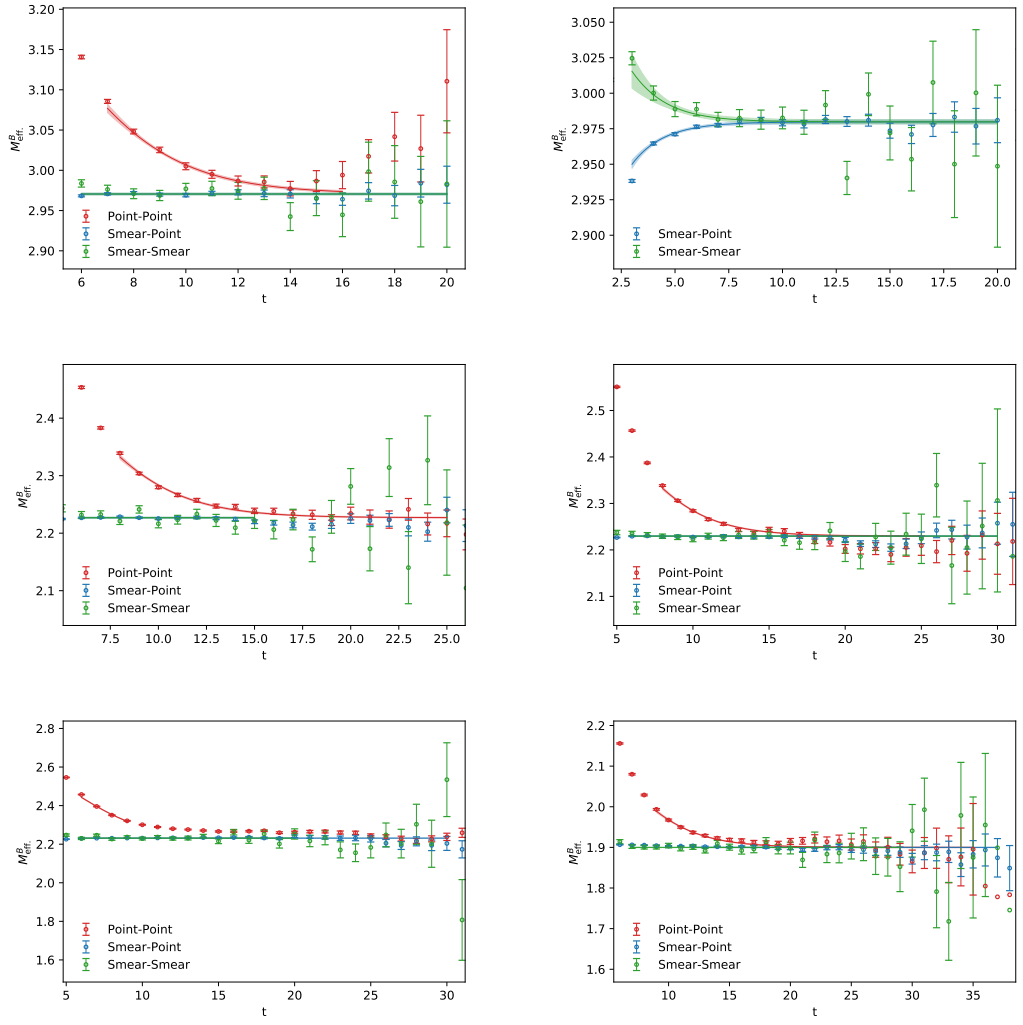

FIGURE 6.2: Two-point function fits to the B meson correlator. From left-to-right, then top-to-bottom, are fits for the six ensembles C1, C2, M1, M2, M3, and F1S.

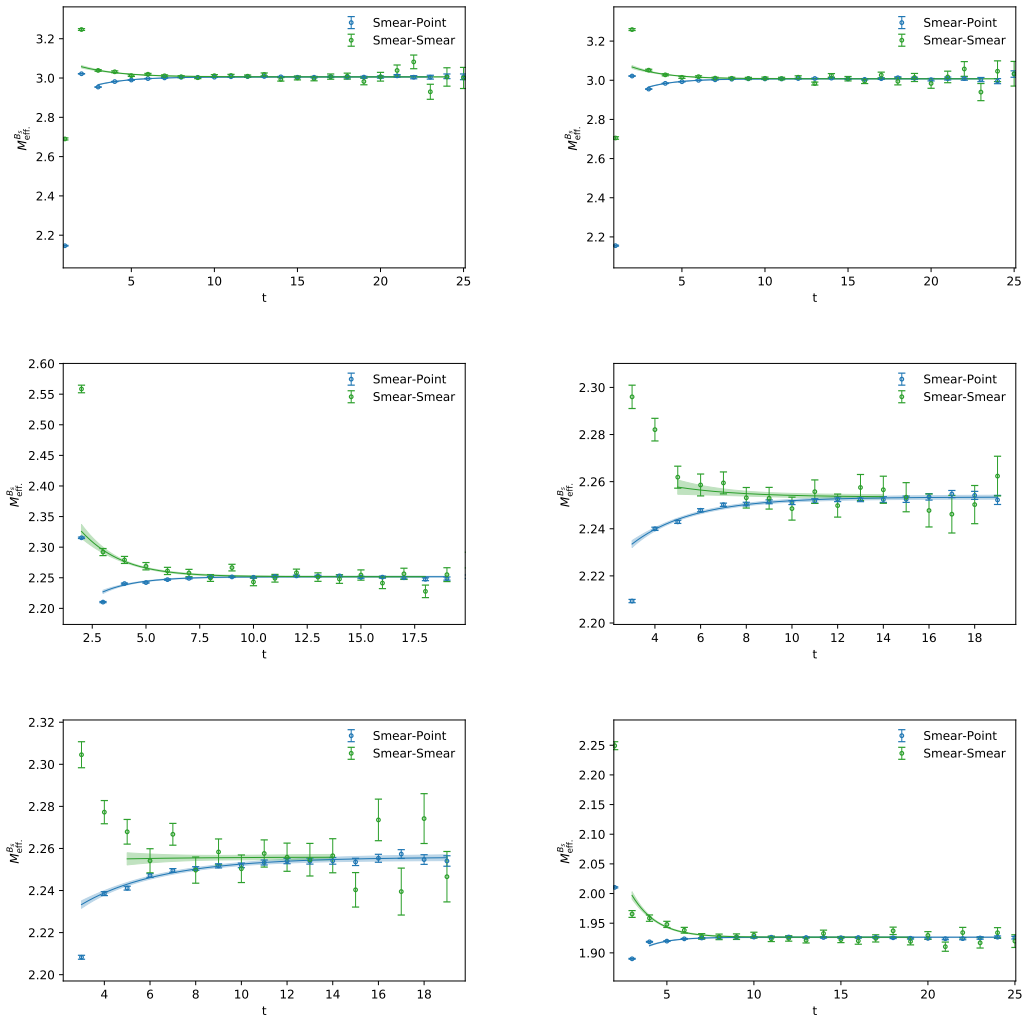

FIGURE 6.3: Two-point function fits to the B_s meson correlator. From left-to-right, then top-to-bottom, are fits for the six ensembles C1, C2, M1, M2, M3, and F1S.

factors. We then use this estimate in the initial guess for an uncorrelated excited state fit, which again informs a correlated excited state fit. The excited state fit we use is a slightly repackaged form of (4.15),

$$\langle P|V^\mu|B_{(s)}\rangle + \alpha\sqrt{e^{-t\left(E_P^{(1)}-E_P^{(0)}\right)}} + \beta\sqrt{e^{-(t_{\text{snk}}-t)\left(E_{B_{(s)}}^{(1)}-E_{B_{(s)}}^{(0)}\right)}}, \tag{6.4}$$

where we have made the definitions

$$\alpha = \langle P^{(1)}|V^\mu|B_{(s)}^{(0)}\rangle \sqrt{\frac{Z_P^{(1)}}{Z_P^{(0)}}}\sqrt{\frac{E_P^{(0)}}{E_P^{(1)}}}, \tag{6.5}$$

$$\beta = \langle P^{(0)}|V^\mu|B_{(s)}^{(1)}\rangle \sqrt{\frac{Z_{B_{(s)}}^{(1)}}{Z_{B_{(s)}}^{(0)}}}\sqrt{\frac{E_{B_{(s)}}^{(0)}}{E_{B_{(s)}}^{(1)}}}. \tag{6.6}$$

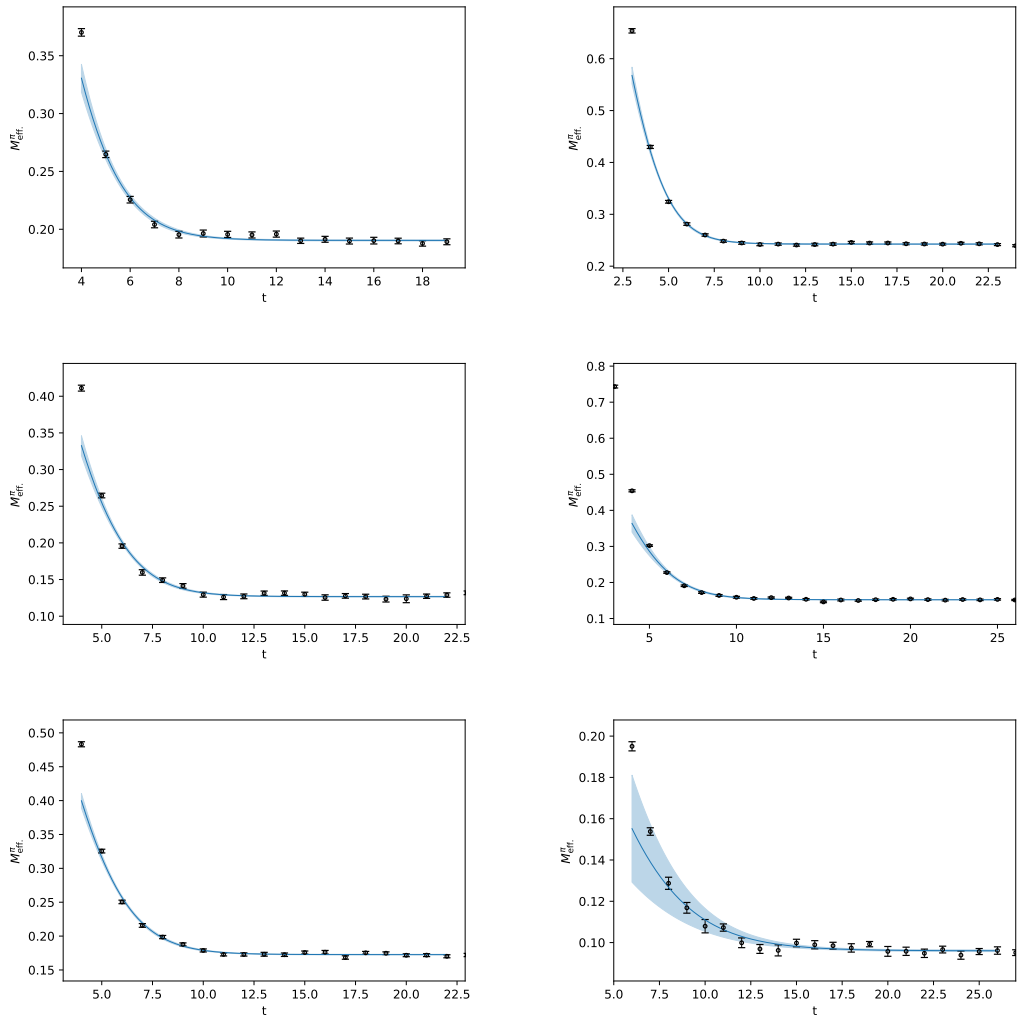

FIGURE 6.4: Two-point function fits to the π meson correlator. From left-to-right, then top-to-bottom, are fits for the six ensembles C1, C2, M1, M2, M3, and F1S.

In principle, we know the eight Z and E factors that enter these definitions and could just fit the two extra unknown matrix elements; however, the precise value of these matrix elements is unimportant to us — we merely need to capture the time-dependence of the excited state contaminations of the plateau and account for these effects in the fit. It proves to be more numerically stable to just fit the α and β parameters as coefficients of the time-dependencies, and so we prefer this rescaled approach over fitting the excited-state matrix elements.

The motivation for including excited states was driven by large excited state contaminations in some ratios, in particular on the F1S $B \to \pi\ell\nu$ data and for some higher-momentum states, where it is not obvious where the plateau lies. We checked the excited state fit against our estimates for the ground state plateau fit, and find excellent agreement with deviations of less than 1σ. We also attempted to include a fourth term in the excited state fit, parameterising the contribution of both the $B_{(s)}$ and

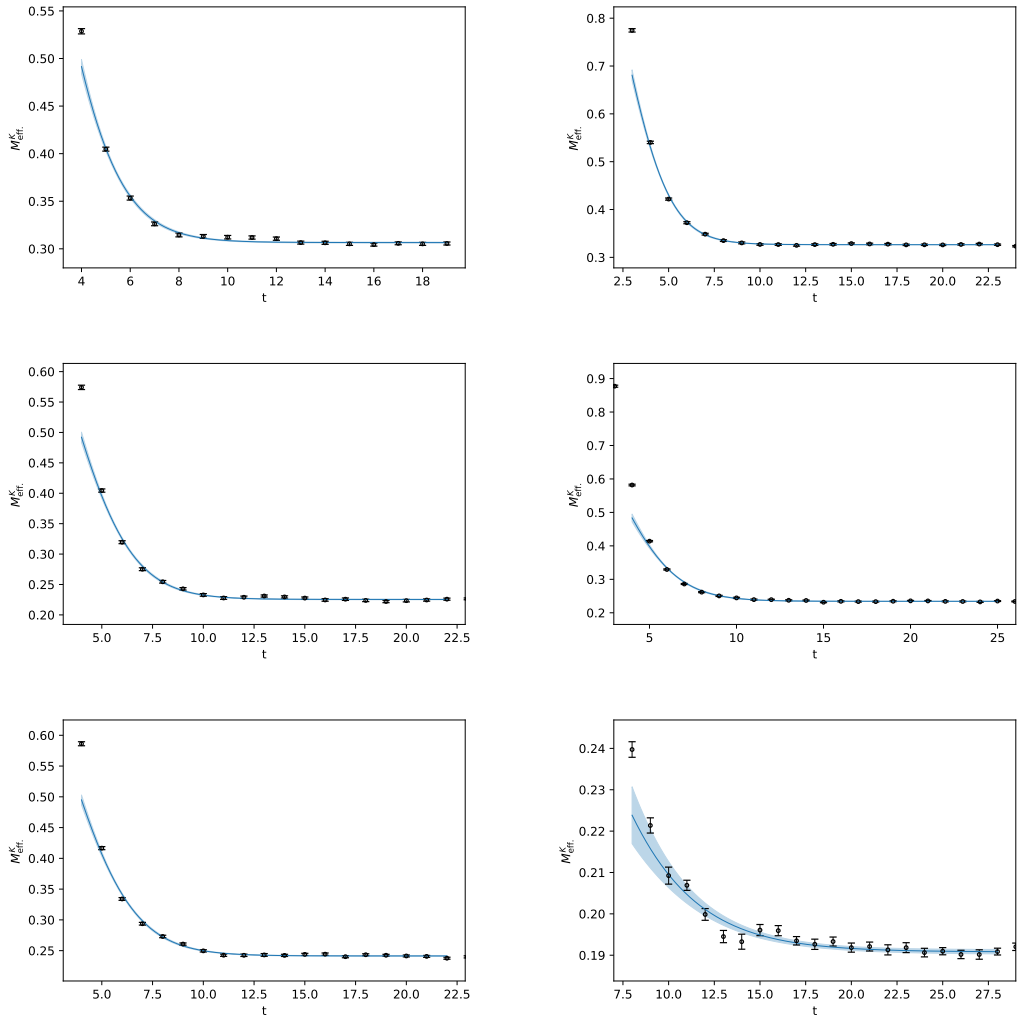

FIGURE 6.5: Two-point function fits to the K meson correlator. From left-to-right, then top-to-bottom, are fits for the six ensembles C1, C2, M1, M2, M3, and F1S.

P mesons in the first excited state. Although this produced successful fits to several ratios and provided excellent descriptions on some F1S ratios across many timeslices, the fits were unstable for many ratios and so we elected to use three-term excited state fits across all ratios. Good p-values are obtained for all fits, as shown in the full results tables given in appendix A.

As stated in section 2.7.2, we obtain the form factors $f_\perp$ and $f_\parallel$ from the fitting procedure, which must then be linearly combined in order to give f_+ and f_0. In tables 6.3 and 6.4, we quote the f_0 and f_+ values resulting from the combination of our fit results for $B_s \to K\ell\nu$ and $B \to \pi\ell\nu$ respectively. Full fit results for $f_\perp$ and $f_\parallel$ are given in appendix A.

	n^2	C1	C2	M1	M2	M3	F1S
$f_0^{B_s\to K}$	0	0.8700(93)	0.8691(89)	0.882(12)	0.881(12)	0.904(21)	0.860(10)
$f_0^{B_s\to K}$	1	0.7284(90)	0.7384(88)	0.739(13)	0.731(10)	0.765(18)	0.771(11)
$f_0^{B_s\to K}$	2	0.635(12)	0.654(12)	0.650(16)	0.648(12)	0.663(19)	0.705(14)
$f_0^{B_s\to K}$	3	0.563(20)	0.598(19)	0.582(27)	0.574(18)	0.603(23)	0.655(17)
$f_0^{B_s\to K}$	4	0.536(32)	0.560(28)	0.494(42)	0.511(31)	0.540(47)	0.600(21)
$f_+^{B_s\to K}$	1	1.987(27)	1.947(24)	2.029(35)	2.010(33)	2.054(63)	2.261(37)
$f_+^{B_s\to K}$	2	1.542(27)	1.511(25)	1.551(34)	1.583(31)	1.622(50)	1.841(32)
$f_+^{B_s\to K}$	3	1.239(36)	1.264(34)	1.234(48)	1.306(36)	1.303(46)	1.591(36)
$f_+^{B_s\to K}$	4	1.075(53)	1.118(48)	1.004(78)	1.087(51)	1.094(62)	1.425(49)

TABLE 6.3: Results for the form factors f_0 and f_+ for the $B_s \to K\ell\nu$ process. The form factors are calculated as a linear combination of $f_\perp$ and $f_\parallel$, as given by equation (4.2). The results are obtained from correlated-in-time fits to the ratios given by (4.12), using the excited-state fit ansatz provided in (6.4). Full fit information for the constituent $f_\perp$ and $f_\parallel$ fits are given in Appendix A.

	n^2	C1	C2	M1	M2	M3	F1S
$f_0^{B\to\pi}$	0	0.966(12)	0.913(13)	1.047(18)	1.002(16)	0.945(13)	1.050(26)
$f_0^{B\to\pi}$	1	0.758(16)	0.748(13)	0.813(25)	0.762(21)	0.761(15)	0.862(26)
$f_0^{B\to\pi}$	2	0.654(28)	0.661(21)	0.692(40)	0.664(24)	0.639(23)	0.750(34)
$f_0^{B\to\pi}$	3	0.557(54)	0.614(39)	0.509(77)	0.592(43)	0.584(39)	0.696(42)
$f_0^{B\to\pi}$	4	0.448(86)	0.554(52)	0.60(14)	0.45(16)	0.453(72)	0.639(91)
$f_+^{B\to\pi}$	1	2.241(52)	2.089(39)	2.376(79)	2.286(62)	2.203(48)	2.890(88)
$f_+^{B\to\pi}$	2	1.676(74)	1.570(43)	1.69(11)	1.765(68)	1.699(61)	2.129(66)
$f_+^{B\to\pi}$	3	1.29(17)	1.386(70)	1.34(23)	1.381(95)	1.262(81)	1.832(88)
$f_+^{B\to\pi}$	4	1.01(29)	1.124(96)	1.05(46)	0.95(19)	1.09(13)	1.51(16)

TABLE 6.4: Results for the form factors f_0 and f_+ for the $B \to \pi\ell\nu$ process. The form factors are calculated as a linear combination of $f_\perp$ and $f_\parallel$, as given by equation (4.2). The results are obtained from correlated-in-time fits to the ratios given by (4.12), using the excited-state fit ansatz provided in (6.4). Full fit information for the constituent $f_\perp$ and $f_\parallel$ fits are given in Appendix A.

6.4 Chiral Continuum Fits

We extrapolate our results to the continuum with the SU(2) heavy-meson chiral perturbation theory expressions given in equations (4.21) and (4.22). We use (4.21) for f_0 and f_+ on both the $B_s \to K\ell\nu$ and $B \to \pi\ell\nu$ processes, taking into account the relevant poles at $\Delta = M_{B^*} - M_{B_{(s)}}$. For f_0, the B^* state carries the quantum numbers $J^P = 0^+$, and for f_+ it takes 1^-. For the 1^- state, we make use of the PDG average [4], and for the 0^+ state we use the theoretical estimate from [169] since no experimental result is available. The numerical values of the constants used in these fits can be found in table 6.5.

For both $B_s \to K\ell\nu$ and $B \to \pi\ell\nu$, we find that the coefficient of the E^2 term is compatible with 0 and do not include it in the fit. When considering the systematic error due to the choice of continuum extrapolation function, we include a fit variation

	f_π	Δ_0	Δ_+	g_b	Λ_χ
$B_s \to K\ell\nu$	130.2 MeV	263 MeV	-41.6 MeV	-	1 GeV
$B \to \pi\ell\nu$	130.2 MeV	305 MeV	45.2 MeV	0.57	1 GeV

TABLE 6.5: Summary of input constants to the continuum fits for both processes. We take f_π from [78], the physical $B_{(s)}$ and $B^*(1^-)$ masses from [4] and theoretical $B(0^+)$ mass from [169] in order to calculate Δ_0 and Δ_+, and g_b—the $B^*B\pi$ coupling constant—from [170].

	c_1	c_2	c_3	c_4	c_5	p
$f_0^{Bs\to K}$	0.529(30)	0.21(11)	0.366(92)	-0.243(69)	-0.073(58)	87%
$f_+^{Bs\to K}$	1.762(38)	-0.04(28)	-0.724(39)	-	-0.24(14)	48%
$f_0^{B\to Pi}$	0.502(25)	0.11(12)	0.45(11)	-0.30(11)	-0.171(58)	87%
$f_+^{B\to Pi}$	1.678(62)	0.26(39)	-0.650(87)	-	-0.34(21)	79%

TABLE 6.6: Chiral-continuum fit results using NLO SU(2) HMχPT to extrapolate lattice results to 0 lattice spacing and physical meson masses.

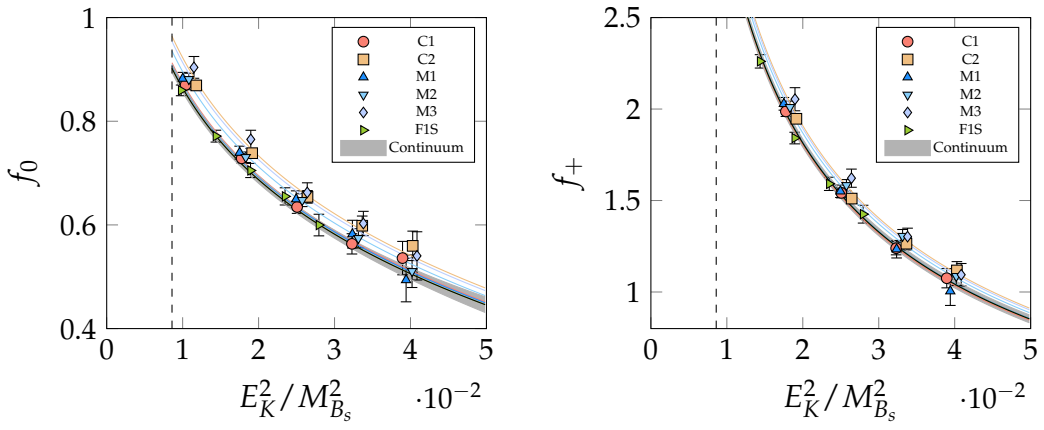

FIGURE 6.6: Chiral continuum fits for $B_s \to K\ell\nu$. The left plot is for f_0, and the right for f_+. The vertical black line indicates the minimum E value at $E = M_K^{\text{phys}}$. The black fit line and grey band are the continuum result and error band respectively.

that does include this term, as will be presented in section 6.5. The fit coefficients for our preferred fits on $B_s \to K\ell\nu$ and $B \to \pi\ell\nu$ are given in table 6.6. Since there are only four fits to report with little additional information necessary, we quote goodness-of-fit statistics in table 6.6 rather than appendix 6.6. Plots of the fits are given in figures 6.7 and 6.6.

6.5 Synthetic Continuum Data and Systematic Errors

6.5.1 Synthetic Data

Having extrapolated our lattice form factors to their continuum limits, we now need to extrapolate across the full q^2 range using the z-expansion (section 4.2.2). In order to

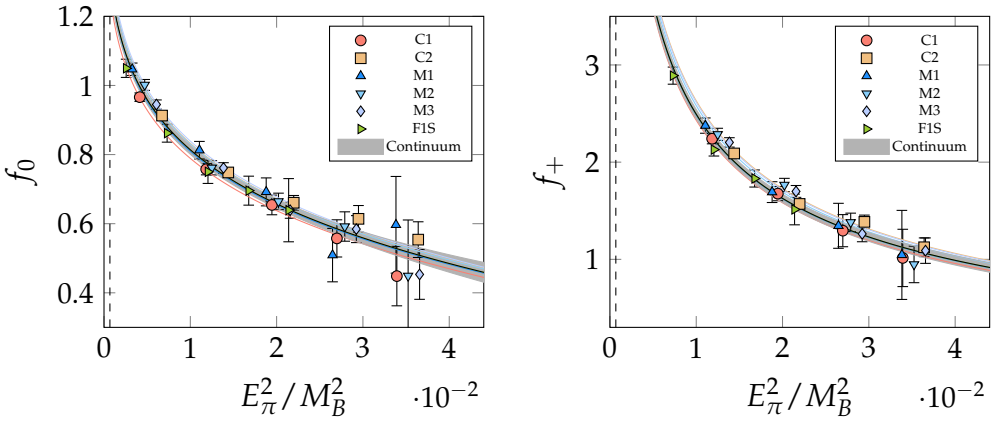

FIGURE 6.7: Chiral continuum fits for $B \to \pi\ell\nu$. The left plot is for f_0, and the right for f_+. The vertical black line indicates the minimum E value at $E = M_\pi^{\text{phys}}$. The black fit line and grey band are the continuum result and error band respectively.

do this, we construct "synthetic data points" at reference q^2 values accessible to our simulations—equally spaced in z, the q^2-dependent expansion parameter used as the independent variable in the z-expansion—such that we have continuum data to fit the z-expansion to.

We choose a number of synthetic data points corresponding to the number of degrees of freedom afforded by our continuum fits. We have five degrees of freedom from the fit parameters; the degrees of freedom in the lattice spacing and pion mass become fixed in the continuum, allowing us to take three synthetic data points. However, the removal of the E^2 term from the f_+ fits costs us another degree of freedom, and we therefore use only two synthetic data points for f_+. We construct the data points between $q^2 = 17.5\,\text{GeV}$ and $q^2 = M_{B_{(s)}} - M_P$ for both processes, with the third f_0 data-point taken at a value of q^2 corresponding to the z halfway between the z-values of the high and low q^2 points.

We also at this point account for systematic errors affecting the continuum result by including these in the total uncertainty of the synthetic data, as described in section 6.5.10. In the remainder of this section, we enumerate the potential contributions to the total error budget from systematic errors and assess their size.

6.5.2 Continuum Fit Systematic

We consider a source of systematic error from the specific forms of our fit Ansätze. The results quoted in section 6.4 are for our preferred choice, but we should consider alternative fit forms resulting from uncertainties on the input constants and the significance of terms in the fit. We perform the following variations to the fit, and take the largest percentage deviation $\left|(f^{\text{preferred}} - f^{\text{variation}})/f^{\text{preferred}}\right|$ at each reference q^2

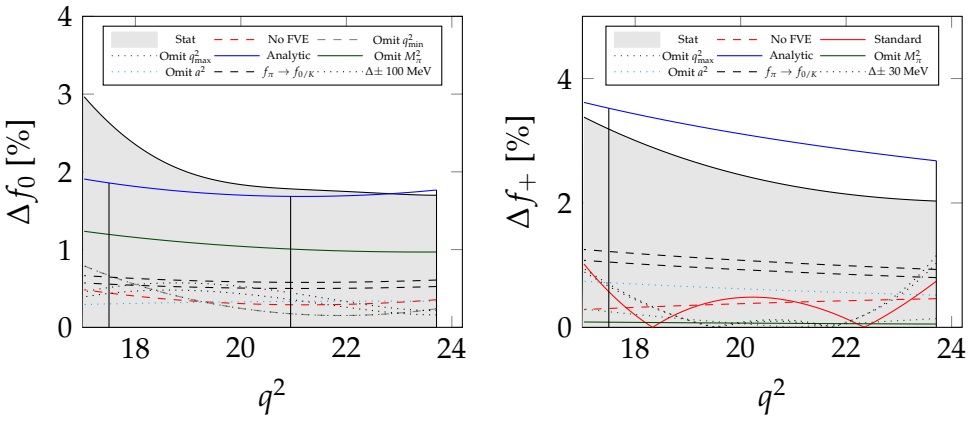

FIGURE 6.8: Percentage deviations from the preferred fit for a set of alternative choices of fit function for the continuum fits of f_0 and f_+ on $B_s \to K\ell\nu$. The grey bands indicate the statistical error.

value out of all variations as the systematic error on that data point due to the fit Ansätze:

- The fit form given in equation 4.21, including finite-volume corrections,
- No finite-volume correction,
- Removing the data points at $n^2 = 0$ (f_0 only),
- Removing the data points at $n^2 = 4$,
- Removing the chiral logarithms ("analytic" fit form),
- Removing the M_π^2 term,
- Removing the a^2 term,
- Replacing f_π with the chiral limit value of f_0 = 112 MeV [121],
- Replacing f_π with the Kaon decay constant f_K = 155.6 MeV [4],
- Varying the f_0 pole mass by 100 MeV,
- Varying the f_+ pole mass by 30 MeV for $B_s \to K$,
- Varying the f_+ pole mass by 10 MeV for $B \to \pi$,
- Varying g_b by $1\sigma = 0.08$ ($B \to \pi$ only).

We report fit coefficients for each variation in appendix A. Plots of the fit variations over the statistical error on the continuum fits are given in figures 6.8 and 6.9.

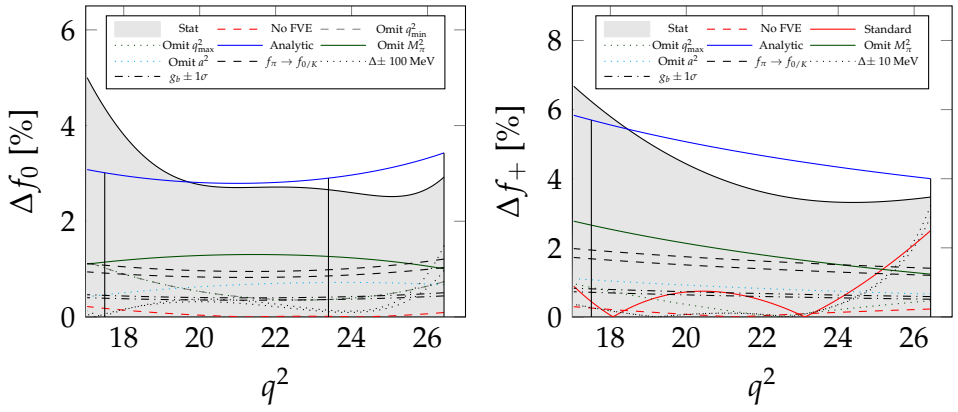

FIGURE 6.9: Percentage deviations from the preferred fit for a set of alternative choices of fit function for the continuum fits of f_0 and f_+ on $B \to \pi\ell\nu$. The grey bands indicate the statistical error.

6.5.3 Lattice Scale Uncertainty

We do not include a systematic for the lattice scale uncertainty, because we already include this in the statistical error of our physical-unit quantities that enter the continuum extrapolation. For each lattice spacing, we build 500 Gaussian-distributed data points—one for each bootstrap sample—centred on the central value of each lattice spacing and distributed with the corresponding standard deviation, and multiply the bootstrap samples of our lattice-unit quantities by these in order to propagate the uncertainty.

6.5.4 Valence Strange Quark Mass Uncertainty

We account for any mis-tuning in the valence strange quark mass, since the $B_s \to K\ell\nu$ form factors feature a valence strange quark. To do this, we re-compute form factors on the C1 ensemble at two additional strange quark masses, and find a linear interpolation for the form factor between these masses. Assuming this interpolation holds on all ensembles, we then use it to compute the fractional change in the form factors if we extrapolate the valence quark mass to the physical value as

$$\frac{\Delta f_{0/+}(am_s)}{\Delta m_s} = \frac{f_{0/+}(am_s) - f_{0/+}(am_s^{\text{phys}})}{f_{0/+}(am_s^{\text{phys}})} \cdot \frac{am_s^{\text{phys}}}{am_s - am_s^{\text{phys}}}, \tag{6.7}$$

for each momentum on each ensemble, and use the largest deviation out of the available momenta. The largest Δm_s is on the F1S ensemble, where we have $am_s^{\text{sim}} = 0.02144$ and $am_s^{\text{phys}} = 0.02167(20)$. This gives us a maximal deviation of

$$\Delta m_s = \left| \frac{am_s^{\text{sim}} - (am_s^{\text{phys}} + \delta am_s^{\text{phys}})}{am_s^{\text{phys}}} \right| \approx 1.98\%. \tag{6.8}$$

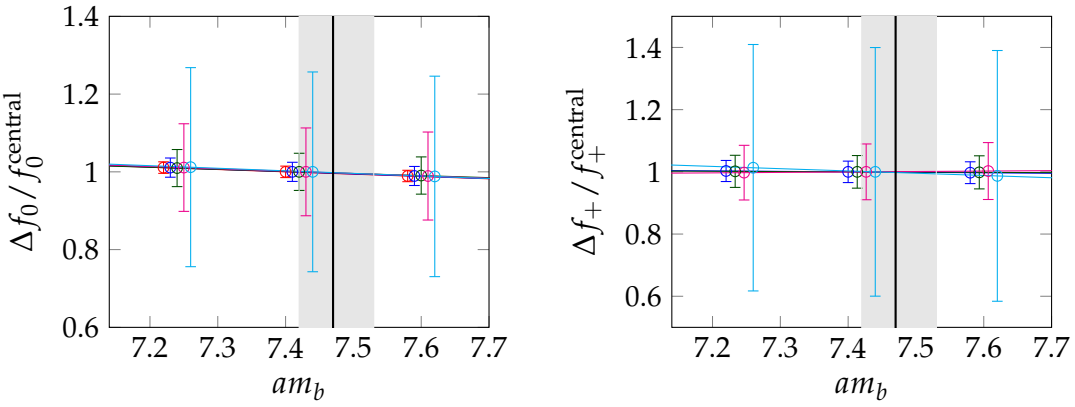

FIGURE 6.10: Dependence of the form factors f_0 and f_+ on the RHQ parameter am_b for $B \to \pi\ell\nu$ on the C1 ensemble. For all momenta, no evidence of curvature in parameter dependence is observed. Our tuned value is indicated by a vertical black line, and the uncertainty by the grey band.

Combined with the corresponding value of $\frac{\Delta f_{0/+}(am_s)}{\Delta m_s}$, this results in an overall maximal change in the form factor of 0.2%. Since this is negligible compared to our other systematic errors, we neglect this contribution.

6.5.5 RHQ Parameters

To estimate the systematic error on the form factors due to any mis-tuning of the RHQ parameters, we partially repeat the box analysis from section 5.3.3. We re-compute the form factors on six variations of the RHQ parameters $\{m_0 a \pm \sigma_{m_0 a}, c_{\text{sw}} \pm \sigma_{c_{\text{sw}}}, \zeta \pm \sigma_\zeta\}$ and make a fit linear in these three parameters to the seven form factor values (including the central data point). We then linearly interpolate the central form factors to those at the three sets of RHQ parameters constructed by increasing one parameter by its uncertainty, and take the quadrature sum of the deviations as the systematic from potential RHQ parameter mis-tuning. We obtain an overall error of 1.8% for f_0 and 1.7% for f_+.

6.5.6 Light Quark Discretisation

We assess several sources of systematic error for the light quarks. We account for the dominant $(a\Lambda_{\text{QCD}})^2$ error in both the DWF quarks and gluons by including an a^2 term in the continuum fit. For higher-order terms, we take $(a\Lambda_{\text{QCD}})^4 \sim 0.10\%$ as the dominant systematic. We also account for errors from residual chiral symmetry breaking from the DWF action, which amounts to $am_{\text{res}} \sim 0.1\%$. There are also several terms from the heavy-light current of size $\mathcal{O}(\alpha_s am_l)$, $\mathcal{O}((am_l)^2)$, and $\mathcal{O}(\alpha_s^2 \Lambda_{\text{QCD}})$. The first two of these effects are negligible at $< 0.1\%$, whereas the third is $\sim 0.78\%$. We add

the light-quark discretisation systematics in quadrature for an overall estimate of 0.79%.

6.5.7 Heavy Quark Discretisation

The RHQ action gives rise to a non-trivial lattice spacing dependence of the form factors in the region $m_0 a \sim 1$. This is due to a mismatch in the coefficients of the higher-order operators in the continuum and discretised theories, with an error on each operator $\mathcal{O}$ in the heavy-quark action and heavy-light current given by

$$(C^{\text{lat}} - C^{\text{QCD}})\langle \mathcal{O} \rangle. \tag{6.9}$$

We estimate the heavy quark discretisation errors using heavy quark effective theory (HQET) power-counting, following the procedure outlined in appendix B of [141], where the continuum and lattice versions of the HQET operators are determined and their difference yields a set of "mismatch functions" that relate the RHQ form factors to the physical observables for our tuned RHQ parameters. We calculate mismatch functions for three sources of lattice spacing dependence. For $\mathcal{O}(a^2)$ errors resulting from the action, we have

$$f_E(m_0 a, c_{\text{sw}}, \zeta) = \frac{1}{8m_E^2 a^2} - \frac{1}{m_2^2 a^2}, \tag{6.10}$$

where

$$\frac{1}{4m_E^2 a^2} = \frac{\zeta^2}{(m_0 a(2 + m_0 a))^2} + \frac{c_{\text{sw}}\zeta}{m_0 a(2 + m_0 a)} \tag{6.11}$$

$$\frac{1}{m_2 a} = \frac{2\zeta^2}{m_0 a(2 + m_0 a)} + \frac{\zeta}{1 + m_0 a}. \tag{6.12}$$

The tree-level coefficients for the $\mathcal{O}(a^2)$ improved heavy-light electroweak operators are given by three mismatch functions,

$$f_{X_1}(m_0 a, c_{\text{sw}}, \zeta) = -\frac{1}{2}\left(d_1^2 - \frac{\zeta}{2(1 + m_0 a)}\right), \tag{6.13}$$

$$f_{X_2}(m_0 a, c_{\text{sw}}, \zeta) = -\frac{1}{2}\left(d_1^2 - \frac{c_{\text{sw}}}{2(1 + m_0 a)}\right), \tag{6.14}$$

$$f_Y(m_0 a, c_{\text{sw}}, \zeta) = -\frac{1}{2}\left(\frac{(\zeta - c_{\text{sw}})(1 + m_0 a)}{m_0 a(2 + m_0 a)} - \frac{d_1}{m_2 a}\right), \tag{6.15}$$

where

$$d_1 = \frac{\zeta(1 + m_0 a)}{m_0 a(2 + m_0 a)} - \frac{1}{2m_2 a}. \tag{6.16}$$

	a^{-1} / GeV	$\alpha_s(a^{-1})$	E	X_1	X_2	Y	3	$f_\parallel$	$f_\perp$
C	1.785	0.2320	0.47	0.67	1.13	1.07	0.93	2.24	2.60
M	2.383	0.2155	0.36	0.43	0.74	0.76	0.63	1.53	1.77
F	2.785	0.2083	0.34	0.35	0.63	0.66	0.54	1.33	1.53

TABLE 6.7: Summary of heavy quark discretisation error contributions, calculated using heavy quark effective theory using the central values of our non-perturbatively tuned RHQ parameters, following appendix B of [141]. The total percentage error on $f_\parallel$ and $f_\perp$ is calculated by adding the errors in quadrature, counting each error the number of times it appears. The 'E' contribution to the action is counted twice, and the '3' action is counted twice for $f_\parallel$ and four times for $f_\perp$, appearing once for each improvement term in the current.

The mismatch function for $\mathcal{O}(\alpha_s^2 a, a^2)$ errors resulting from the current is

$$f_3(m_0 a, c_{\text{sw}}, \zeta) = \alpha_s \zeta \frac{2}{2 + m_0 a}. \tag{6.17}$$

where we take $\alpha_s = \alpha_s^{\overline{MS}}$.

We take a power-counting approach to estimating the leading-order effects from these three functions,

$$\text{error}_n \approx f_n (a\Lambda_{\text{QCD}})^k, \tag{6.18}$$

where f_n are the mismatch functions, $\Lambda_{\text{QCD}} \approx 500$ MeV as implied by fits to inclusive B decays [171], and k is the leading-order lattice spacing dependence of the effects the mismatch functions model; all such effects are $\mathcal{O}(a^2)$ except for f_3, which has a leading $\mathcal{O}(a^1)$ dependence. We obtain an estimate for the total error on the lattice form factors by adding each error in quadrature, counting each error the number of times it occurs in the action and improved current. We tabulate the errors in table 6.7, and propagate the errors onto f_+ and f_0 by transforming these back to $f_\parallel$ and $f_\perp$, applying the errors, and then transforming once more to f_+ and f_0. We use the estimate for our finest lattice spacing on the $F1S$ ensemble as the estimate for the discretisation error.

6.5.8 Renormalisation Factor

The renormalisation factor is constructed from three multiplicative constants—Z_V^{ll}, Z_V^{bb}, and ρ—which we individually consider the errors of, and sum in quadrature to obtain the overall renormalisation factor uncertainty. For Z_V^{ll}, we relate this to Z_A^{ll} *via* the chiral-symmetry relation

$$Z_V^{ll} = Z_A^{ll} + \mathcal{O}(a m_{\text{res}}). \tag{6.19}$$

We take Z_A^{ll} from [121], and note that the overall error on Z_A^{ll} is negligible — it is $\sim 0.02\%$ on the finer ensembles, and $\mathcal{O}(a m_{\text{res}} \approx 0.007$ at $a \approx 0.086$ fm. The error on Z_V^{bb} from our determination is also small; at most $\sim 0.28\%$. The perturbative truncation

	$f_0^{B_s\to K}$			$f_+^{B_s\to K}$	
q^2 [GeV^2]	17.5	20.94	23.71	17.5	23.71
$f(q^2)$	0.481(13)	0.659(12)	0.861(15)	0.977(31)	3.126(63)
Statistics	2.6	1.8	1.7	3.2	2.0
Continuum Fit	1.9	1.7	1.8	3.5	2.7
RHQ	1.3	1.3	1.3	0.8	0.8
HQ	1.5	1.5	1.5	1.4	1.4
Renorm.	0.4	0.4	0.4	1.1	1.1
Imp.	0.1	0.1	0.1	0.3	0.3
IB	0.7	0.7	0.7	0.7	0.7
LQ	0.8	0.8	0.8	0.8	0.8
m_s Sea	0.3	0.3	0.3	0.3	0.3
m_s Val.	0.1	0.1	0.1	0.2	0.2
Total [%]	3.9	3.4	3.4	5.3	5.5

TABLE 6.8: Total error budget for the $B_s \to K\ell\nu$ synthetic data. Errors are given in %. We obtain the total error by adding all contributions in quadrature.

error on ρ is considerably larger and dominates the error estimate for the renormalisation factor, at $\rho_{V_0} \approx 1.7\%$ for $f_\parallel$ and $\rho_{V_i} \approx 0.6\%$ for $f_\perp$. The overall error is, therefore, essentially equivalent to this perturbative truncation error. As with the discretisation errors, we transform f_0 and f_+ back to $f_\parallel$ and $f_\perp$ in order to apply the errors and correctly propagate them through to f_0 and f_+.

6.5.9 Isospin Breaking

The leading contribution to the isospin breaking from the valence quark masses is estimated at $\mathcal{O}((m_d - m_u)/\Lambda_{QCD}) \sim 0.5\%$, using $m_d - m_u = 2.38(18)$ MeV [172] and $\Lambda_{\text{QCD}} = 500$ MeV. Electromagnetic contributions are expected to be around $\mathcal{O}(\alpha_s) \sim 1/137 \approx 0.7\%$, which we take as the overall systematic due to isospin symmetry breaking.

6.5.10 Constructing the Synthetic Data Points

To construct the synthetic data points, we now sum all significant sources of systematic error in quadrature with the statistical error to build our final error budget at each reference q^2 value. We combine these errors with the correlation matrix of the data to obtain the corresponding covariance matrix. To construct the synthetic data points, we then draw 500 Monte-Carlo samples from a multivariate Gaussian distribution using this combined covariance matrix, centred on the reference q^2 values. The total error budget is plotted in figures 6.11 & 6.12, and given for each reference q^2 value in tables 6.8 & 6.9.

	$f_0^{B\to\pi}$			$f_+^{B\to\pi}$	
q^2 [GeV^2]	17.5	23.4	26.4	17.5	26.4
$f(q^2)$	0.505(22)	0.875(23)	1.260(34)	1.012(63)	8.65(30)
Statistics	4.4	2.7	2.9	6.2	3.5
Continuum Fit	3.0	2.9	3.4	5.7	4.0
RHQ	1.3	1.3	1.3	0.8	0.8
HQ	1.5	1.5	1.5	1.4	1.4
Renorm.	0.4	0.4	0.4	1.1	1.1
Imp.	0.1	0.1	0.1	0.3	0.3
IB	0.7	0.7	0.7	0.7	0.7
LQ	0.8	0.8	0.8	0.8	0.8
Total [%]	5.8	4.6	5.1	8.7	12.5

TABLE 6.9: Total error budget for the $B \to \pi\ell\nu$ synthetic data. Errors are given in %. We obtain the total error by adding all contributions in quadrature.

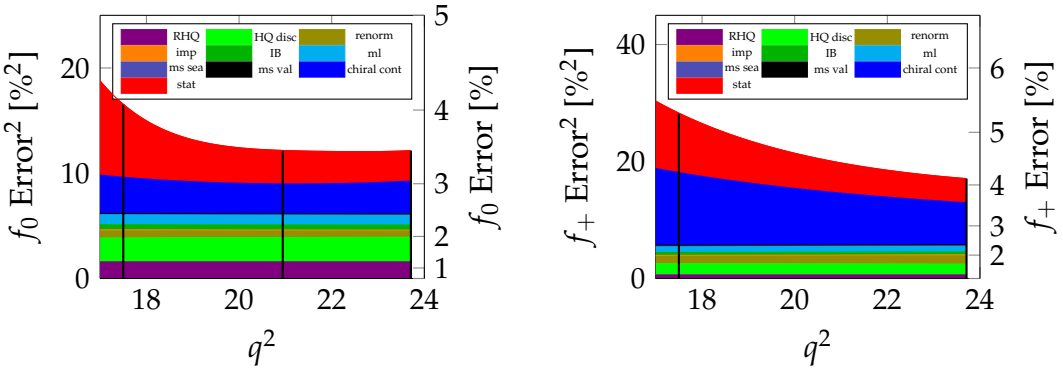

FIGURE 6.11: Total error budget for the $B_s \to K\ell\nu$ form factors. On the left is f_0, and the right is f_+. The synthetic data points are constructed using the total error given in this plot at each reference q^2 value.

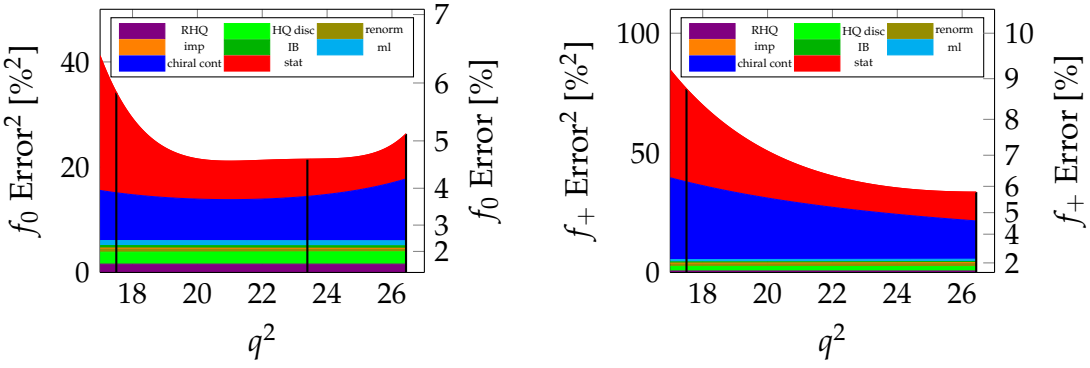

FIGURE 6.12: Total error budget for the $B \to \pi\ell\nu$ form factors. On the left is f_0, and the right is f_+. The synthetic data points are constructed using the total error given in this plot at each reference q^2 value.

	b_0^+	b_1^+	b_0^0	b_1^0	b_2^0	p
$B_s \to K\ell\nu$	0.332(17)	-1.34(12)	0.401(18)	-2.54(13)	4.35(68)	86%
$B \to \pi\ell\nu$	0.425(19)	-0.668(77)	0.651(25)	-1.884(83)	1.13(34)	40%

TABLE 6.10: The fitted coefficients of the z-expansions for the BCL fits, taking $K = 2$ for f_+ and $K = 3$ for f_0.

	b_0^+	b_1^+	b_0^0	b_1^0	b_2^0	p
$B_s \to K\ell\nu$	0.001365(69)	-0.00454(44)	0.00377(15)	-0.0110(13)	-0.0106(63)	22%
$B \to \pi\ell\nu$	0.00235(12)	-0.00146(41)	0.01223(43)	-0.0178(15)	-0.0021(61)	3%

TABLE 6.11: The fitted coefficients of the z-expansions for the BGL fits, taking $K = 2$ for f_+ and $K = 3$ for f_0.

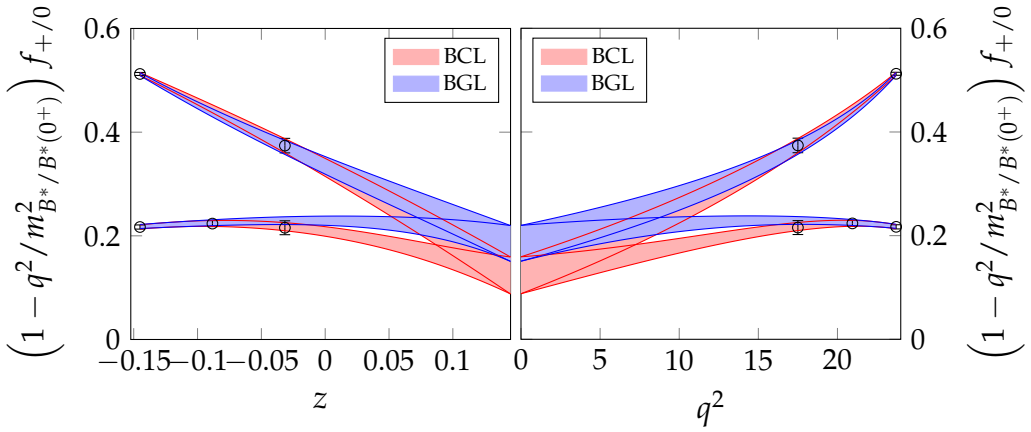

FIGURE 6.13: The extrapolation over the full q^2 range for $B_s \to K\ell\nu$ using the BCL and BGL fit forms.

6.6 z-expansion

Having built the synthetic data points, we can now use these in the z-expansion the extrapolate the results over the full q^2 range. In our z-expansions, we choose a number of independent terms equal to the number of synthetic data points entering the fit, and use the kinematic constraint that $f_0(0) = f_+(0)$. This is implemented by removing the b_0^0 parameter as a degree of freedom in the fit, and constructing it from the other fit parameters at each minimisation step such that the kinematic constraint is satisfied. The fitted coefficients are presented in tables 6.10 and 6.11, alongside the constructed b_0^0, and plots of the z-expansions are found in figures 6.13 and 6.14.

6.7 $|V_{ub}|$ and Lepton Universality Ratios

Having obtained a description of f_+ and f_0 over the full q^2 range, we can now obtain estimates for the standard model parameter $|V_{ub}|$, and for the lepton universality ratios R and R_{impr} introduced in section 4.2.3. Given our parameterisations of f_0 and

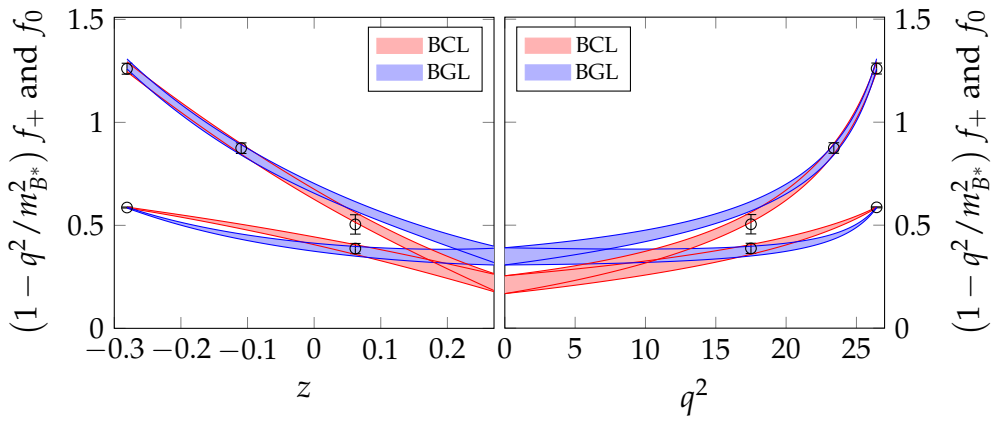

FIGURE 6.14: The extrapolation over the full q^2 range for $B \to \pi\ell\nu$ using the BCL and BGL fit forms.

f_+, we can use these in equation (4.1) to obtain theoretical predictions for the differential decay rates of $B_s \to K\ell\nu$ and $B \to \pi\ell\nu$, up to a factor of $|V_{ub}|^2$. Our prediction for the decay rates with final state μ and τ leptons, using the BCL parameterisation, is presented in figure 6.15.

As we noted in section 4.2.3, the lepton universality ratios are independent of $|V_{ub}|$ due to the cancellation of pre-factors that do not depend on q^2 in the decay rate integrals. We calculate predictions for both the standard ratio R and the "improved" ratio R_{impr} using the BCL parameterisation, and present the ratios in table 6.12. We also plot the unintegrated standard and improved ratios in figure 6.16.

As we see in table 6.12, the improved ratio has a substantially improved error over the standard ratio as expected, with an approximately ∼2.5 more precise error for both $B_s \to K\ell\nu$ and $B \to \pi\ell\nu$. If experimental results also show an improvement in precision using this method, this would suggest that the improved ratio may be a more powerful tool to monitor lepton universality violation — for $B_s \to K\ell\nu$ and $B \to \pi\ell\nu$ at least.

We obtain an error of 5.1% and 4.5% on the leading b_0^+ parameter in the BCL expansion for $B_s \to K\ell\nu$ and $B \to \pi\ell\nu$ respectively. The respective results of 0.332(17) and 0.425(19) are in excellent agreement with the previous determinations of these parameters in the 2015 analysis of 0.338(24) and 0.410(39) (see appendix A of [90] for z-parameterisation results), which by comparison have errors of 7.1% and 9.5%. We see that the addition of the F1S ensemble greatly benefits the $B \to \pi\ell\nu$ calculation, where the additional lattice spacing and closer-to-physical pion mass leads to a significantly more precise chiral continuum extrapolation.

Our b_0^+ coefficient has a similar uncertainty to the 5.0% error given by the 2019 Fermilab/MILC $B_s \to K\ell\nu$ fit [91], and our result for the lepton universality ratio $R_{\tau/\mu}$ of 0.837(59) also compares favourably with the Fermilab/MILC result of 0.836(34). We

	R	$R^{\text{impr.}}$
$B_s \to K\ell\nu$	0.837(59)	1.544(43)
$B \to \pi\ell\nu$	0.839(67)	1.631(59)

TABLE 6.12: Lepton universality ratios for the $B \to \pi\ell\nu$ and $B_s \to K\ell\nu$ processes. We present results for both the "standard" R-ratio, and the "improved" R-ratio, using the BCL parameterisation. The improved ratio shows substantially improved errors over the standard approach. It is as yet unclear whether such an improvement would also be visible in a similar ratio for experimental data.

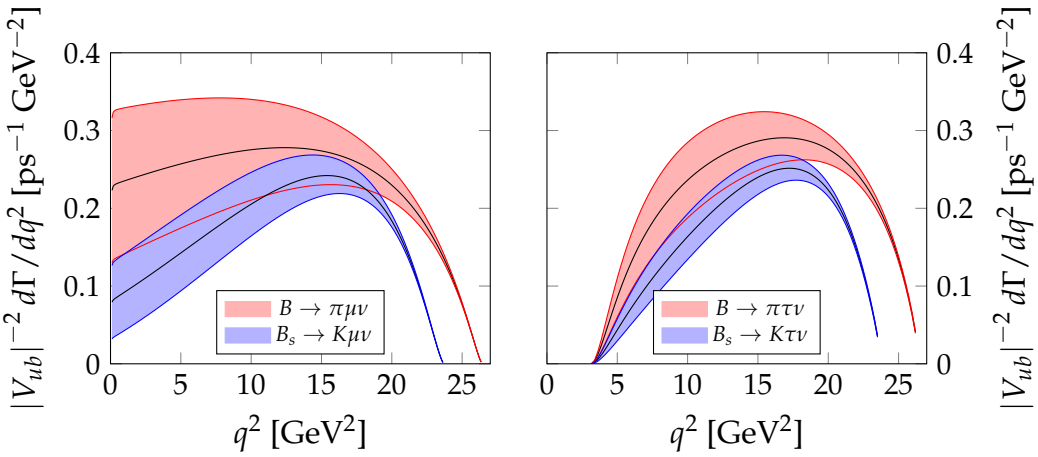

FIGURE 6.15: Standard Model predictions for the differential decay rate of $B_{(s)} \to P\ell\nu$ for the muon (left) and tau (right) final-state leptons, up to a factor of $|V_{ub}|^2$.

also compare favourably with the 2014 HPQCD result [89] for the b_0^+ parameter, which has an error of 5.7%, but are in tension with the R-ratio determination of 0.695(50). Our result for the $B \to \pi\ell\nu$ leading BCL coefficient also has a comparable error to the 2015 Fermilab/MILC analysis result of 3.9% [93].

The results of z-parameterisations across multiple independent calculations are assessed by the Flavour Lattice Averaging Group (FLAG), in order to form a global theoretical average for the form factor behaviour across q^2. These combined averages are then used to calculate $|V_{ub}|$ and lepton universality ratios in combination with experimental data. The current FLAG averages [78] include those of the RBC/UKQCD 2015 analysis [90] for $B_s \to K\ell\nu$ and $B \to \pi\ell\nu$, which this project will update in future publications. Given the substantial improvement in precision over the 2015 analysis, we anticipate that these results will lead to more precise FLAG averages of $|V_{ub}|$ and R, providing valuable input on CKM unitarity and the B-anomalies.

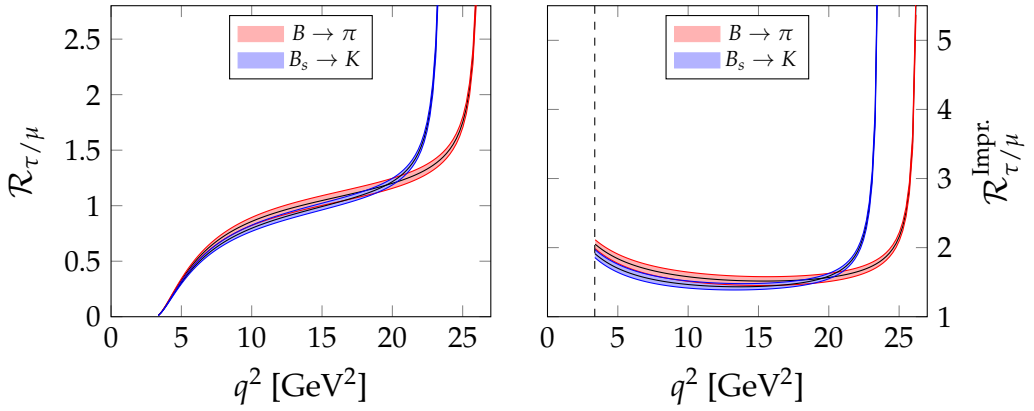

FIGURE 6.16: Standard Model ratio of the differential branching fraction $\mathcal{R}^{\tau/\mu}$ (left) and modified ratio $\mathcal{R}^{\tau/\mu}_{\text{Impr.}}$ (right). For the improved ratio, m_τ^2 is indicated with a vertical line.

Chapter 7

Conclusions

We have calculated standard model predictions of the form factors f_0 and f_+ for the semileptonic decays $B_s \to K\ell\nu$ and $B \to \pi\ell\nu$, using RHQ bottom quarks and DWF light & strange quarks. These calculations will provide future updates to the published 2015 RBC/UKQCD [90] determinations of these form factors.

We obtain an error of 5.1% and 4.5% on the most significant BCL z-expansion coefficient b_0^+ for $B_s \to K\ell\nu$ and $B \to \pi\ell\nu$ respectively. The corresponding 2015 RBC/UKQCD analysis for these decays found errors of 7.1% and 9.5%, highlighting the fact that the addition of the F1S ensemble provides a useful additional constraint on the continuum results, for $B \to \pi\ell\nu$ in particular. Our b_0^+ coefficient has a similar uncertainty to the 5.0% error given by the 2019 Fermilab/MILC $B_s \to K\ell\nu$ fit [91], and our result for the lepton universality ratio $R_{\tau/\mu}$ of 0.837(59) also compares favourably with the Fermilab/MILC result of 0.836(34). We also compare favourably with the 2014 HPQCD result [89] for the b_0^+ parameter, which has an error of 5.7%, but are in tension with the R-ratio determination of 0.695(50). Our result for the $B \to \pi\ell\nu$ leading BCL coefficient also has a comparable error to the 2015 Fermilab/MILC analysis result of 3.9% [93].

In addition to providing calculations of the standard lepton universality-testing ratios $R(\pi)$ & $R(K)$, we also demonstrate that the modified ratios $R_{\text{impr}}(\pi)$ & $R_{\text{impr}}(K)$—proposed in [155] and informed by [155–157]—offer more precise theoretical input on potential lepton flavour universality violation, with around a ~ 2.5 more precise error in our determination. If a similar improvement is also seen in ratios of experimental data, we propose that these ratios may provide a new, important check on lepton flavour universality.

The results calculated in this work provide independent theoretical checks on the form factors f_0 and f_+ for $B_s \to K\ell\nu$ and $B \to \pi\ell\nu$. Given the substantial improvement in precision over the 2015 analysis, we anticipate that these results will lead to more

precise FLAG averages of $|V_{ub}|$ and R from the $B_s \to K\ell\nu$ and $B \to \pi\ell\nu$ channels, providing valuable input on CKM unitarity, the B-anomalies, and the tension between exclusive $B \to \pi\ell\nu$ & inclusive $B \to X_u\ell\nu$ decays.

Appendix A

		n^2	$f_\parallel$	α	β	fit range	thinning	p value
C1	$f_\parallel$	0	1.175(13)	$-0.686(59)$	-1.57(38)	[4, 16]	1	36.89%
C1	$f_\parallel$	1	0.981(12)	$-0.409(35)$	-1.60(70)	[5, 17]	1	75.14%
C1	$f_\parallel$	2	0.854(17)	$-0.43(13)$	-1.36(78)	[5, 15]	1	54.77%
C1	$f_\parallel$	3	0.759(28)	$-0.273(85)$	-1.1(1.0)	[5, 18]	1	49.91%
C1	$f_\parallel$	4	0.725(48)	$-0.36(24)$	-1.6(1.6)	[5, 18]	1	84.88%
C2	$f_\parallel$	0	1.181(12)	$-0.676(75)$	-1.64(23)	[3, 16]	1	25.89%
C2	$f_\parallel$	1	1.001(12)	$-0.441(25)$	-1.75(22)	[3, 18]	1	41.23%
C2	$f_\parallel$	2	0.888(17)	$-0.339(28)$	-1.78(22)	[3, 18]	1	56.16%
C2	$f_\parallel$	3	0.813(27)	$-0.179(73)$	-1.76(25)	[3, 18]	1	58.44%
C2	$f_\parallel$	4	0.760(42)	$0.09(28)$	-1.7(1.8)	[5, 18]	1	56.98%
M1	$f_\parallel$	0	1.030(14)	$-3.0(1.7)$	-1.7(1.7)	[7, 18]	1	54.91%
M1	$f_\parallel$	1	0.861(15)	$-1.7(1.1)$	-3.9(3.3)	[8, 18]	1	46.25%
M1	$f_\parallel$	2	0.757(19)	$-0.46(12)$	2.8(6.8)	[9, 22]	1	88.14%
M1	$f_\parallel$	3	0.681(33)	$0.0(1.2)$	-6.0(10)	[9, 20]	1	69.73%
M1	$f_\parallel$	4	0.576(54)	$-0.4(1.2)$	1.0(17)	[9, 22]	1	26.71%
M2	$f_\parallel$	0	1.032(14)	$-0.68(25)$	-0.28(96)	[7, 18]	1	33.47%
M2	$f_\parallel$	1	0.853(12)	$-0.278(81)$	-1.36(56)	[6, 20]	1	60.85%
M2	$f_\parallel$	2	0.755(15)	$-0.213(44)$	-1.6(1.1)	[7, 22]	1	64.34%
M2	$f_\parallel$	3	0.667(23)	$-0.22(12)$	-1.6(1.4)	[7, 22]	1	55.64%
M2	$f_\parallel$	4	0.592(40)	$0.15(33)$	5.2(4.7)	[8, 22]	1	85.79%
M3	$f_\parallel$	0	1.063(25)	$-0.40(12)$	-1.0(1.3)	[7, 18]	1	50.12%
M3	$f_\parallel$	1	0.896(21)	$-0.254(66)$	-2.19(83)	[6, 20]	1	40.77%
M3	$f_\parallel$	2	0.774(22)	$-0.208(40)$	-2.3(1.4)	[7, 22]	1	26.79%
M3	$f_\parallel$	3	0.706(29)	$-0.00(10)$	-0.5(1.8)	[7, 22]	1	36.31%
M3	$f_\parallel$	4	0.633(60)	$-0.41(27)$	-4.7(6.2)	[8, 22]	1	27.53%
F1S	$f_\parallel$	0	0.927(11)	$-67.0(35)$	0.91(71)	[12, 19]	1	24.17%
F1S	$f_\parallel$	1	0.830(12)	$-150.0(110)$	-0.05(22)	[10, 17]	1	35.48%
F1S	$f_\parallel$	2	0.759(15)	$-110.0(100)$	-0.28(29)	[10, 17]	1	46.78%
F1S	$f_\parallel$	3	0.706(18)	$-4.7(3.8)$	-0.56(39)	[10, 21]	1	70.99%
F1S	$f_\parallel$	4	0.643(23)	$-2.4(5.8)$	-0.31(33)	[10, 21]	1	58.65%

TABLE A.1: Excited state form factor fits for $B_s \to K\ell\nu$ on all ensembles and momenta.

		n^2	$f_\perp$	α	β	fit range	thinning	p value
C1	$f_\perp$	1	1.493(22)	−1.183(91)	-2.82(71)	[4, 17]	1	7.64%
C1	$f_\perp$	2	1.157(22)	−0.70(11)	-2.58(63)	[4, 17]	1	5.40%
C1	$f_\perp$	3	0.924(31)	0.11(22)	-2.36(70)	[4, 17]	1	11.11%
C1	$f_\perp$	4	0.792(48)	−0.39(49)	-2.45(97)	[4, 17]	1	15.66%
C2	$f_\perp$	1	1.456(19)	−1.15(10)	-2.82(82)	[4, 17]	1	85.87%
C2	$f_\perp$	2	1.118(20)	−0.62(10)	-2.51(73)	[4, 17]	1	70.86%
C2	$f_\perp$	3	0.931(29)	−0.02(21)	-2.21(74)	[4, 17]	1	63.18%
C2	$f_\perp$	4	0.824(42)	−0.36(54)	-2.3(1.0)	[4, 17]	1	59.88%
M1	$f_\perp$	1	1.763(32)	−9.8(5.6)	-2.4(4.9)	[7, 18]	1	89.06%
M1	$f_\perp$	2	1.336(32)	−1.04(18)	-4.1(4.5)	[7, 23]	1	23.00%
M1	$f_\perp$	3	1.049(48)	−0.54(44)	-0.0(12)	[8, 23]	1	34.82%
M1	$f_\perp$	4	0.862(83)	−0.8(1.1)	-1.0(17)	[8, 23]	1	65.78%
M2	$f_\perp$	1	1.752(32)	−2.00(77)	-4.3(1.5)	[6, 18]	1	71.37%
M2	$f_\perp$	2	1.378(29)	−0.83(15)	-4.7(1.4)	[6, 22]	1	56.64%
M2	$f_\perp$	3	1.142(35)	−0.66(26)	-4.7(1.6)	[6, 22]	1	56.21%
M2	$f_\perp$	4	0.952(52)	−0.85(57)	-1.8(2.0)	[6, 22]	1	87.33%
M3	$f_\perp$	1	1.781(59)	−1.08(12)	-1.5(2.0)	[6, 22]	1	41.56%
M3	$f_\perp$	2	1.414(46)	−0.71(11)	-3.1(1.8)	[6, 22]	1	35.51%
M3	$f_\perp$	3	1.119(45)	−0.27(19)	-2.00(45)	[4, 22]	1	54.14%
M3	$f_\perp$	4	0.939(56)	−0.36(39)	-1.68(55)	[4, 22]	1	75.35%
F1S	$f_\perp$	1	2.128(37)	−840.0(610)	2.2(1.2)	[10, 17]	1	45.05%
F1S	$f_\perp$	2	1.719(31)	−300.0(360)	1.85(89)	[10, 17]	1	25.52%
F1S	$f_\perp$	3	1.482(37)	−160.0(440)	0.71(78)	[10, 17]	1	9.71%
F1S	$f_\perp$	4	1.343(51)	−170.0(550)	1.2(1.1)	[10, 17]	1	89.05%

TABLE A.2: Excited state form factor fits for $B_s \to K\ell\nu$ on all ensembles and momenta for $f_\perp$.

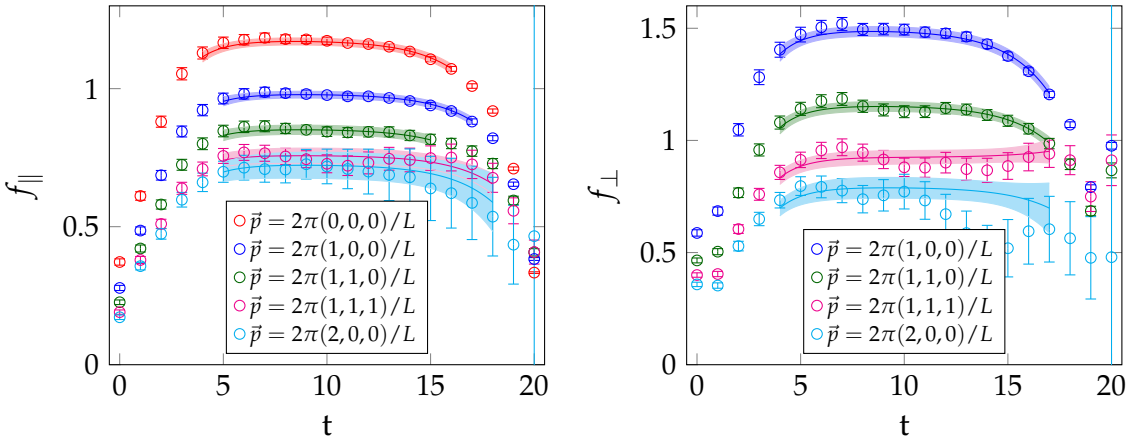

FIGURE A.1: Excited state form factor fits for $B_s \to K\ell\nu$ on the C1 ensemble.

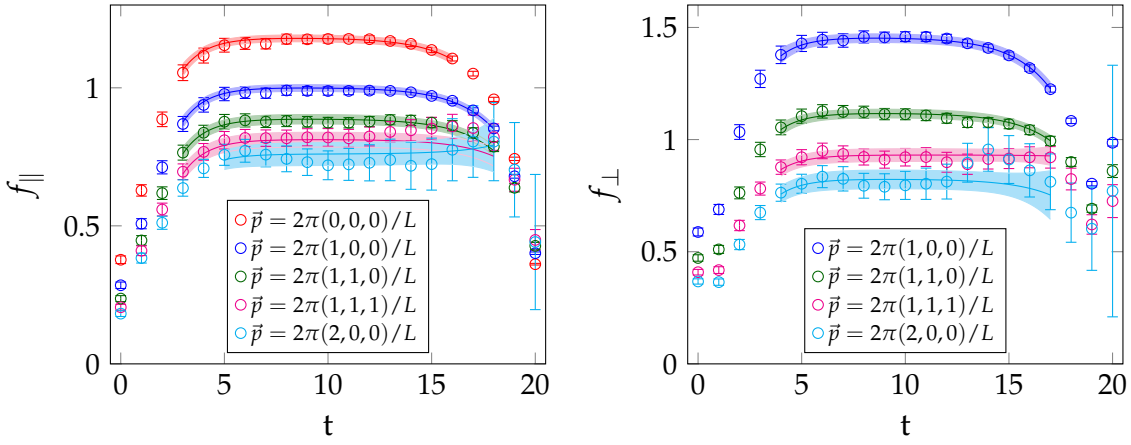

FIGURE A.2: Excited state form factor fits for $B_s \to K\ell\nu$ on the C2 ensemble.

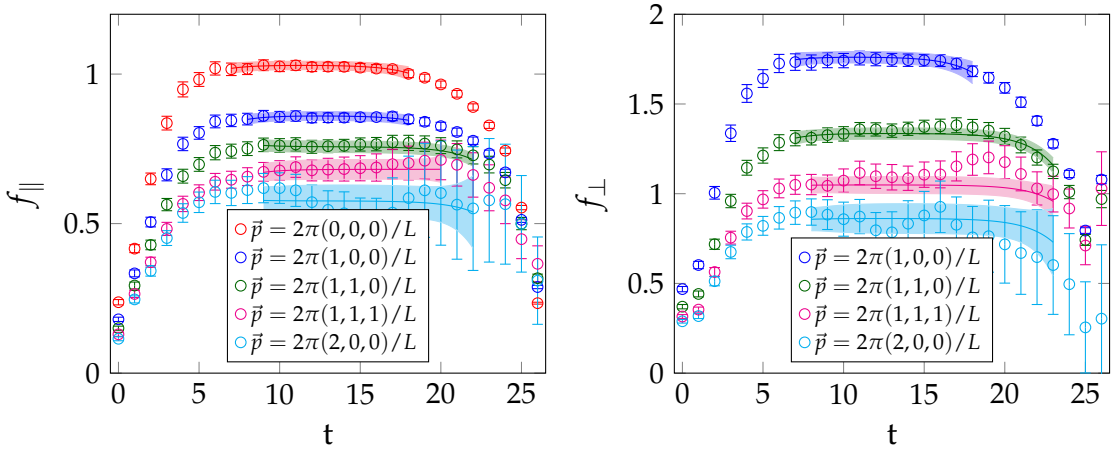

FIGURE A.3: Excited state form factor fits for $B_s \to K\ell\nu$ on the M1 ensemble.

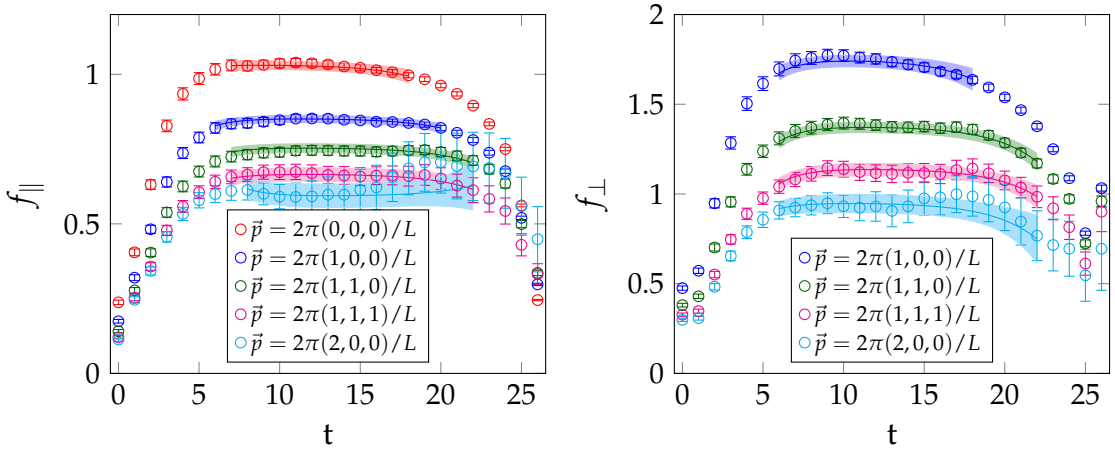

FIGURE A.4: Excited state form factor fits for $B_s \to K\ell\nu$ on the M2 ensemble.

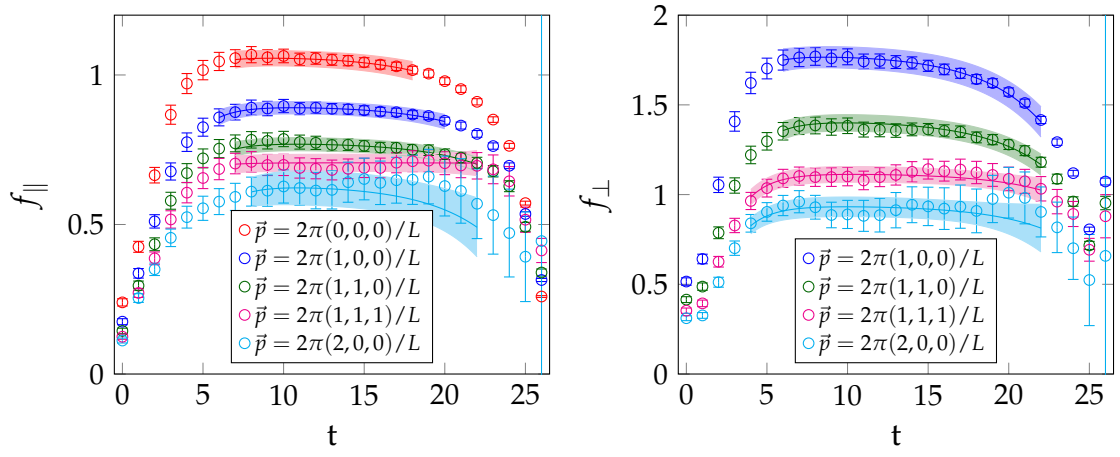

FIGURE A.5: Excited state form factor fits for $B_s \to K\ell\nu$ on the M3 ensemble.

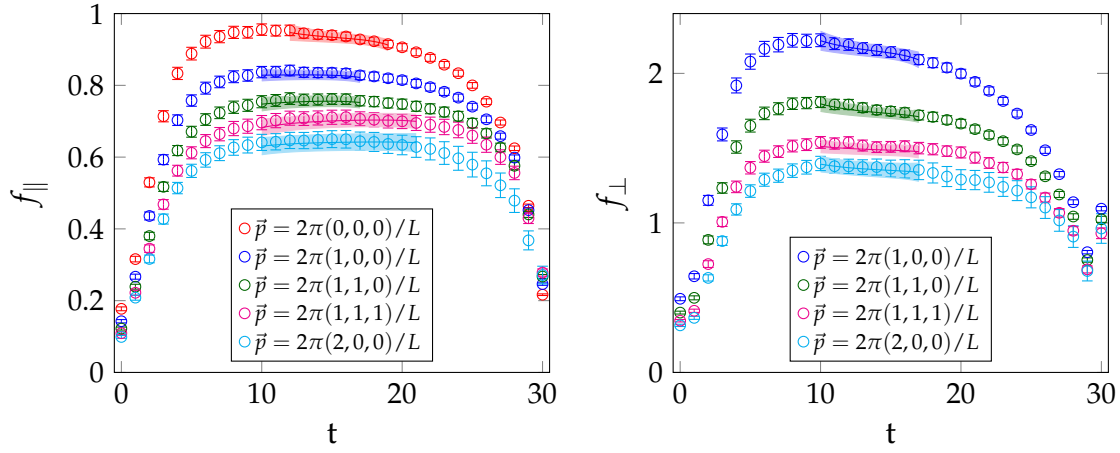

FIGURE A.6: Excited state form factor fits for $B_s \to K\ell\nu$ on the F1S ensemble.

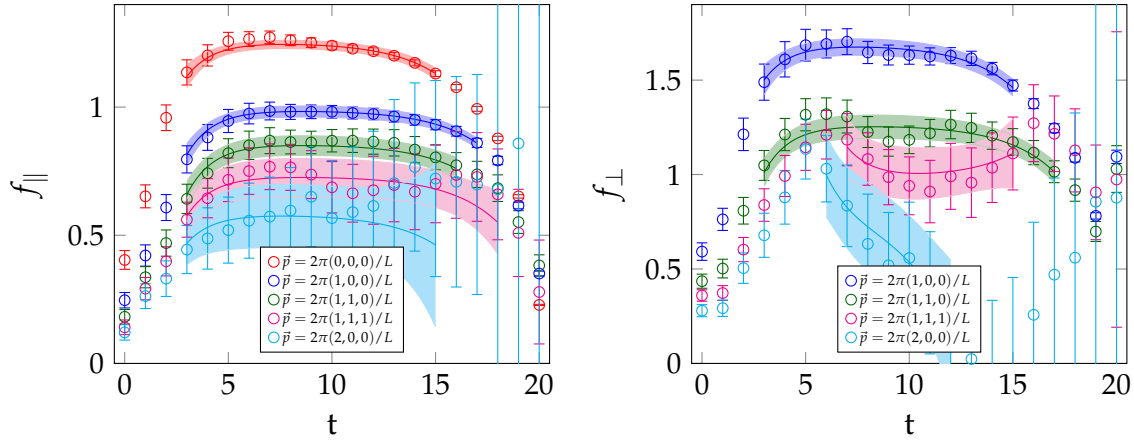

FIGURE A.7: Excited state form factor fits for $B \to \pi\ell\nu$ on the C1 ensemble.

		n^2	$f_\parallel$	α	β	fit range	thinning	p value
C1	$f_\parallel$	0	1.253(16)	−1.03(11)	-1.50(47)	[3, 15]	1	85.17%
C1	$f_\parallel$	1	0.988(22)	−0.464(40)	-1.97(46)	[3, 17]	1	97.50%
C1	$f_\parallel$	2	0.856(39)	−0.53(20)	-2.23(52)	[3, 16]	1	85.23%
C1	$f_\parallel$	3	0.730(75)	−0.42(30)	-1.75(60)	[3, 18]	1	78.03%
C1	$f_\parallel$	4	0.58(13)	−1.0(2.7)	-1.28(84)	[3, 15]	1	86.29%
C2	$f_\parallel$	0	1.205(17)	−1.40(46)	-1.71(21)	[2, 16]	1	7.69%
C2	$f_\parallel$	1	0.990(17)	−0.62(15)	-1.71(18)	[2, 17]	1	54.80%
C2	$f_\parallel$	2	0.878(29)	−0.54(27)	-1.69(18)	[2, 16]	1	20.11%
C2	$f_\parallel$	3	0.814(55)	1.6(1.0)	-2.02(53)	[3, 16]	1	61.09%
C2	$f_\parallel$	4	0.739(74)	2.5(3.4)	-2.00(71)	[3, 16]	1	93.82%
M1	$f_\parallel$	0	1.168(20)	−1.85(30)	-1.49(25)	[2, 18]	1	11.24%
M1	$f_\parallel$	1	0.915(30)	−0.88(18)	-2.04(46)	[3, 20]	1	25.39%
M1	$f_\parallel$	2	0.785(48)	−0.329(67)	-1.2(1.0)	[4, 24]	1	38.01%
M1	$f_\parallel$	3	0.565(95)	3.0(12)	-1.55(56)	[3, 15]	1	69.68%
M1	$f_\parallel$	4	0.70(18)	2.0(26)	-2.3(1.0)	[3, 15]	1	59.38%
M2	$f_\parallel$	0	1.130(18)	−3.00(85)	-1.5(1.0)	[5, 15]	1	48.21%
M2	$f_\parallel$	1	0.862(24)	−2.0(1.0)	-2.0(1.1)	[5, 15]	1	75.60%
M2	$f_\parallel$	2	0.751(28)	−0.265(59)	-1.70(31)	[3, 23]	1	45.77%
M2	$f_\parallel$	3	0.672(52)	−0.53(64)	-1.47(31)	[3, 21]	1	26.49%
M2	$f_\parallel$	4	0.51(21)	12.0(13)	140.0(150)	[10, 15]	1	60.02%
M3	$f_\parallel$	0	1.075(15)	−1.49(27)	-1.16(57)	[4, 18]	1	63.71%
M3	$f_\parallel$	1	0.868(18)	−0.57(13)	-1.61(52)	[4, 20]	1	52.53%
M3	$f_\parallel$	2	0.726(28)	−0.50(26)	-1.59(51)	[4, 20]	1	33.17%
M3	$f_\parallel$	3	0.673(48)	−0.43(10)	-1.52(30)	[3, 25]	1	67.58%
M3	$f_\parallel$	4	0.505(90)	−0.1(1.0)	-0.94(41)	[3, 22]	1	80.73%
F1S	$f_\parallel$	0	1.075(27)	−6.7(2.5)	0.38(67)	[8, 15]	1	28.25%
F1S	$f_\parallel$	1	0.889(27)	−3.01(96)	-0.88(17)	[3, 17]	1	19.87%
F1S	$f_\parallel$	2	0.779(36)	−2.3(1.4)	-0.71(26)	[4, 17]	1	69.81%
F1S	$f_\parallel$	3	0.723(46)	0.92(67)	-0.88(17)	[3, 20]	1	59.64%
F1S	$f_\parallel$	4	0.67(10)	−8.4(6.4)	-0.35(95)	[7, 16]	1	75.85%

TABLE A.3: Excited state form factor fits for $B \to \pi\ell\nu$ on all ensembles and momenta for $f_\parallel$.

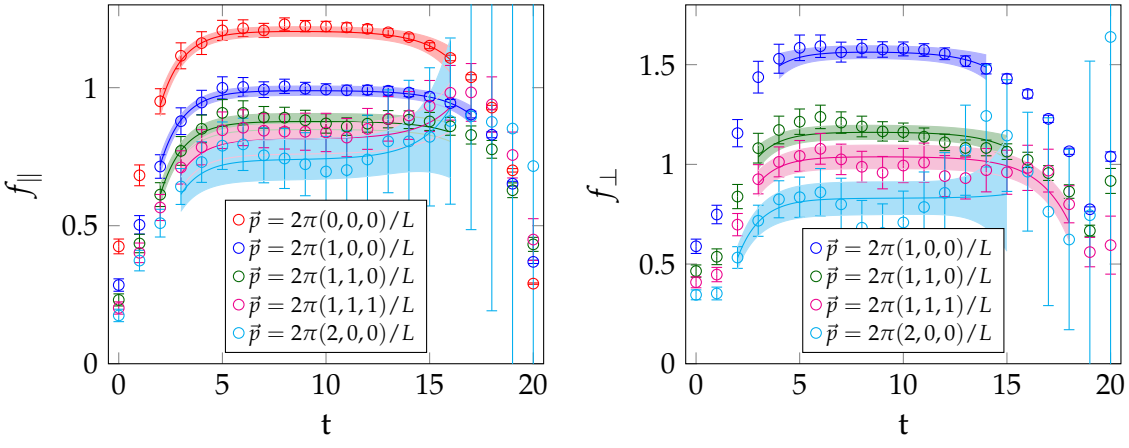

FIGURE A.8: Excited state form factor fits for $B \to \pi\ell\nu$ on the C2 ensemble.

		n^2	$f_\perp$	α	β	fit range	thinning	p value
C1	$f_\perp$	1	1.689(44)	−1.93(34)	-2.12(81)	[3, 15]	1	42.56%
C1	$f_\perp$	2	1.263(63)	−0.90(25)	-2.83(82)	[3, 17]	1	36.10%
C1	$f_\perp$	3	0.98(15)	1.1(1.8)	47.0(44)	[7, 15]	1	32.69%
C1	$f_\perp$	4	0.78(30)	−18.0(13)	34.0(34)	[6, 12]	1	63.43%
C2	$f_\perp$	1	1.566(32)	−3.9(2.4)	-2.9(2.1)	[4, 14]	1	48.61%
C2	$f_\perp$	2	1.162(35)	−2.0(1.3)	-2.01(72)	[3, 15]	1	59.52%
C2	$f_\perp$	3	1.039(59)	−1.22(32)	-2.16(84)	[3, 18]	1	41.32%
C2	$f_\perp$	4	0.830(83)	0.5(7.4)	-1.90(34)	[2, 15]	1	40.49%
M1	$f_\perp$	1	2.056(78)	−4.4(1.4)	-1.8(2.3)	[4, 18]	1	75.59%
M1	$f_\perp$	2	1.45(11)	−1.8(1.2)	-8.9(4.5)	[5, 20]	1	65.52%
M1	$f_\perp$	3	1.22(25)	−31.0(25)	-13.8(6.5)	[5, 15]	1	87.74%
M1	$f_\perp$	4	0.83(53)	48.0(58)	70.0(120)	[8, 15]	1	21.61%
M2	$f_\perp$	1	2.001(60)	−7.8(2.2)	-3.5(1.3)	[4, 16]	1	45.36%
M2	$f_\perp$	2	1.554(69)	−2.97(92)	-2.7(1.1)	[4, 19]	1	92.81%
M2	$f_\perp$	3	1.206(98)	−1.0(1.1)	-2.1(1.3)	[4, 22]	1	93.77%
M2	$f_\perp$	4	0.82(18)	11.0(11)	0.3(4.2)	[5, 17]	1	84.76%
M3	$f_\perp$	1	1.921(47)	−8.1(2.8)	-2.5(1.2)	[4, 16]	1	55.89%
M3	$f_\perp$	2	1.502(61)	−3.7(1.7)	-3.5(1.1)	[4, 18]	1	74.72%
M3	$f_\perp$	3	1.076(83)	−0.3(1.5)	-1.75(23)	[2, 20]	1	79.65%
M3	$f_\perp$	4	0.99(13)	−4.4(4.0)	-2.77(74)	[3, 20]	1	88.71%
F1S	$f_\perp$	1	2.730(89)	−17.6(5.8)	3.9(5.1)	[9, 17]	1	70.07%
F1S	$f_\perp$	2	1.992(64)	−5.7(1.1)	4.1(4.0)	[8, 21]	1	58.21%
F1S	$f_\perp$	3	1.721(96)	−2.8(1.1)	-1.0(1.3)	[6, 22]	1	41.29%
F1S	$f_\perp$	4	1.41(16)	−1.0(1.3)	3.7(4.5)	[8, 25]	1	34.14%

TABLE A.4: Excited state form factor fits for $B \to \pi\ell\nu$ on all ensembles and momenta for $f_\perp$.

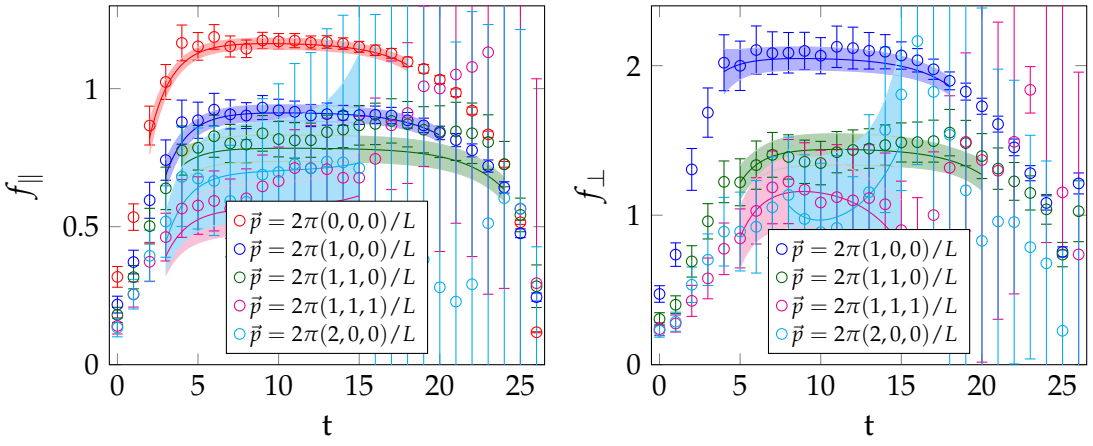

FIGURE A.9: Excited state form factor fits for $B \to \pi\ell\nu$ on the M1 ensemble.

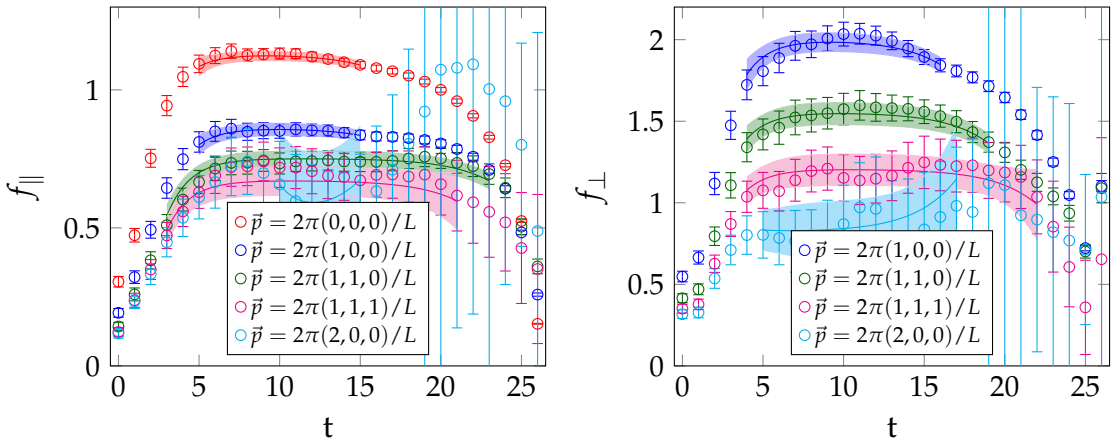

FIGURE A.10: Excited state form factor fits for $B \to \pi\ell\nu$ on the M2 ensemble.

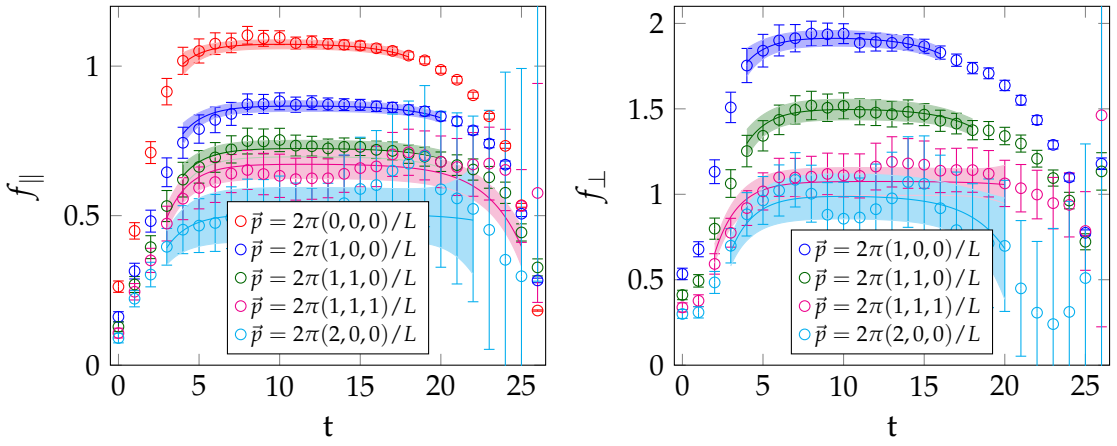

FIGURE A.11: Excited state form factor fits for $B \to \pi\ell\nu$ on the M3 ensemble.

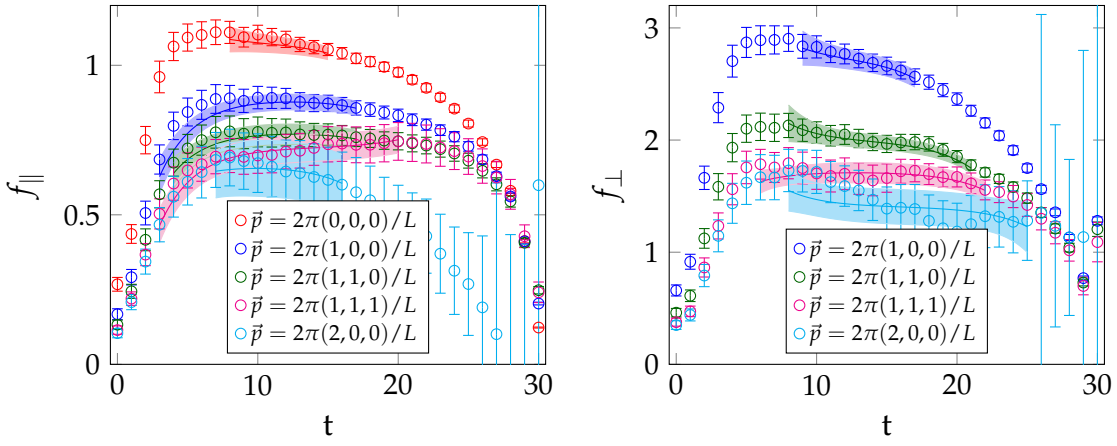

FIGURE A.12: Excited state form factor fits for $B \to \pi\ell\nu$ on the F1S ensemble.

	Variation	C1	C2	C3	C4	C5	p
$f_0^{Bs\to K}$	Preferred Fit	0.529(30)	0.22(11)	0.378(91)	-0.252(69)	0.024(58)	73.81%
$f_0^{Bs\to K}$	Standard Fit	0.529(30)	0.22(11)	0.378(91)	-0.252(69)	0.024(58)	73.81%
$f_0^{Bs\to K}$	No FV	0.535(30)	0.35(11)	0.368(92)	-0.245(69)	-0.068(58)	85.43%
$f_0^{Bs\to K}$	Remove smallest momentum	0.539(33)	0.21(12)	0.35(10)	-0.233(77)	0.025(58)	59.34%
$f_0^{Bs\to K}$	Remove largest momentum	0.539(33)	0.21(12)	0.35(10)	-0.233(77)	0.025(58)	59.34%
$f_0^{Bs\to K}$	Analytic	0.543(31)	0.51(11)	0.371(92)	-0.247(69)	-0.063(58)	82.94%
$f_0^{Bs\to K}$	No M_π^2	0.536(30)	-	0.377(91)	-0.250(69)	0.097(45)	58.57%
$f_0^{Bs\to K}$	No a^2	0.531(30)	0.252(90)	0.381(91)	-0.254(68)	-	77.60%
$f_0^{Bs\to K}$	Varying f_π	0.524(30)	0.13(12)	0.382(91)	-0.254(69)	0.053(58)	69.82%
$f_0^{Bs\to K}$	Varying f_π	0.533(30)	0.31(11)	0.376(91)	-0.250(69)	-0.002(58)	76.90%
$f_0^{Bs\to K}$	Varying Δ	0.385(27)	0.24(10)	0.522(83)	-0.300(63)	0.007(51)	75.48%
$f_0^{Bs\to K}$	Varying Δ	0.674(33)	0.20(13)	0.24(10)	-0.205(75)	0.040(65)	72.28%
$f_+^{Bs\to K}$	Preferred Fit	1.782(39)	-0.03(28)	-0.717(39)	-	0.07(14)	24.39%
$f_+^{Bs\to K}$	Standard Fit	1.89(15)	-0.08(29)	-0.99(37)	0.17(22)	0.10(15)	21.87%
$f_+^{Bs\to K}$	No FV	1.792(39)	0.43(28)	-0.723(39)	-	-0.23(14)	43.28%
$f_+^{Bs\to K}$	Remove smallest momentum	1.782(39)	-0.03(28)	-0.717(39)	-	0.07(14)	24.39%
$f_+^{Bs\to K}$	Remove largest momentum	1.788(41)	-0.02(28)	-0.725(44)	-	0.07(14)	13.40%
$f_+^{Bs\to K}$	Analytic	1.822(40)	0.93(27)	-0.721(39)	-	-0.21(14)	37.20%
$f_+^{Bs\to K}$	No M_π^2	1.781(38)	-	-0.717(39)	-	0.07(11)	29.44%
$f_+^{Bs\to K}$	No a^2	1.789(36)	0.06(22)	-0.717(39)	-	-	28.20%
$f_+^{Bs\to K}$	Varying f_π	1.768(38)	-0.35(28)	-0.715(39)	-	0.17(14)	20.05%
$f_+^{Bs\to K}$	Varying f_π	1.794(39)	0.26(28)	-0.718(39)	-	-0.01(14)	28.25%
$f_+^{Bs\to K}$	Varying Δ	1.655(37)	0.01(27)	-0.620(38)	-	0.07(14)	29.48%
$f_+^{Bs\to K}$	Varying Δ	1.908(40)	-0.06(29)	-0.813(41)	-	0.08(15)	18.36%

TABLE A.5: Fit coefficients for chiral continuum fits on $B_s \to K\ell\nu$ for all fit variations with acceptable p-values.

	Variation	C1	C2	C3	C4	C5	p
$f_0^{B\to Pi}$	Preferred Fit	0.501(24)	-0.09(12)	0.46(11)	-0.31(11)	-0.030(56)	86.74%
$f_0^{B\to Pi}$	Standard Fit	0.501(24)	-0.09(12)	0.46(11)	-0.31(11)	-0.030(56)	86.74%
$f_0^{B\to Pi}$	No FV	0.502(25)	0.11(12)	0.45(11)	-0.30(11)	-0.171(58)	87.46%
$f_0^{B\to Pi}$	Remove smallest momentum	0.507(26)	-0.11(12)	0.44(12)	-0.29(12)	-0.033(57)	76.31%
$f_0^{B\to Pi}$	Remove largest momentum	0.507(26)	-0.11(12)	0.44(12)	-0.29(12)	-0.033(57)	76.31%
$f_0^{B\to Pi}$	Analytic	0.521(25)	0.39(12)	0.45(11)	-0.31(11)	-0.166(57)	84.52%
$f_0^{B\to Pi}$	No M_π^2	0.498(24)	-	0.44(11)	-0.30(11)	-0.042(54)	87.88%
$f_0^{B\to Pi}$	No a^2	0.498(24)	-0.11(12)	0.45(11)	-0.30(11)	-	88.76%
$f_0^{B\to Pi}$	Varying f_π	0.494(24)	-0.26(12)	0.46(11)	-0.31(11)	0.016(55)	85.82%
$f_0^{B\to Pi}$	Varying f_π	0.507(25)	0.05(12)	0.45(11)	-0.31(11)	-0.070(56)	86.86%
$f_0^{B\to Pi}$	Varying g_b	0.504(25)	-0.03(12)	0.46(11)	-0.31(11)	-0.047(56)	86.86%
$f_0^{B\to Pi}$	Varying g_b	0.498(24)	-0.16(12)	0.46(11)	-0.31(11)	-0.011(56)	86.46%
$f_0^{B\to Pi}$	Varying Δ	0.363(21)	-0.00(10)	0.603(97)	-0.368(97)	-0.042(47)	85.95%
$f_0^{B\to Pi}$	Varying Δ	0.640(28)	-0.18(14)	0.31(12)	-0.25(12)	-0.018(64)	87.06%
$f_+^{B\to Pi}$	Preferred Fit	1.673(62)	-0.39(40)	-0.642(87)	-	0.10(20)	57.75%
$f_+^{B\to Pi}$	Standard Fit	1.61(19)	-0.36(41)	-0.42(59)	-0.16(42)	0.08(21)	52.11%
$f_+^{B\to Pi}$	No FV	1.678(62)	0.26(39)	-0.650(87)	-	-0.34(21)	78.96%
$f_+^{B\to Pi}$	Remove smallest momentum	1.673(62)	-0.39(40)	-0.642(87)	-	0.10(20)	57.75%
$f_+^{B\to Pi}$	Remove largest momentum	1.663(66)	-0.39(40)	-0.623(97)	-	0.09(20)	28.57%
$f_+^{B\to Pi}$	Analytic	1.738(64)	1.21(38)	-0.647(87)	-	-0.33(21)	74.17%
$f_+^{B\to Pi}$	No M_π^2	1.655(60)	-	-0.652(86)	-	0.01(18)	58.10%
$f_+^{B\to Pi}$	No a^2	1.684(58)	-0.30(35)	-0.642(87)	-	-	62.47%
$f_+^{B\to Pi}$	Varying f_π	1.651(61)	-0.93(40)	-0.640(87)	-	0.24(20)	49.24%
$f_+^{B\to Pi}$	Varying f_π	1.693(63)	0.08(39)	-0.644(87)	-	-0.03(20)	64.03%
$f_+^{B\to Pi}$	Varying g_b	1.682(62)	-0.19(39)	-0.643(87)	-	0.05(20)	60.55%
$f_+^{B\to Pi}$	Varying g_b	1.664(62)	-0.62(40)	-0.641(87)	-	0.16(20)	54.32%
$f_+^{B\to Pi}$	Varying Δ	1.630(61)	-0.36(39)	-0.606(86)	-	0.10(20)	57.84%
$f_+^{B\to Pi}$	Varying Δ	1.716(63)	-0.42(40)	-0.679(88)	-	0.10(20)	57.49%

TABLE A.6: Fit coefficients for chiral continuum fits on $B \to \pi\ell\nu$ for all fit variations with acceptable p-values.

References

[1] J. M. Flynn et al. *Semi-leptonic form factors for $B_s \to K\ell\nu$ and $B_s \to D_s\ell\nu$*. 2019. arXiv: 1903.02100 [hep-lat].

[2] J. Flynn et al. *Semileptonic $B \to \pi\ell\nu$, $B \to D\ell\nu$, $B_s \to K\ell\nu$, and $B_s \to D_s\ell\nu$ decays*. 2019. arXiv: 1912.09946 [hep-lat].

[3] J. M. Flynn et al. *Nonperturbative calculations of form factors for exclusive semileptonic $B_{(s)}$ decays*. 2020. arXiv: 2012.04323 [hep-ph].

[4] P. Zyla et al. "Review of Particle Physics". In: *PTEP* 2020.8 (2020), p. 083C01. DOI: 10.1093/ptep/ptaa104.

[5] M. A. Shifman, A. I. Vainshtein, and V. I. Zakharov. In: *Nucl. Phys. B* 147.385 (1979), p. 448.

[6] Y. Amhis et al. "Averages of b-hadron, c-hadron, and τ-lepton properties as of 2018". In: *The European Physical Journal C* 81.3 (2021). ISSN: 1434-6052. DOI: 10.1140/epjc/s10052-020-8156-7. URL: http://dx.doi.org/10.1140/epjc/s10052-020-8156-7.

[7] K. G. Wilson. "Confinement of Quarks". In: *Phys. Rev.* D10 (1974), pp. 2445–2459.

[8] E. Follana et al. "Highly improved staggered quarks on the lattice with applications to charm physics". In: *Physical Review D* 75.5 (2007). ISSN: 1550-2368. DOI: 10.1103/physrevd.75.054502. URL: http://dx.doi.org/10.1103/PhysRevD.75.054502.

[9] A. X. El-Khadra, A. S. Kronfeld, and P. B. Mackenzie. "Massive fermions in lattice gauge theory". In: *Physical Review D* 55.7 (1997), 3933–3957. ISSN: 1089-4918. DOI: 10.1103/physrevd.55.3933. URL: http://dx.doi.org/10.1103/PhysRevD.55.3933.

[10] S. Aoki, Y. Kuramashi, and S. Tominaga. "Relativistic Heavy Quarks on the Lattice". In: *Progress of Theoretical Physics* 109.3 (2003), 383–414. ISSN: 1347-4081. DOI: 10.1143/ptp.109.383. URL: http://dx.doi.org/10.1143/PTP.109.383.

[11] N. H. Christ, M. Li, and H. Lin. "Relativistic heavy quark effective action". In: *Physical Review D* 76.7 (2007). ISSN: 1550-2368. DOI: 10.1103/physrevd.76.074505. URL: http://dx.doi.org/10.1103/PhysRevD.76.074505.

[12] D. B. Kaplan. "A method for simulating chiral fermions on the lattice". In: *Physics Letters B* 288.3-4 (1992), 342–347. ISSN: 0370-2693. DOI: 10.1016/0370-2693(92)91112-m. URL: http://dx.doi.org/10.1016/0370-2693(92)91112-M.

[13] Y. Shamir. "Chiral fermions from lattice boundaries". In: *Nuclear Physics B* 406.1 (1993), pp. 90–106. ISSN: 0550-3213. DOI: https://doi.org/10.1016/0550-3213(93)90162-I.

[14] V. Furman and Y. Shamir. "Axial symmetries in lattice QCD with Kaplan fermions". In: *Nuclear Physics B* 439.1 (1995), pp. 54–78. ISSN: 0550-3213. DOI: https://doi.org/10.1016/0550-3213(95)00031-M.

[15] T. Blum and A. Soni. "QCD with domain wall quarks". In: *Physical Review D* 56.1 (1997), 174–178. ISSN: 1089-4918. DOI: 10.1103/physrevd.56.174. URL: http://dx.doi.org/10.1103/PhysRevD.56.174.

[16] T. Blum and A. Soni. "Domain Wall Quarks and Kaon Weak Matrix Elements". In: *Physical Review Letters* 79.19 (1997), 3595–3598. ISSN: 1079-7114. DOI: 10.1103/physrevlett.79.3595. URL: http://dx.doi.org/10.1103/PhysRevLett.79.3595.

[17] T. Aoyama, T. Kinoshita, and M. Nio. "Revised and improved value of the QED tenth-order electron anomalous magnetic moment". In: *Physical Review D* 97.3 (2018). ISSN: 2470-0029. DOI: 10.1103/physrevd.97.036001. URL: http://dx.doi.org/10.1103/PhysRevD.97.036001.

[18] B. J. Bjørken and S. L. Glashow. "Elementary particles and SU(4)". In: *Physics Letters* 11.3 (Aug. 1964), pp. 255–257. DOI: 10.1016/0031-9163(64)90433-0.

[19] J. E. Augustin et al. "Discovery of a Narrow Resonance in e^+e^- Annihilation". In: *Physical Review Letters* 33.23 (Dec. 1974), pp. 1406–1408. DOI: 10.1103/PhysRevLett.33.1406.

[20] J. J. Aubert et al. "Experimental Observation of a Heavy Particle J". In: *Physical Review Letters* 33.23 (Dec. 1974), pp. 1404–1406. DOI: 10.1103/PhysRevLett.33.1404.

[21] N. Cabibbo. "Unitary Symmetry and Leptonic Decays". In: *Physical Review Letters* 10.12 (June 1963), pp. 531–533. DOI: 10.1103/PhysRevLett.10.531.

[22] M. Kobayashi and T. Maskawa. "CP-Violation in the Renormalizable Theory of Weak Interaction". In: *Progress of Theoretical Physics* 49.2 (Feb. 1973), pp. 652–657. DOI: 10.1143/PTP.49.652.

[23] S. W. Herb et al. "Observation of a Dimuon Resonance at 9.5 GeV in 400-GeV Proton-Nucleus Collisions". In: *Physical Review Letters* 39.5 (Aug. 1977), pp. 252–255. DOI: 10.1103/PhysRevLett.39.252.

[24] F. Abe et al. "Observation of Top Quark Production in $p\bar{p}$ Collisions with the Collider Detector at Fermilab". In: *Physical Review Letters* 74.14 (Apr. 1995), pp. 2626–2631. DOI: 10.1103/PhysRevLett.74.2626. arXiv: hep-ex/9503002 [hep-ex].

[25] S. Abachi et al. "Observation of the Top Quark". In: *Physical Review Letters* 74.14 (Apr. 1995), pp. 2632–2637. DOI: 10.1103/PhysRevLett.74.2632. arXiv: hep-ex/9503003 [hep-ex].

[26] S. Weinberg. "A Model of Leptons". In: *Physical Review Letters* 19.21 (Nov. 1967), pp. 1264–1266. DOI: 10.1103/PhysRevLett.19.1264.

[27] G. Arnison et al. "Experimental observation of isolated large transverse energy electrons with associated missing energy at s=540 GeV". In: *Physics Letters B* 122.1 (1983), pp. 103–116. ISSN: 0370-2693. DOI: https://doi.org/10.1016/0370-2693(83)91177-2. URL: https://www.sciencedirect.com/science/article/pii/0370269383911772.

[28] G. Arnison et al. "Experimental observation of lepton pairs of invariant mass around 95 GeV/c2 at the CERN SPS collider". In: *Physics Letters B* 126.5 (1983), pp. 398–410. ISSN: 0370-2693. DOI: https://doi.org/10.1016/0370-2693(83)90188-0. URL: https://www.sciencedirect.com/science/article/pii/0370269383901880.

[29] K. Kodama et al. "Observation of tau neutrino interactions". In: *Physics Letters B* 504.3 (2001), 218–224. ISSN: 0370-2693. DOI: 10.1016/s0370-2693(01)00307-0. URL: http://dx.doi.org/10.1016/S0370-2693(01)00307-0.

[30] G. Aad et al. "Observation of a new particle in the search for the Standard Model Higgs boson with the ATLAS detector at the LHC". In: *Physics Letters B* 716.1 (2012), 1–29. ISSN: 0370-2693. DOI: 10.1016/j.physletb.2012.08.020. URL: http://dx.doi.org/10.1016/j.physletb.2012.08.020.

[31] S. Chatrchyan et al. "Observation of a new boson at a mass of 125 GeV with the CMS experiment at the LHC". In: *Physics Letters B* 716.1 (2012), 30–61. ISSN: 0370-2693. DOI: 10.1016/j.physletb.2012.08.021. URL: http://dx.doi.org/10.1016/j.physletb.2012.08.021.

[32] B. Abi et al. "Measurement of the Positive Muon Anomalous Magnetic Moment to 0.46 ppm". In: *Phys. Rev. Lett.* 126 (14 2021), p. 141801. DOI: 10.1103/PhysRevLett.126.141801. URL: https://link.aps.org/doi/10.1103/PhysRevLett.126.141801.

[33] S. Borsanyi et al. "Leading hadronic contribution to the muon magnetic moment from lattice QCD". In: *Nature* 593.7857 (2021), 51–55. ISSN: 1476-4687. DOI: 10.1038/s41586-021-03418-1. URL: http://dx.doi.org/10.1038/s41586-021-03418-1.

[34] J. P. Lees et al. "Evidence for an Excess of $\overline{B} \to D^{(*)}\tau^-\overline{\nu}_\tau$". In: *Physical Review Letters* 109.10 (2012). ISSN: 1079-7114. DOI: 10.1103/physrevlett.109.101802. URL: http://dx.doi.org/10.1103/PhysRevLett.109.101802.

[35] M. Huschle et al. "Measurement of the branching ratio of $\overline{B} \to D^{(*)}\tau^-\overline{\nu}_\tau$ relative to $\overline{B} \to D^{(*)}\ell^-\overline{\nu}_\ell$ decays with hadronic tagging at Belle". In: *Physical Review D* 92.7 (2015). ISSN: 1550-2368. DOI: 10.1103/physrevd.92.072014. URL: http://dx.doi.org/10.1103/PhysRevD.92.072014.

[36] G. Caria et al. "Measurement of $R(D)$ and $R(D^*)$ with a Semileptonic Tagging Method". In: *Physical Review Letters* 124.16 (2020). ISSN: 1079-7114. DOI: 10.1103/physrevlett.124.161803. URL: http://dx.doi.org/10.1103/PhysRevLett.124.161803.

[37] S. Hirose et al. "Measurement of the τ Lepton Polarization and $R(D^*)$ in the Decay $\overline{B} \to D^*\tau^-\overline{\nu}_\tau$". In: *Physical Review Letters* 118.21 (2017). ISSN: 1079-7114. DOI: 10.1103/physrevlett.118.211801. URL: http://dx.doi.org/10.1103/PhysRevLett.118.211801.

[38] R. Aaij et al. "Measurement of the Ratio of Branching Fractions $\mathcal{B}(\overline{B}^0 \to D^{*+}\tau^-\overline{\nu}_\tau)/\mathcal{B}(\overline{B}^0 \to D^{*+}\nu^-\overline{\nu}_\mu)$". In: *Physical Review Letters* 115.11 (2015). ISSN: 1079-7114. DOI: 10.1103/physrevlett.115.111803. URL: http://dx.doi.org/10.1103/PhysRevLett.115.111803.

[39] R. Aaij et al. "Measurement of the Ratio of the $B^0 \to D^*\tau^+\nu_\tau$ and $B^0 \to D^*\mu^+\nu_\mu$ Branching Fractions Using Three-Prong τ -Lepton Decays". In: *Physical Review Letters* 120.17 (2018). ISSN: 1079-7114. DOI: 10.1103/physrevlett.120.171802. URL: http://dx.doi.org/10.1103/PhysRevLett.120.171802.

[40] J. P. Lees et al. "Measurement of an excess of $\overline{B} \to D^{(*)}\tau^-\overline{\nu}_\tau$ decays and implications for charged Higgs bosons". In: *Physical Review D* 88.7 (2013). ISSN: 1550-2368. DOI: 10.1103/physrevd.88.072012. URL: http://dx.doi.org/10.1103/PhysRevD.88.072012.

[41] R. Aaij et al. "Test of lepton flavor universality by the measurement of the $B^0 \to D^{*-}\tau^+\nu_\tau$ branching fraction using three-prong τ decays". In: *Physical Review D* 97.7 (2018). ISSN: 2470-0029. DOI: 10.1103/physrevd.97.072013. URL: http://dx.doi.org/10.1103/PhysRevD.97.072013.

[42] F. U. Bernlochner et al. "Combined analysis of semileptonic B decays to D and D^* : $\mathcal{R}(D^{(*)})$, $|V_{cb}|$, and new physics". In: *Physical Review D* 95.11 (2017). ISSN: 2470-0029. DOI: 10.1103/physrevd.95.115008. URL: http://dx.doi.org/10.1103/PhysRevD.95.115008.

[43] S. Jaiswal, S. Nandi, and S. K. Patra. "Extraction of $|V_{cb}|$ from $B \to D^{(*)}\ell\nu_\ell$ and the Standard Model predictions of $\mathcal{R}(D^{(*)})$". In: *Journal of High Energy Physics* 2017.12 (2017). ISSN: 1029-8479. DOI: 10.1007/jhep12(2017)060. URL: http://dx.doi.org/10.1007/JHEP12(2017)060.

[44] D. Bigi, P. Gambino, and S. Schacht. "$\mathcal{R}(D^*)$, $|V_{cb}|$, and the Heavy Quark Symmetry relations between form factors". In: *Journal of High Energy Physics* 2017.11 (2017). ISSN: 1029-8479. DOI: 10.1007/jhep11(2017)061. URL: http://dx.doi.org/10.1007/JHEP11(2017)061.

[45] R. Aaij et al. "Search for Lepton-Universality Violation in $B^+ \to K^+\ell^+\ell^-$ Decays". In: *Physical Review Letters* 122.19 (2019). ISSN: 1079-7114. DOI: 10.1103/physrevlett.122.191801. URL: http://dx.doi.org/10.1103/PhysRevLett.122.191801.

[46] R. Aaij et al. "Branching Fraction Measurements of the Rare $B_s^0 \to \phi\mu^+\mu^-$ and $B_s^0 \to f_2'(1525)\mu^+\mu^-$ Decays". In: *Physical Review Letters* 127.15 (2021). ISSN: 1079-7114. DOI: 10.1103/physrevlett.127.151801. URL: http://dx.doi.org/10.1103/PhysRevLett.127.151801.

[47] M. Peskin and D. Schroeder. *An Introduction To Quantum Field Theory*. Frontiers in Physics. Avalon Publishing, 1995. ISBN: 9780813345437.

[48] L. M. Brown. "Dirac's The Principles of Quantum Mechanics". In: 2006.

[49] R. P. Feynman. "Space-Time Approach to Non-Relativistic Quantum Mechanics". In: *Reviews of Modern Physics* 20.2 (Apr. 1948), pp. 367–387. DOI: 10.1103/RevModPhys.20.367.

[50] F. Englert and R. Brout. "Broken Symmetry and the Mass of Gauge Vector Mesons". In: *Physical Review Letters* 13.9 (Aug. 1964), pp. 321–323. DOI: 10.1103/PhysRevLett.13.321.

[51] P. W. Higgs. "Broken Symmetries and the Masses of Gauge Bosons". In: *Physical Review Letters* 13.16 (Oct. 1964), pp. 508–509. DOI: 10.1103/PhysRevLett.13.508.

[52] G. S. Guralnik, C. R. Hagen, and T. W. Kibble. "Global Conservation Laws and Massless Particles". In: *Physical Review Letters* 13.20 (Nov. 1964), pp. 585–587. DOI: 10.1103/PhysRevLett.13.585.

[53] L. Wolfenstein. "Parametrization of the Kobayashi-Maskawa Matrix". In: *Phys. Rev. Lett.* 51 (21 1983), pp. 1945–1947. DOI: 10.1103/PhysRevLett.51.1945. URL: https://link.aps.org/doi/10.1103/PhysRevLett.51.1945.

[54] B. Pontecorvo. "Inverse beta processes and nonconservation of lepton charge". In: *Zh. Eksp. Teor. Fiz.* 34 (1957), p. 247.

[55] Z. Maki, M. Nakagawa, and S. Sakata. "Remarks on the Unified Model of Elementary Particles". In: *Progress of Theoretical Physics* 28.5 (Nov. 1962), pp. 870–880. ISSN: 0033-068X. DOI: 10.1143/PTP.28.870. eprint: https://academic.oup.com/ptp/article-pdf/28/5/870/5258750/28-5-870.pdf. URL: https://doi.org/10.1143/PTP.28.870.

[56] E. Swanson. "New Particle Hints at Four-Quark Matter". In: *Physics Online Journal* 6, 69 (June 2013), p. 69. DOI: 10.1103/Physics.6.69.

[57] R. Aaij et al. "Observation of J/ψ Resonances Consistent with Pentaquark States in $\Lambda_b^0 \to J/\psi k^- p$ Decays". In: *Physical Review Letters* 115.7 (2015). ISSN: 1079-7114. DOI: 10.1103/physrevlett.115.072001. URL: http://dx.doi.org/10.1103/PhysRevLett.115.072001.

[58] E. Martynov and B. Nicolescu. "Did TOTEM experiment discover the Odderon?" In: *Physics Letters B* 778 (2018), 414–418. ISSN: 0370-2693. DOI: 10.1016/j.physletb.2018.01.054. URL: http://dx.doi.org/10.1016/j.physletb.2018.01.054.

[59] T. Csörgő et al. "Evidence of Odderon-exchange from scaling properties of elastic scattering at TeV energies". In: *The European Physical Journal C* 81.2 (2021). ISSN: 1434-6052. DOI: 10.1140/epjc/s10052-021-08867-6. URL: http://dx.doi.org/10.1140/epjc/s10052-021-08867-6.

[60] V. M. Abazov et al. "Odderon Exchange from Elastic Scattering Differences between pp and $p\bar{p}$ Data at 1.96 TeV and from pp Forward Scattering Measurements". In: *Phys. Rev. Lett.* 127 (6 2021), p. 062003. DOI: 10.1103/PhysRevLett.127.062003. URL: https://link.aps.org/doi/10.1103/PhysRevLett.127.062003.

[61] A. Deur, S. J. Brodsky, and G. F. de Téramond. "The QCD running coupling". In: *Progress in Particle and Nuclear Physics* 90 (2016), 1–74. ISSN: 0146-6410. DOI: 10.1016/j.ppnp.2016.04.003. URL: http://dx.doi.org/10.1016/j.ppnp.2016.04.003.

[62] D. J. Gross and F. Wilczek. "Ultraviolet Behavior of Non-Abelian Gauge Theories". In: *Physical Review Letters* 30.26 (June 1973), pp. 1343–1346. DOI: 10.1103/PhysRevLett.30.1343.

[63] H. D. Politzer. "Reliable Perturbative Results for Strong Interactions?" In: *Physical Review Letters* 30.26 (June 1973), pp. 1346–1349. DOI: 10.1103/PhysRevLett.30.1346.

[64] G. 't Hooft. "Symmetry Breaking through Bell-Jackiw Anomalies". In: *Phys. Rev. Lett.* 37 (1 1976), pp. 8–11. DOI: 10.1103/PhysRevLett.37.8. URL: https://link.aps.org/doi/10.1103/PhysRevLett.37.8.

[65] R. D. Peccei and H. R. Quinn. "CP Conservation in the Presence of Pseudoparticles". In: *Phys. Rev. Lett.* 38 (25 1977), pp. 1440–1443. DOI: 10.1103/PhysRevLett.38.1440. URL: https://link.aps.org/doi/10.1103/PhysRevLett.38.1440.

[66] F. Wilczek. "Problem of Strong P and T Invariance in the Presence of Instantons". In: *Phys. Rev. Lett.* 40 (5 1978), pp. 279–282. DOI: 10.1103/PhysRevLett.40.279. URL: https://link.aps.org/doi/10.1103/PhysRevLett.40.279.

[67] S. Weinberg. "A New Light Boson?" In: *Phys. Rev. Lett.* 40 (4 1978), pp. 223–226. DOI: 10.1103/PhysRevLett.40.223. URL: https://link.aps.org/doi/10.1103/PhysRevLett.40.223.

[68] L. Di Luzio et al. "The landscape of QCD axion models". In: *Physics Reports* 870 (2020). The landscape of QCD axion models, pp. 1–117. ISSN: 0370-1573. DOI: https://doi.org/10.1016/j.physrep.2020.06.002. URL: https://www.sciencedirect.com/science/article/pii/S0370157320302477.

[69] K. Fujikawa. "Path Integral Measure for Gauge Invariant Fermion Theories". In: *Phys. Rev. Lett.* 42 (1979), 1195–1198.

[70] J. Goldstone. "Field theories with Superconductor solutions". In: *Il Nuovo Cimento* 19.1 (Jan. 1961), pp. 154–164. DOI: 10.1007/BF02812722.

[71] S. Coleman, J. Wess, and B. Zumino. "Structure of Phenomenological Lagrangians. I". In: *Phys. Rev.* 177 (5 1969), pp. 2239–2247. DOI: 10.1103/PhysRev.177.2239. URL: https://link.aps.org/doi/10.1103/PhysRev.177.2239.

[72] C. G. Callan et al. "Structure of Phenomenological Lagrangians. II". In: *Phys. Rev.* 177 (5 1969), pp. 2247–2250. DOI: 10.1103/PhysRev.177.2247. URL: https://link.aps.org/doi/10.1103/PhysRev.177.2247.

[73] F. L. Wilson. "Fermi's Theory of Beta Decay". In: *American Journal of Physics* 36.12 (1968), pp. 1150–1160. DOI: 10.1119/1.1974382. eprint: https://doi.org/10.1119/1.1974382. URL: https://doi.org/10.1119/1.1974382.

[74] K. G. Wilson. "Non-Lagrangian Models of Current Algebra". In: *Phys. Rev.* 179 (5 1969), pp. 1499–1512. DOI: 10.1103/PhysRev.179.1499. URL: https://link.aps.org/doi/10.1103/PhysRev.179.1499.

[75] K. G. Wilson and W. Zimmermann. "Operator product expansions and composite field operators in the general framework of quantum field theory". In: *Commun. Math. Phys.* 24 (1972), pp. 87–106. DOI: 10.1007/BF01878448.

[76] W. Zimmermann. "Normal products and the short distance expansion in the perturbation theory of renormalizable interactions". In: *Annals Phys.* 77 (1973), pp. 570–601. DOI: 10.1016/0003-4916(73)90430-2.

[77] Y. Aoki et al. "FLAG Review 2021". In: (Nov. 2021). arXiv: 2111.09849 [hep-lat].

[78] S. Aoki et al. "FLAG Review 2019". In: *The European Physical Journal C* 80.2 (2020). ISSN: 1434-6052. DOI: 10.1140/epjc/s10052-019-7354-7. URL: http://dx.doi.org/10.1140/epjc/s10052-019-7354-7.

[79] L. Cao et al. "Measurements of partial branching fractions of inclusive $B \to X_u \ell^+ \nu_\ell$ decays with hadronic tagging". In: *Phys. Rev. D* 104 (1 2021), p. 012008. DOI: 10.1103/PhysRevD.104.012008. URL: https://link.aps.org/doi/10.1103/PhysRevD.104.012008.

[80] W. Altmannshofer et al. "The Belle II Physics Book". In: *PTEP* 2019.12 (2019). Ed. by E. Kou and P. Urquijo. [Erratum: PTEP 2020, 029201 (2020)], p. 123C01. DOI: 10.1093/ptep/ptz106. arXiv: 1808.10567 [hep-ex].

[81] B. Aubert et al. "Measurements of $B \to \{\pi, \eta, \eta'\}\ell\nu_\ell$ Branching Fractions and Determination of $|V_{ub}|$ with Semileptonically Tagged B Mesons". In: *Phys. Rev. Lett.* 101 (2008), p. 081801. DOI: 10.1103/PhysRevLett.101.081801. arXiv: 0805.2408 [hep-ex].

[82] P. del Amo Sanchez et al. "Study of $B \to \pi\ell\nu$ and $B \to \rho\ell\nu$ Decays and Determination of $|V_{ub}|$". In: *Phys. Rev. D* 83 (2011), p. 032007. DOI: 10.1103/PhysRevD.83.032007. arXiv: 1005.3288 [hep-ex].

[83] J. P. Lees et al. "Branching fraction and form-factor shape measurements of exclusive charmless semileptonic B decays, and determination of $|V_{ub}|$". In: *Phys. Rev. D* 86 (2012), p. 092004. DOI: 10.1103/PhysRevD.86.092004. arXiv: 1208.1253 [hep-ex].

[84] T. Hokuue et al. "Measurements of branching fractions and q^2 distributions for $B \to \pi\ell\nu$ and $B \to \rho\ell\nu$ decays with $B \to D^{(*)}\ell\nu$ decay tagging". In: *Phys. Lett. B* 648 (2007), pp. 139–148. DOI: 10.1016/j.physletb.2007.02.067. arXiv: hep-ex/0604024.

[85] H. Ha et al. "Measurement of the decay $B^0 \to \pi^-\ell^+\nu$ and determination of $|V_{ub}|$". In: *Phys. Rev. D* 83 (2011), p. 071101. DOI: 10.1103/PhysRevD.83.071101. arXiv: 1012.0090 [hep-ex].

[86] A. Sibidanov et al. "Study of Exclusive $B \to X_u\ell\nu$ Decays and Extraction of $\|V_{ub}\|$ using Full Reconstruction Tagging at the Belle Experiment". In: *Phys. Rev. D* 88.3 (2013), p. 032005. DOI: 10.1103/PhysRevD.88.032005. arXiv: 1306.2781 [hep-ex].

[87] N. E. Adam et al. "A Study of Exclusive Charmless Semileptonic B Decay and $|V_{ub}|$". In: *Phys. Rev. Lett.* 99 (2007), p. 041802. DOI: 10.1103/PhysRevLett.99.041802. arXiv: hep-ex/0703041.

[88] R. Aaij et al. "First Observation of the Decay $B_s^0 \to K^- \mu^+ \nu_\mu$ and a Measurement of $|V_{ub}|/|V_{cb}|$". In: *Physical Review Letters* 126.8 (2021). ISSN: 1079-7114. DOI: 10.1103/physrevlett.126.081804. URL: http://dx.doi.org/10.1103/PhysRevLett.126.081804.

[89] C. M. Bouchard et al. "$B_s \to K\ell\nu$ form factors from lattice QCD". In: *Phys. Rev.* D90 (2014), p. 054506. DOI: 10.1103/PhysRevD.90.054506. arXiv: 1406.2279 [hep-lat].

[90] J. Flynn et al. "$B \to \pi\ell\nu$ and $B_s \to K\ell\nu$ form factors and $|V_{ub}|$ from 2+1-flavor lattice QCD with domain-wall light quarks and relativistic heavy quarks". In: *Physical Review D* 91.7 (2015). ISSN: 1550-2368. DOI: 10.1103/physrevd.91.074510. URL: http://dx.doi.org/10.1103/PhysRevD.91.074510.

[91] A. Bazavov et al. "$B_s \to K\ell\nu$ decay from lattice QCD". In: *Phys. Rev. D* 100.3 (2019), p. 034501. DOI: 10.1103/PhysRevD.100.034501. arXiv: 1901.02561 [hep-lat].

[92] E. Dalgic et al. "B meson semileptonic form-factors from unquenched lattice QCD". In: *Phys. Rev.* D73 (2006). [Erratum: Phys. Rev.D75,119906(2007)], p. 074502. DOI: 10.1103/PhysRevD.75.119906,10.1103/PhysRevD.73.074502. arXiv: hep-lat/0601021 [hep-lat].

[93] J. A. Bailey et al. "$|V_{ub}|$ from $B \to \pi\ell\nu$ decays and (2+1)-flavor lattice QCD". In: *Phys. Rev.* D92.1 (2015), p. 014024. DOI: 10.1103/PhysRevD.92.014024. arXiv: 1503.07839 [hep-lat].

[94] S. Aoki et al. *Review of lattice results concerning low-energy particle physics*. 2016. arXiv: 1607.00299 [hep-lat].

[95] C. Gattringer and C. Lang. *Quantum Chromodynamics on the Lattice: An Introductory Presentation*. Lecture Notes in Physics. Springer Berlin Heidelberg, 2009. ISBN: 9783642018497.

[96] W. Pauli and F. Villars. "On the Invariant Regularization in Relativistic Quantum Theory". In: *Rev. Mod. Phys.* 21 (3 1949), pp. 434–444. DOI: 10.1103/RevModPhys.21.434. URL: https://link.aps.org/doi/10.1103/RevModPhys.21.434.

[97] G. 't Hooft and M. Veltman. "Regularization and renormalization of gauge fields". In: *Nuclear Physics B* 44.1 (July 1972), pp. 189–213. DOI: 10.1016/0550-3213(72)90279-9.

[98] C. G. Bollini and J. J. Giambiagi. "Dimensional renorinalization : The number of dimensions as a regularizing parameter". In: *Il Nuovo Cimento B (1971-1996)* 12.1 (Nov. 1972). DOI: 10.1007/BF02895558. URL: https://doi.org/10.1007/BF02895558.

[99] G. 't Hooft. "Dimensional regularization and the renormalization group". In: *Nucl. Phys. B* 61 (1973), pp. 455–468. DOI: 10.1016/0550-3213(73)90376-3.

[100] P. T. Matthews and A. Salam. "The Green's functions of quantised fields". In: *Il Nuovo Cimento* 12.4 (Oct. 1954), pp. 563–565. DOI: 10.1007/BF02781302.

[101] P. T. Matthews and A. Salam. "Propagators of quantized field". In: *Nuovo Cim.* 2 (1955), pp. 120–134. DOI: 10.1007/BF02856011.

[102] G. C. Wick. "The Evaluation of the Collision Matrix". In: *Phys. Rev.* 80 (2 1950), pp. 268–272. DOI: 10.1103/PhysRev.80.268. URL: https://link.aps.org/doi/10.1103/PhysRev.80.268.

[103] F. Fucito et al. "A proposal for Monte Carlo simulations of fermionic systems". In: *Nuclear Physics B* 180.3 (1981), pp. 369–377. ISSN: 0550-3213. DOI: https://doi.org/10.1016/0550-3213(81)90055-9. URL: https://www.sciencedirect.com/science/article/pii/0550321381900559.

[104] D. Weingarten and D. Petcher. "Monte Carlo integration for lattice gauge theories with fermions". In: *Physics Letters B* 99.4 (1981), pp. 333–338. ISSN: 0370-2693. DOI: https://doi.org/10.1016/0370-2693(81)90112-X. URL: https://www.sciencedirect.com/science/article/pii/037026938190112X.

[105] S. Duane et al. "Hybrid Monte Carlo". In: *Physics Letters B* 195.2 (Sept. 1987), pp. 216–222. DOI: 10.1016/0370-2693(87)91197-X.

[106] S. Güsken. "A study of smearing techniques for hadron correlation functions". In: *Nuclear Physics B - Proceedings Supplements* 17 (1990), pp. 361–364. ISSN: 0920-5632. DOI: https://doi.org/10.1016/0920-5632(90)90273-W. URL: https://www.sciencedirect.com/science/article/pii/092056329090273W.

[107] M. R. Hestenes and E. Stiefel. "Methods of conjugate gradients for solving linear systems". In: *Journal of research of the National Bureau of Standards* 49 (1952), pp. 409–435.

[108] R. G. Edwards and B. Joó. "The Chroma Software System for Lattice QCD". In: *Nuclear Physics B - Proceedings Supplements* 140 (2005), 832–834. ISSN: 0920-5632. DOI: 10.1016/j.nuclphysbps.2004.11.254. URL: http://dx.doi.org/10.1016/j.nuclphysbps.2004.11.254.

[109] K. Symanzik. "Continuum limit and improved action in lattice theories: (I). Principles and ϕ^4 theory". In: *Nuclear Physics B* 226.1 (1983), pp. 187–204. ISSN: 0550-3213. DOI: https://doi.org/10.1016/0550-3213(83)90468-6. URL: https://www.sciencedirect.com/science/article/pii/0550321383904686.

[110] K. Symanzik. "Continuum limit and improved action in lattice theories: (II). O(N) non-linear sigma model in perturbation theory". In: *Nuclear Physics B* 226.1 (1983), pp. 205–227. ISSN: 0550-3213. DOI: https://doi.org/10.1016/0550-3213(83)90469-8. URL: https://www.sciencedirect.com/science/article/pii/0550321383904698.

[111] M. Lüscher and P. Weisz. "Computation of the action for on-shell improved lattice gauge theories at weak coupling". In: *Physics Letters B* 158.3 (1985), pp. 250–254. ISSN: 0370-2693. DOI: https://doi.org/10.1016/0370-2693(85)90966-9. URL: https://www.sciencedirect.com/science/article/pii/0370269385909669.

[112] W. Bietenholz and U.-J. Wiese. "Perfect lattice actions for quarks and gluons". In: *Nuclear Physics B* 464.1 (1996), pp. 319–350. ISSN: 0550-3213. DOI: https://doi.org/10.1016/0550-3213(95)00678-8. URL: https://www.sciencedirect.com/science/article/pii/0550321395006788.

[113] K. G. Wilson and J. Kogut. "The renormalization group and the ϵ expansion". In: *Physics Reports* 12.2 (1974), pp. 75–199. ISSN: 0370-1573. DOI: https://doi.org/10.1016/0370-1573(74)90023-4. URL: https://www.sciencedirect.com/science/article/pii/0370157374900234.

[114] K. G. Wilson. "The renormalization group: Critical phenomena and the Kondo problem". In: *Rev. Mod. Phys.* 47 (4 1975), pp. 773–840. DOI: 10.1103/RevModPhys.47.773. URL: https://link.aps.org/doi/10.1103/RevModPhys.47.773.

[115] Y. Iwasaki and T. Yoshié. "Renormalization group improved action for SU(3) lattice gauge theory and the string tension". In: *Physics Letters B* 143.4-6 (Aug. 1984), pp. 449–452. DOI: 10.1016/0370-2693(84)91500-4.

[116] Y. Iwasaki. *Renormalization Group Analysis of Lattice Theories and Improved Lattice Action. II – four-dimensional non-abelian SU(N) gauge model*. 2011. arXiv: 1111.7054 [hep-lat].

[117] T. Takaishi. "Heavy quark potential and effective actions on blocked configurations". In: *Phys. Rev. D* 54 (1 1996), pp. 1050–1053. DOI: 10.1103/PhysRevD.54.1050. URL: https://link.aps.org/doi/10.1103/PhysRevD.54.1050.

[118] P. de Forcrand et al. "Renormalization group flow of SU(3) lattice gauge theory. Numerical studies in a two coupling space". In: *Nuclear Physics B* 577.1 (2000), pp. 263–278. ISSN: 0550-3213. DOI: https://doi.org/10.1016/S0550-3213(00)00145-0. URL: https://www.sciencedirect.com/science/article/pii/S0550321300001450.

[119] D. J. Antonio et al. "First results from 2 + 1-flavor domain wall QCD: Mass spectrum, topology change, and chiral symmetry with $L_s = 8$". In: *Phys. Rev. D* 75 (11 2007), p. 114501. DOI: 10.1103/PhysRevD.75.114501. URL: https://link.aps.org/doi/10.1103/PhysRevD.75.114501.

[120] C. Allton et al. "Physical results from 2 + 1 flavor domain wall QCD and SU(2) chiral perturbation theory". In: *Phys. Rev. D* 78 (11 2008), p. 114509. DOI: 10.1103/PhysRevD.78.114509. URL: https://link.aps.org/doi/10.1103/PhysRevD.78.114509.

[121] Y. Aoki et al. "Continuum limit physics from 2 + 1 flavor domain wall QCD". In: *Phys. Rev. D* 83 (7 2011), p. 074508. DOI: 10.1103/PhysRevD.83.074508. URL: https://link.aps.org/doi/10.1103/PhysRevD.83.074508.

[122] T. Blum et al. "Domain wall QCD with physical quark masses". In: *Phys. Rev. D* 93 (7 2016), p. 074505. DOI: 10.1103/PhysRevD.93.074505. URL: https://link.aps.org/doi/10.1103/PhysRevD.93.074505.

[123] H. Nielsen and M. Ninomiya. "A no-go theorem for regularizing chiral fermions". In: *Physics Letters B* 105.2 (1981), pp. 219–223. ISSN: 0370-2693. DOI: https://doi.org/10.1016/0370-2693(81)91026-1. URL: https://www.sciencedirect.com/science/article/pii/0370269381910261.

[124] P. H. Ginsparg and K. G. Wilson. "A remnant of chiral symmetry on the lattice". In: *Phys. Rev. D* 25 (10 1982), pp. 2649–2657. DOI: 10.1103/PhysRevD.25.2649. URL: https://link.aps.org/doi/10.1103/PhysRevD.25.2649.

[125] M. Lüscher. "Exact chiral symmetry on the lattice and the Ginsparg-Wilson relation". In: *Physics Letters B* 428.3-4 (1998), 342–345. ISSN: 0370-2693. DOI: 10.1016/s0370-2693(98)00423-7. URL: http://dx.doi.org/10.1016/S0370-2693(98)00423-7.

[126] D. B. Kaplan. *Chiral Symmetry and Lattice Fermions*. 2012. arXiv: 0912.2560 [hep-lat].

[127] R. Narayanan and H. Neuberger. "Infinitely many regulator fields for chiral fermions". In: *Physics Letters B* 302.1 (1993), 62–69. ISSN: 0370-2693. DOI: 10.1016/0370-2693(93)90636-v. URL: http://dx.doi.org/10.1016/0370-2693(93)90636-V.

[128] R. Narayanan and H. Neuberger. "Chiral fermions on the lattice". In: *Physical Review Letters* 71.20 (1993), 3251–3254. ISSN: 0031-9007. DOI: 10.1103/physrevlett.71.3251. URL: http://dx.doi.org/10.1103/PhysRevLett.71.3251.

[129] R. Narayanan and H. Neuberger. "Chiral determinant as an overlap of two vacua". In: *Nuclear Physics B* 412.3 (1994), 574–606. ISSN: 0550-3213. DOI: 10.1016/0550-3213(94)90393-x. URL: http://dx.doi.org/10.1016/0550-3213(94)90393-X.

[130] R. Narayanan and H. Neuberger. "A construction of lattice chiral gauge theories". In: *Nuclear Physics B* 443.1-2 (1995), 305–385. ISSN: 0550-3213. DOI: 10.1016/0550-3213(95)00111-5. URL: http://dx.doi.org/10.1016/0550-3213(95)00111-5.

[131] H. Neuberger. "Exactly massless quarks on the lattice". In: *Physics Letters B* 417.1-2 (1998), 141–144. ISSN: 0370-2693. DOI: 10.1016/s0370-2693(97)01368-3. URL: http://dx.doi.org/10.1016/S0370-2693(97)01368-3.

[132] H. Neuberger. "More about exactly massless quarks on the lattice". In: *Physics Letters B* 427.3-4 (1998), 353–355. ISSN: 0370-2693. DOI: 10.1016/s0370-2693(98)00355-4. URL: http://dx.doi.org/10.1016/S0370-2693(98)00355-4.

[133] B. Sheikholeslami and R. Wohlert. "Improved continuum limit lattice action for QCD with wilson fermions". In: *Nuclear Physics B* 259.4 (1985), pp. 572–596. ISSN: 0550-3213. DOI: https://doi.org/10.1016/0550-3213(85)90002-1.

[134] H.-W. Lin and N. Christ. "Nonperturbatively determined relativistic heavy quark action". In: *Physical Review D* 76.7 (2007). ISSN: 1550-2368. DOI: 10.1103/physrevd.76.074506. URL: http://dx.doi.org/10.1103/PhysRevD.76.074506.

[135] C. Lehner. *Private Communication*. 2014.

[136] G. P. Lepage and P. B. Mackenzie. "Viability of lattice perturbation theory". In: *Physical Review D* 48.5 (1993), 2250–2264. ISSN: 0556-2821. DOI: 10.1103/physrevd.48.2250. URL: http://dx.doi.org/10.1103/PhysRevD.48.2250.

[137] S. Hashimoto et al. "Lattice QCD calculation of $\overline{B} \to D\ell\overline{\nu}$ decay form factors at zero recoil". In: *Physical Review D* 61.1 (1999). ISSN: 1089-4918. DOI: 10.1103/physrevd.61.014502. URL: http://dx.doi.org/10.1103/PhysRevD.61.014502.

[138] A. X. El-Khadra et al. "Semileptonic decays $\vec{B}\ \pi l\nu$ and $\vec{D}\ \pi l\nu$ from lattice QCD". In: *Phys. Rev. D* 64 (1 2001), p. 014502. DOI: 10.1103/PhysRevD.64.014502. URL: https://link.aps.org/doi/10.1103/PhysRevD.64.014502.

[139] J. Harada et al. "Application of heavy-quark effective theory to lattice QCD. III. Radiative corrections to heavy-heavy currents". In: *Physical Review D* 65.9 (2002), p. 094514.

[140] Y. Aoki et al. "Continuum limit physics from 2+1flavor domain wall QCD". In: *Physical Review D* 83.7 (2011). ISSN: 1550-2368. DOI: 10.1103/physrevd.83.074508. URL: http://dx.doi.org/10.1103/PhysRevD.83.074508.

[141] N. Christ et al. "B-meson decay constants from 2+1-flavor lattice QCD with domain-wall light quarks and relativistic heavy quarks". In: *Physical Review D* 91.5 (2015). ISSN: 1550-2368. DOI: 10.1103/physrevd.91.054502. URL: http://dx.doi.org/10.1103/PhysRevD.91.054502.

[142] M. B. Wise. "Chiral perturbation theory for hadrons containing a heavy quark". In: *Phys. Rev. D* 45 (7 1992), R2188–R2191. DOI: 10.1103/PhysRevD.45.R2188.

[143] G. Burdman and J. F. Donoghue. "Union of chiral and heavy quark symmetries". In: *Physics Letters B* 280.3 (1992), pp. 287–291. ISSN: 0370-2693. DOI: https://doi.org/10.1016/0370-2693(92)90068-F.

[144] T. Yan et al. "Heavy-quark symmetry and chiral dynamics". English. In: *Physical Review D* 46.3 (Jan. 1992), pp. 1148–1164. ISSN: 2470-0010. DOI: 10.1103/PhysRevD.46.1148.

[145] P. Cho. "Chiral perturbation theory for hadrons containing a heavy quark. The sequel". In: *Physics Letters B* 285.1 (1992), pp. 145–152. ISSN: 0370-2693. DOI: https://doi.org/10.1016/0370-2693(92)91314-Y.

[146] A. Manohar and M. Wise. *Heavy Quark Physics*. Cambridge Monographs on Particle Physics, Nuclear Physics and Cosmology. Cambridge University Press, 2007. ISBN: 9780521037570.

[147] D. Becirevic, S. Prelovsek, and J. Zupan. *$B \to \pi$ and $B \to K$ transitions in standard and quenched chiral perturbation theory*. 2002. arXiv: hep-lat/0210048 [hep-lat].

[148] J. Flynn and C. Sachrajda. "SU(2) chiral perturbation theory for Kl3 decay amplitudes". In: *Nuclear Physics B* 812.1-2 (2009), 64–80. ISSN: 0550-3213. DOI: 10.1016/j.nuclphysb.2008.12.001. URL: http://dx.doi.org/10.1016/j.nuclphysb.2008.12.001.

[149] J. Bijnens and I. Jemos. "Hard pion chiral perturbation theory for $B \to \pi$ and $D \to \pi$ formfactors". In: *Nuclear Physics B* 840.1 (2010), pp. 54–66. ISSN: 0550-3213. DOI: https://doi.org/10.1016/j.nuclphysb.2010.06.021. URL: https://www.sciencedirect.com/science/article/pii/S0550321310003469.

[150] Boyd, Grinstein, and Lebed. "Constraints on form factors for exclusive semileptonic heavy to light meson decays." In: *Physical review letters* 74 23 (1995), pp. 4603–4606.

[151] L. Lellouch. "Lattice-Constrained Unitarity Bounds for $B_0 \to \pi^+ l^+ \nu^=$ Decays". In: 2008.

[152] C. Bourrely, L. Lellouch, and I. Caprini. "Model-independent description of $B \to \pi l \nu$ decays and a determination of $|V_{ub}|$". In: *Phys. Rev. D* 79 (1 2009), p. 013008. DOI: 10.1103/PhysRevD.79.013008. URL: https://link.aps.org/doi/10.1103/PhysRevD.79.013008.

[153] C. M. Arnesen et al. "Precision Model Independent Determination of $|V_{\mathrm{ub}}|$ from $B \to \pi l \nu$". In: *Phys. Rev. Lett.* 95 (7 2005), p. 071802. DOI: 10.1103/PhysRevLett.95.071802. URL: https://link.aps.org/doi/10.1103/PhysRevLett.95.071802.

[154] A. X. El-Khadra. *Lattice calculation of meson form-factors for semileptonic decays*. PhD thesis, UCLA, 1989.

[155] G. Isidori and O. Sumensari. "Optimized lepton universality tests in $B \to V\ell\bar{\nu}$ decays". In: *The European Physical Journal C* 80.11 (2020). ISSN: 1434-6052. DOI: 10.1140/epjc/s10052-020-08653-w. URL: http://dx.doi.org/10.1140/epjc/s10052-020-08653-w.

[156] M. Freytsis, Z. Ligeti, and J. T. Ruderman. "Flavor models for $\overline{B} \to D^{(*)}\tau\nu$". In: *Physical Review D* 92.5 (2015). ISSN: 1550-2368. DOI: 10.1103/physrevd.92.054018. URL: http://dx.doi.org/10.1103/PhysRevD.92.054018.

[157] F. U. Bernlochner and Z. Ligeti. "Semileptonic $B_{(s)}$ decays to excited charmed mesons with e, μ, τ and searching for new physics with $R(D^{**})$". In: *Physical Review D* 95.1 (2017). ISSN: 2470-0029. DOI: 10.1103/physrevd.95.014022. URL: http://dx.doi.org/10.1103/PhysRevD.95.014022.

[158] C. Alexandrou et al. *Quark and gluon momentum fractions in the pion from $N_f = 2 + 1 + 1$ lattice QCD*. 2021. arXiv: 2109.10692 [hep-lat].

[159] C. Alexandrou et al. "Ratio of kaon and pion leptonic decay constants with $N_f = 2 + 1 + 1$ Wilson-clover twisted-mass fermions". In: *Physical Review D* 104.7 (2021). ISSN: 2470-0029. DOI: 10.1103/physrevd.104.074520. URL: http://dx.doi.org/10.1103/PhysRevD.104.074520.

[160] W. I. Jay et al. *B- and D-meson semileptonic decays with highly improved staggered quarks*. 2021. arXiv: 2111.05184 [hep-lat].

[161] Z. Gelzer et al. "B-meson semileptonic form factors on (2+1+1)-flavor HISQ ensembles". In: *PoS* LATTICE2019 (2019), p. 236. DOI: 10.22323/1.363.0236. arXiv: 1912.13358 [hep-lat].

[162] T. Blum et al. "Domain wall QCD with physical quark masses". In: *Physical Review D* 93.7 (2016). ISSN: 2470-0029. DOI: 10.1103/physrevd.93.074505. URL: http://dx.doi.org/10.1103/PhysRevD.93.074505.

[163] P. Boyle et al. "The decay constants fD and f D s f_{D_s} in the continuum limit of Nf = 2 + 1 domain wall lattice QCD". In: *Journal of High Energy Physics* 2017.12 (2017). ISSN: 1029-8479. DOI: 10.1007/jhep12(2017)008. URL: http://dx.doi.org/10.1007/JHEP12(2017)008.

[164] P. A. Boyle et al. *SU(3)-breaking ratios for $D_{(s)}$ and $B_{(s)}$ mesons*. 2020. arXiv: 1812.08791 [hep-lat].

[165] Y. Aoki et al. "Nonperturbative tuning of an improved relativistic heavy-quark action with application to bottom spectroscopy". In: *Physical Review D* 86.11 (2012). ISSN: 1550-2368. DOI: 10.1103/physrevd.86.116003. URL: http://dx.doi.org/10.1103/PhysRevD.86.116003.

[166] M. B. Oktay and A. S. Kronfeld. "New lattice action for heavy quarks". In: *Physical Review D* 78.1 (2008). ISSN: 1550-2368. DOI: 10.1103/physrevd.78.014504. URL: http://dx.doi.org/10.1103/PhysRevD.78.014504.

[167] B. Efron. "Bootstrap Methods: Another Look at the Jackknife". In: *The Annals of Statistics* 7.1 (1979), pp. 1 –26. DOI: 10.1214/aos/1176344552. URL: https://doi.org/10.1214/aos/1176344552.

[168] P. Virtanen et al. "SciPy 1.0: Fundamental Algorithms for Scientific Computing in Python". In: *Nature Methods* 17 (2020), pp. 261–272. DOI: 10.1038/s41592-019-0686-2.

[169] W. A. Bardeen, E. J. Eichten, and C. T. Hill. "Chiral multiplets of heavy-light mesons". In: *Physical Review D* 68.5 (2003). ISSN: 1089-4918. DOI: 10.1103/physrevd.68.054024. URL: http://dx.doi.org/10.1103/PhysRevD.68.054024.

[170] J. Flynn et al. "$B^*B\pi$ coupling using relativistic heavy quarks". In: *Physical Review D* 93.1 (2016). ISSN: 2470-0029. DOI: 10.1103/physrevd.93.014510. URL: http://dx.doi.org/10.1103/PhysRevD.93.014510.

[171] O. L. Buchmüller and H. U. Flächer. "Fit to moments of inclusive $B \to X_c \ell \overline{\nu}$ and $B \to X_s \gamma$ decay distributions using heavy quark expansions in the kinetic scheme". In: *Phys. Rev. D* 73 (7 2006), p. 073008. DOI: 10.1103/PhysRevD.73.073008. URL: https://link.aps.org/doi/10.1103/PhysRevD.73.073008.

[172] D. Giusti et al. "Leading isospin-breaking corrections to pion, kaon, and charmed-meson masses with twisted-mass fermions". In: *Physical Review D* 95.11 (2017). ISSN: 2470-0029. DOI: 10.1103/physrevd.95.114504. URL: http://dx.doi.org/10.1103/PhysRevD.95.114504.